Quantum and Classical Hilbert Space Fragmentation

Jonathan Classen-Howes

Merton College

University of Oxford

A thesis submitted for the degree of

Doctor of Philosophy

Michaelmas 2024

To my Grandmother

Acknowledgements

My doctoral studies were funded by scholarships from the Department of Physics at the University of Oxford and the Fonds de recherche du Québec – Nature et technologies. I would like to thank Professor Sid Parameswaran for giving me the opportunity to join his research group and for his guidance during my degree. I would also like to acknowledge the assistance of Professor Paul Fendley with evaluating and writing research results, and the constructive and encouraging comments I received from my examiners, Professors Steve Simon and Zlatko Papić, as well as from Professors John Chalker, Fabian Essler, and Shivaji Sondhi. I am very appreciative of the support and helpful advice I received as a doctoral student. I am particularly indebted to Dr. Abhishodh Prakash for his friendship and generosity with his time and expertise. I also wish to thank my fellow students in the condensed matter theory group, especially my collaborator Riccardo and my office-mates Jacob, Jovan, and Minghao, for interesting discussions and exciting times working together. Throughout the whole process, my family has been a wonderful source of support and insights. Thank you for making this journey possible!

Statement of Originality

This thesis is based on the following co-authored works:

- J. Classen-Howes, P. Fendley, A. Pandey, and S. A. Parameswaran. "Bipartite Sachdev-Ye models with Read-Saleur symmetries". In: *Phys. Rev. B* 110 (12 Sept. 2024), p. 125140. [Editors' Suggestion]
- J. Classen-Howes, R. Senese, and A. Prakash. "Universal Freezing Transitions of Dipole-Conserving Chains". 2024. arXiv: `2408.10321 [cond-mat.str-el]`

The results presented in this thesis are my own work except where indicated otherwise in the text.

Abstract

Hilbert space fragmentation has provided fruitful grounds for the study of ergodicity violations and unusual symmetry structures in a variety of quantum systems. In this thesis, I use analytic and numerical approaches to examine these features in two contrasting Hilbert-space-fragmented models. One of these models exhibits "quantum fragmentation" (where the fragmentation can only be described in an entangled basis), the other displays "classical fragmentation" (where the fragmentation can be described in a product-state basis).

The quantum-fragmented system is an SU(M)-symmetric disordered bipartite spin model which, for $M \geq 3$, has a large non-trivial nullspace whose dimension grows exponentially with system size. This exponential growth leads to a rare example of Hilbert space fragmentation in a system with long-range interactions. I characterise the nullspace and the resulting fragmentation in detail, and show that the symmetry algebra responsible for the large degeneracy is a non-trivial subalgebra of the Read-Saleur commutant algebra. I also discuss perturbations of the model, including one that transforms certain states in the nullspace into quantum many-body scars.

The classically fragmented system is a family of quantum chains with local range-k interactions subject to the conservation of a total charge and its dipole moment. Such models exhibit a continuous "freezing" phase transition between weakly fragmented (ergodic) and strongly fragmented (non-ergodic) phases as the charge density ν is varied. I use a variety of innovative approaches to analyse these models, and show that the transition occurs at a critical charge density of $\nu_c = (k-2)^{-1}$ independently of the onsite Hilbert space dimension. I also obtain numerous results characterising the properties of the different phases and their impact on the models' dynamical evolution. Together, the work in this thesis presents new insights into areas of fundamental importance to the exploration of Hilbert space fragmentation and ergodicity breaking.

Contents

List of Abbreviations

BES . . . . . Blockage-free Extended State.

BFES . . . . . Blockage-free Fully Extended State.

CAEE . . . . . Cut-Averaged Entanglement Entropy.

CS . . . . . Contracted State.

DOS . . . . . Density of States.

ETH . . . . . Eigenstate Thermalisation Hypothesis.

FES . . . . . Fully Extended State.

QMBS . . . . . Quantum Many-Body Scar.

RS . . . . . Read-Saleur.

SM . . . . . Shiraishi-Mori.

SY . . . . . Sachdev-Ye.

SYK . . . . . Sachdev-Ye-Kitaev.

TL . . . . . Temperley-Lieb.

1 Introduction

Isolated quantum systems evolving with time are generally expected to "thermalise" [3–6]. This means that such systems are predicted to eventually reach a highly entangled state in which any sufficiently small subsystem is in thermal equilibrium with the system as a whole. Hence, thermalising systems act as a heat bath for their subsystems. Such systems are often referred to as ergodic. Implications of this behaviour are formalised in the eigenstate thermalisation hypothesis (ETH), which states that thermalisation should also occur at the level of individual eigenstates. Consequently, in the thermodynamic limit, the expectation value of a local observable in an eigenstate of an ETH-obeying system should equal that observable's thermal expectation value in the appropriate thermal ensemble.

Although ETH is widely applicable in isolated quantum many-body systems, it is not universal, and the search for generic settings in which ETH fails has been a long-standing quest. It is known that ETH can be violated in the presence of strong quenched disorder, such as happens in Anderson-localised models [7, 8] and is conjectured to happen in many-body localised systems [5, 9, 10]. ETH can also be violated by the presence of an extensive set of conservation laws, as occurs in integrable models [3, 11]. Such settings often present strong violations of ETH: almost all eigenstates of a quantum model featuring one of these phenomena are expected to disobey ETH. There are also systems in which ETH is only weakly violated due to the presence of a measure-0 set of ETH-violating eigenstates in

an otherwise thermal spectrum. Such rare non-thermal eigenstates are referred to as quantum many-body scars (QMBS), and their study has led to a remarkable array of theoretical and experimental results [6, 12–30].

A newly discovered mechanism for breaking ETH which has been the subject of much recent research is Hilbert space fragmentation (HSF) [6, 15, 31–34]. Broadly speaking, HSF occurs in a quantum system when there exists a non-trivial decomposition of the system's Hilbert space into several dynamically disconnected "Krylov" subspaces whose number grows exponentially in system size. More specifically, the Hilbert space of a closed quantum system can generically be decomposed into some number K of Krylov subspaces $\{\mathcal{K}_i\}_{i=1}^{K}$ as

$$\mathcal{H} = \bigoplus_{i=1}^{K} \mathcal{K}_i, \quad \mathcal{K}_i := \mathrm{span}_t \left\{ U(t) \left| \psi_i \right\rangle \right\}, \tag{1.1}$$

where $U(t)$ is the unitary operator that governs the time evolution of the system (e.g. $U(t) = e^{-iHt}$ for a system with Hamiltonian H) and $\mathrm{span}_t \left\{ U(t) \left| \psi_i \right\rangle \right\}$ denotes the subspace spanned by time-evolution of the state $\left| \psi_i \right\rangle$. A trivial decomposition would be if the states $\{\left| \psi_i \right\rangle\}$ in Eq. (1.1) were chosen to be eigenstates of $U(t)$. Richer decompositions can be obtained if the model in question possesses a global symmetry, such that the $\{\left| \psi_i \right\rangle\}$ can be chosen to belong to different symmetry quantum number sectors. For example, in a system where particle number is conserved, one $\left| \psi_i \right\rangle$ could be chosen for each total particle number.

Hilbert space fragmentation occurs when there is a non-trivial choice of states $\{\left| \psi_i \right\rangle\}$ such that $K \sim e^{\alpha L}$, where L is the total system size. This is a greater scaling than can be explained via more conventional symmetries, such as particle-number conservation or SU(M). In fact, the different Krylov subspaces in fragmented models generally cannot be labeled by quantum numbers of any local symmetry of the model in question. Hilbert space fragmentation can lead to unconventional thermalisation dynamics from simple initial states and to violations of ETH.

Hilbert space fragmentation was first discovered in the context of quantum chains with strictly local interactions that conserve a global charge and its dipole

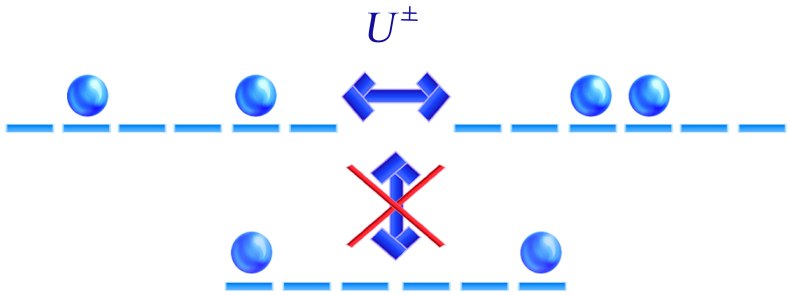

Figure 1.1: A simple example of a fractonic model: two hopping particles on a 1D lattice subject to particle-number and centre-of-mass conservation and to strictly local interactions of range $k = 4$. The two upper particle configurations can be connected by dynamical evolution via range-k inward and outward hops, represented by the operator $U^{\pm}$. However, they cannot be connected to the lower configuration despite sharing a same centre of mass and particle number.

moment [31–33]. Such models are examples of fractonic systems [35–40] as elementary excitations within them have restricted mobility when acted upon by local operators. An example of such a fragmented dipole-conserving chain is a system of identical particles on a 1D lattice, subject to random strictly local hopping motions which conserve particle number and centre of mass [41, 42]. In this system, the combined impact of the conservation laws and the locality of interactions ensures that particles cannot move independently of each other. Indeed, for a particle to hop in one direction, a hop in the opposite direction must be performed by another nearby particle to conserve centre of mass while respecting locality. Hence, certain particle configurations which share a same particle number and centre of mass cannot be linked under dynamical evolution. A simple example of this is presented in Fig. 1.1. The Hilbert space of such a model can then be decomposed into Krylov subspaces, where each subspace is composed of states that can be connected under the restricted dynamical evolution. The states $\{|\psi_i\rangle\}$ in Eq. (1.1) can then be chosen to be product states, corresponding to one configuration of particles from each Krylov subspace. As shown in [32, 33, 43] (and as we discuss in Section 2.3.2), there are an exponentially growing number of Krylov subspaces in

the model described, and hence the model is fragmented. Furthermore, many of the eigenstates of this system have area-law entanglement entropy, in stark contrast with the volume-law entanglement entropy predicted by ETH [5, 6].

Numerous other systems have also been found to exhibit Hilbert space fragmentation [1, 15, 34, 44–77]. In many of these models, including the locally interacting dipole-conserving models described above, the fragmentation is "classical" in nature, in that the Krylov subspaces making up the decomposition in Eq. (1.1) can be spanned using a basis of product states. Other examples of classically fragmented models include the $t - J_z$ model [34, 44] (which arises as a limiting form of the Hubbard model), certain domain-wall conserving models [45], the disordered $t - V$ model in the small t/V limit [46], a correlated hopping model of spinless fermions [47], the pair-flip model [48], and the transverse-field 2D quantum Ising model [49, 50].

In [34], a symmetry-based approach to describing fragmentation in terms of commutant algebras was proposed. This approach removed the ambiguities involved in the choice of basis states $\{|\psi_i\rangle\}$ in the decomposition in Eq. (1.1). It also generalised previous symmetry-based approaches to describing fragmentation in locally interacting dipole-conserving models and the $t-J_z$ model [44]. A commutant algebra $\mathcal{C}$ is defined for a family of Hamiltonians of the form $H = \sum_j J_j h_j$ as the algebra of all operators that commute with each of the few-body operators h_j individually, and hence with H for any choice of the coefficients J_j. Thus,

$$\mathcal{C} = \left\{ O \in \mathcal{L}(\mathcal{H}) \middle| [h_j, O] = 0 \ \forall j \right\}, \tag{1.2}$$

where $\mathcal{L}(\mathcal{H})$ is the algebra of all linear operators on the Hilbert space. For example, for a Hamiltonian which conserves total particle number N, the commutant algebra would include N as well as higher powers of this operator (N^2, N^3, ...) and their linear combinations. As we discuss in more detail in Section 2.2, commutant algebras provide a way to "block-diagonalise" the Hilbert space into Krylov subspaces. The number of Krylov subspaces obtained by this block-diagonalisation is related to the dimension of the commutant algebra, such that

$\log(\dim(\mathcal{C})) \sim L \iff \log(K) \sim L$. Hence, an exponentially growing commutant algebra implies Hilbert space fragmentation.

Using the commutant algebra formalism, the authors of [34] were able to identify the first example of a "quantum" fragmented system where the Krylov subspaces can only be spanned by an entangled basis. In particular, they highlighted that certain Temperley-Lieb spin chains have an exponentially growing commutant algebra. This algebra was first analysed in detail by Read and Saleur [78]. The Read-Saleur (RS) algebra is non-abelian and highly non-local and leads to exponentially growing degeneracies throughout the spectrum of these Temperley-Lieb chains. Subsequently, quantum Hilbert space fragmentation has also been found to arise in long-range generalisations of Temperley-Lieb chains [1], quantum East models [52], hard-rod deformations of certain spin-1/2 chains [53], flat-band lattices [54], and Bose-Hubbard diamond necklaces [55].

In addition to being categorised as classical or quantum, Hilbert space fragmentation can also be classified as strong or weak depending on how greatly it violates ETH [32, 33]. In the absence of conventional global symmetries, a model is considered to be weakly fragmented if there is a large dominant Krylov subspace to which almost all of the model's eigenstates belong in the thermodynamic limit. Hence, ETH is only weakly violated in the model, with the violation stemming from the presence of the rare eigenstates that are not in the dominant Krylov subspace. In a strongly fragmented model, all Krylov subspaces form a vanishingly small fraction of the total Hilbert space in the thermodynamic limit, and so ETH is strongly violated. In models with conventional global symmetries, such as the particle-hopping model discussed above, the degree of fragmentation must be assessed in each symmetry sector of the global symmetries individually. Hence, strong and weak fragmentation can coexist in a same spectrum.

In this thesis, we study two contrasting examples of quantum many-body systems which undergo Hilbert space fragmentation. The first is a quantum-fragmented model with long-range interactions which is a variation on nearest-neighbour Temperley-Lieb spin chains [78–80]. Although examples of fragmented

long-range models exist in the literature [54, 76, 77], they are generally rare, and our model's rich and unusual symmetry structure makes it of particular interest. We derive numerous analytic results for this system, characterising its fragmentation structure in detail and highlighting its associations with other well-known condensed matter models such as Temperley-Lieb spin chains and Sachdev-Ye models. We also discuss perturbations of the model, including one which endows it with a large number of quantum many-body scars.

The second example is a general class of quantum chains with strictly local interactions that conserve a global charge and its dipole moment. As discussed, these models, which are classically fragmented, were the first known examples of fragmented systems [31–33]. Furthermore, they undergo a continuous phase transition between non-thermalising (strongly fragmented) and thermalising (weakly fragmented) phases as the charge density is varied [41, 42]. We show via analytic and numerical results that these models have a "universal" critical charge density that only depends on the local range k of interactions, and not on the details of the dynamics or on the onsite Hilbert space dimension. To this end, we develop several innovative approaches for analysing the models' strongly and weakly fragmented phases, giving us a high level of analytic understanding of the ergodicity-restoring phase transition. We also consider special-case "frozen" models, which are strongly fragmented at all charge densities and do not have a phase transition.

The main body of the thesis is organised as follows. In Chapter 2, we provide a general introduction to Hilbert space fragmentation, thermalisation in quantum systems, and other related topics. In Chapter 3, we study the Hilbert space fragmentation present in the quantum-fragmented long-range variation on Temperley-Lieb chains discussed above. This chapter is based on [1]. In Chapter 4, we present our analysis of the non-thermalising and thermalising phases that occur in locally interacting dipole-conserving chains and also examine the transition between them. This chapter is based on [2]. In Chapter 5, we analyse frozen dipole-conserving models where no phase transition occurs. This chapter is based in part on [2]. We provide concluding remarks in Chapter 6.

2

Hilbert Space Fragmentation

In this chapter, we provide an introduction to Hilbert space fragmentation with examples. We begin with a short review of thermalisation and the eigenstate thermalisation hypothesis (ETH) in Section 2.1. We define Hilbert space fragmentation (HSF) in Section 2.2 using the bond and commutant algebra formalism of [34]. We provide two basic examples of fragmented models in Section 2.3, both of which are related to models we study in more detail later in this thesis. We conclude with a short review of quantum many-body scars in Section 2.4.

2.1 Thermalisation and ETH in Quantum Systems

Here we present a very brief review of thermalisation and the eigenstate thermalisation hypothesis in quantum systems. For a more in-depth review, the reader is directed to [3–6].

An interacting isolated quantum many-body system is said to be "thermal" if the long-time expectation values of local observables in the model are found to coincide with the predictions of standard thermodynamic ensembles. More precisely, say we start with some "simple" initial state $|\psi_0\rangle$ of a thermal system, where by simple we mean a low-entanglement or product state. We time-evolve the system according to the system's Hamiltonian H to a state $|\psi(t)\rangle = e^{-iHt}|\psi_0\rangle$ at some late time t. Consider then an arbitrary local subsystem $\mathcal{S}$, such that $V_{\mathcal{S}} \ll V$ (where

$V_{\mathcal{S}}$ and V are the volumes of the subsystem and overall system respectively), and let O be some few-body observable acting within $\mathcal{S}$. We then have that

$$\langle\psi(t)|\, O\, |\psi(t)\rangle = \mathrm{Tr}(\rho_{\mathcal{S}}(t)O), \tag{2.1}$$

where $\rho_{\mathcal{S}} = \mathrm{Tr}_{\mathcal{S}^c}(|\psi(t)\rangle\langle\psi(t)|)$ is the reduced density matrix obtained by tracing out $\mathcal{S}^c$, the orthogonal complement of $\mathcal{S}$. In a (sufficiently large) thermal system, we expect that

$$\lim_{t\to\infty} \mathrm{Tr}(\rho_{\mathcal{S}}(t)O) = \mathrm{Tr}(\rho_{\mathrm{eq}}(\beta)O), \tag{2.2}$$

where $\rho_{\mathrm{eq}}(\beta) = \frac{1}{Z}e^{-\beta H}$ is a Gibbs density matrix (with H as above being the system's Hamiltonian) and hence $\mathrm{Tr}(\rho_{\mathrm{eq}}(\beta)O) \equiv \langle O\rangle_{\mathrm{mc}}$ is the thermal expectation value of O in the microcanonical ensemble. The inverse temperature β can be determined by computing

$$\langle\psi_0|\, H\, |\psi_0\rangle = \mathrm{Tr}(\rho_{\mathrm{eq}}(\beta)H). \tag{2.3}$$

A thermal system therefore acts as a "heat bath" for its subsystems, bringing them to a thermal state that is in equilibrium with the rest of the system. For models with additional conserved quantities, the equilibrium density matrix is modified to include a grand canonical ensemble taking the conservation laws into account.

The above properties further imply that in thermal systems, subsystems try to maximise their entanglement with the bulk of the system. The entanglement between the subsystem $\mathcal{S}$ and its complement $\mathcal{S}^c$ can be measured by the von Neumann entanglement entropy, given by $S(\rho_{\mathcal{S}}) = -\mathrm{Tr}(\rho_{\mathcal{S}}\log\rho_{\mathcal{S}})$. In thermal systems, we expect that $\lim_{t\to\infty} S(\rho_{\mathcal{S}}(t)) \propto V_{\mathcal{S}}$, meaning that the entanglement entropy grows extensively as a volume law with subsystem size. A hallmark of non-thermal behaviour is when area-law entanglement entropy scaling is found for states with energies in the bulk of the spectrum, showing thermalisation is not occurring.

The eigenstate thermalisation hypothesis (ETH) takes the above conjectures further, and supposes that in thermal systems, thermalisation must also occur at the level of individual eigenstates. Hence, for $|E\rangle$ an eigenstate of H, we

would also expect that $\mathrm{Tr}(|E\rangle\langle E|\, O) = \mathrm{Tr}(\rho_{\mathrm{eq}}(\beta_E)O)$, with β_E determined using Eq. (2.3) as before. This furthermore implies that we should expect volume-law entanglement growth in subsystems of individual eigenstates of ETH-satisfying systems, particularly for eigenstates with energies in the bulk of the spectrum. This will prove a key diagnostic tool for violations of ETH in the upcoming chapters.

ETH also makes predictions for the content of "off-diagonal" elements of few-body observables O. Let $\{|E_n\rangle\}$ be an eigenbasis for our system. The on-diagonal and off-diagonal predictions of ETH can then be summarised in the equation

$$\langle E_m|\, O\, |E_n\rangle = \langle O\rangle_{\mathrm{mc}}\delta_{m,n} + R_{m,n}e^{-S(E)/2}f_O(E,\omega), \tag{2.4}$$

where the eigenstates $|E_n\rangle$ and $\langle E_m|$ have the same symmetry quantum numbers, $E = (E_m + E_n)/2$, $\omega = E_n - E_m$, $\langle O\rangle_{\mathrm{mc}} = \mathrm{Tr}(\rho_{\mathrm{eq}}(\beta_E)O)$ is the thermal expectation value at inverse temperature β_E determined via Eq. (2.3), $S(E)$ is the thermodynamic entropy at energy E, $f_O(E,\omega)$ is a smooth function of its arguments that doesn't scale with system size, and $R_{m,n}$ is a random variable with zero mean and unit variance. Hence, ETH predicts that off-diagonal values of few-body observables will be exponentially suppressed in the thermodynamic entropy.

Violations of ETH can be divided into strong and weak violations. ETH is weakly violated if there exists a measure-0 set of eigenstates that do not respect it. This can happen, for example, due to the presence of non-thermal quantum many-body scar states, which we discuss in more detail in Section 2.4. ETH is strongly violated if almost all eigenstates violate ETH. This can arise due to Hilbert space fragmentation, as we will discuss in Section 2.2, or due to other phenomena such as Anderson localisation [5, 7, 8]. For models that possess one or more global symmetries, the extent to which ETH is violated must be assessed individually in the different quantum number sectors of those symmetries. As we will see in the models examined in Chapters 3, 4, and 5, symmetry sectors where ETH is satisfied, weakly violated, and strongly violated can all be present within a same Hilbert space of a given Hamiltonian.

2.2 Defining Hilbert Space Fragmentation

In this thesis, we adopt the definition of Hilbert space fragmentation in terms of bond and commutant algebras originally proposed in [34]. We summarise this formalism here.

Say we are considering a family of Hamiltonians of the general form $H = \sum_j J_j h_j$, where the h_j are few-body (not necessarily local) operators and the J_j are arbitrary coefficients. We define the bond algebra $\mathcal{A}$ to be the algebra generated by these few-body operators:

$$\mathcal{A} = \langle\!\langle \{h_j\} \rangle\!\rangle, \tag{2.5}$$

where $\langle\!\langle \ldots \rangle\!\rangle$ denotes the associative algebra generated by linear combinations with complex coefficients of arbitrary products of the enclosed elements and the identity operator. Alternatively, if instead of a family of Hamiltonians H we were considering unitary circuits of the form $U = \prod_j \exp(-iJ_j h_j)$, the above definition of $\mathcal{A}$ would still hold.

Let $\mathcal{L}(\mathcal{H})$ denote the set of all linear operators on the Hilbert space $\mathcal{H}$. Clearly $\mathcal{A}$ is a subalgebra of $\mathcal{L}(\mathcal{H})$. We then define the corresponding commutant algebra $\mathcal{C}$ to be the centraliser of $\mathcal{A}$ in $\mathcal{L}(\mathcal{H})$, i.e. the algebra $\mathcal{C}$ is defined as being constituted of all operators which commute with each of the generators of the bond algebra individually:

$$\mathcal{C} = \left\{ O \in \mathcal{L}(\mathcal{H}) \middle| [h_j, O] = 0 \ \forall j \right\}. \tag{2.6}$$

It is clear that $\mathcal{C}$ is also an associative algebra, i.e. products and sums of operators in $\mathcal{C}$ are themselves in $\mathcal{C}$. It is also plain that $\mathcal{A}$ and $\mathcal{C}$ are both closed under Hermitian conjugation of operators, and both contain the identity $\mathbb{1}$. This makes them both examples of von Neumann algebras [81, 82]. As a result, we may apply the bicommutant theorem to them, which states that if $\mathcal{C}$ centralises $\mathcal{A}$ in $\mathcal{L}(\mathcal{H})$, then $\mathcal{A}$ must also centralise $\mathcal{C}$. Since $\mathcal{A}$ and $\mathcal{C}$ centralise each other, we may

construct a virtual bipartition of $\mathcal{H}$ in which we decompose it into representations of $\mathcal{A}$ and $\mathcal{C}$ [83, 84]:

$$\mathcal{H} = \bigoplus_{\lambda} \left(\mathcal{H}_{\lambda}^{(\mathcal{A})} \otimes \mathcal{H}_{\lambda}^{(\mathcal{C})} \right), \tag{2.7}$$

where $\mathcal{H}_{\lambda}^{(\mathcal{A})}$ and $\mathcal{H}_{\lambda}^{(\mathcal{C})}$ are irreps (irreducible representations) of $\mathcal{A}$ and $\mathcal{C}$ respectively, with dimensions D_λ and d_λ. In this decomposition, operators in $\mathcal{A}$ will only act non-trivially on the degrees of freedom in the $\mathcal{H}_{\lambda}^{(\mathcal{A})}$, i.e. any operator $O_{\mathcal{A}} \in \mathcal{A}$ will have a matrix representation $O_{\mathcal{A}} = \oplus_\lambda (M^\lambda(O_{\mathcal{A}}) \otimes \mathbb{1})$ where the $M^\lambda(O_{\mathcal{A}})$ are D_λ-dimensional matrices. Likewise, operators $O_{\mathcal{C}} \in \mathcal{C}$ will have a matrix representation $O_{\mathcal{C}} = \oplus_\lambda (\mathbb{1} \otimes N^\lambda(O_{\mathcal{C}}))$, where the $N^\lambda(O_{\mathcal{C}})$ are d_λ-dimensional matrices. Furthermore, $\mathcal{A}$ and $\mathcal{C}$ respectively act in each $\mathcal{H}_{\lambda}^{(\mathcal{A})}$ and $\mathcal{H}_{\lambda}^{(\mathcal{C})}$ as the full matrix algebras of $D_\lambda \times D_\lambda$ and $d_\lambda \times d_\lambda$ matrices. Hence, for each λ, it is possible to construct a tensored basis $\{|u_{\lambda,\alpha}\rangle \otimes |v_{\lambda,\beta}\rangle\}_{\alpha,\beta=1}^{\alpha=D_\lambda,\beta=d_\lambda}$ such that the $O_{\mathcal{A}}$ act as the matrix algebra on the $|u_{\lambda,\alpha}\rangle$ and the $O_{\mathcal{C}}$ act as the matrix algebra on the $|v_{\lambda,\beta}\rangle$.

The bipartite decomposition in Eq. (2.7) can be used to characterise the different Krylov subspaces of the model in question. Since the Hamiltonian is an element of the bond algebra, it only acts on the $|u_{\lambda,\alpha}\rangle$ in the $\mathcal{H}_{\lambda}^{(\mathcal{A})}$. Thus each state $|v_{\lambda,\beta}\rangle$ in the $\mathcal{H}_{\lambda}^{(\mathcal{C})}$ corresponds to a different Krylov subspace, as the Hamiltonian cannot map from one state $|v_{\lambda,\beta}\rangle$ to another. The total number K of Krylov subspaces is therefore

$$K = \sum_{\lambda} d_\lambda. \tag{2.8}$$

We note that a given decomposition into Krylov subspaces performed according to this method will not necessarily be unique, as there will be more than one choice of basis $|v_{\lambda,\beta}\rangle$ for degenerate Krylov subspaces with $d_\lambda > 1$. However, the total number K is independent of this choice.

For a simple example of a commutant algebra taken from [34], we may consider the spin-1/2 XXZ chain with a random onsite magnetic field:

$$H = \sum_{j=1}^{L} [J_j^x (\sigma_j^x \sigma_{j+1}^x + \sigma_j^y \sigma_{j+1}^y) + J_j^z \sigma_j^z \sigma_{j+1}^z] + \sum_{j=1}^{L} c_j \sigma_j^z, \tag{2.9}$$

where the J_j^x, J_j^z, and c_j are arbitrary coefficients. It's clear that each few-body term $\sigma_j^x\sigma_{j+1}^x + \sigma_j^y\sigma_{j+1}^y$, $\sigma_j^z\sigma_{j+1}^z$, and σ_j^z in the above Hamiltonian will commute with the total spin operator $\sigma_{\text{tot}}^z = \sum_j \sigma_j^z$, endowing the model with a U(1) symmetry. Hence, the model's commutant algebra is given by

$$\mathcal{C} = \text{span}\{\mathbb{I}, \sigma_{\text{tot}}^z, (\sigma_{\text{tot}}^z)^2, \ldots, (\sigma_{\text{tot}}^z)^L\}. \tag{2.10}$$

We note that any higher powers of σ_{tot}^z than $(\sigma_{\text{tot}}^z)^L$ would be linearly dependent on the terms in Eq. (2.10). The Krylov subspaces arising from the irrep decomposition in Eq. (2.7) thus correspond to different values of the total spin. Since this commutant algebra is abelian, its irreps will be one-dimensional, and hence $d_\lambda = 1$ for all λ in Eq. (2.7).

We define Hilbert space fragmentation as occurring when the number of Krylov subspaces K grows exponentially with system size, i.e. when $\log(K) \sim L$, where L is the system size. This is equivalent to saying fragmentation occurs when $\log(\dim(\mathcal{C})) \sim L$, since $\dim(\mathcal{C}) = \sum_\lambda d_\lambda^2$, and therefore $K \leq \dim(\mathcal{C}) \leq K^2$. Furthermore, we can classify fragmented models as featuring either "classical" or "quantum" fragmentation, depending respectively on whether there exists a product-state basis spanning all of the Krylov subspaces in the decomposition or the Krylov subspaces can only all be spanned by an entangled basis.

The degree of fragmentation present in a model can be either weak or strong depending on the sizes of the Krylov subspaces. Assume first that the model possesses no conventional global symmetries, and let $\mathcal{K}_{\text{max}}$ denote the largest Krylov subspace. A fragmented model is said to be weakly fragmented if

$$\dim(\mathcal{K}_{\text{max}})/\dim(\mathcal{H}) \xrightarrow{L\to\infty} 1. \tag{2.11}$$

In this case, almost all eigenstates belong to the dominant Krylov subspace and presumably satisfy ETH. However, those states which are part of the other non-dominant Krylov subspaces violate ETH. This is because their Krylov subspaces are dynamically disconnected from the bulk of the spectrum, and so expectation

values in those states will not match the predictions of thermal ensembles. Hence ETH is weakly violated in this scenario.

On the other hand, strong fragmentation is defined to occur when

$$\dim(\mathcal{K}_{\max})/\dim(\mathcal{H}) \xrightarrow{L\to\infty} 0. \tag{2.12}$$

This leads to a strong violation of ETH in the spectrum as a whole. However, it is still possible for "Krylov-restricted ETH" to be respected within some of the Krylov subspaces themselves [43]. Krylov subspaces can also exhibit integrability and many-body localisation, and thermal and non-thermal Krylov subspaces can coexist within a same Hilbert space [1, 43, 60, 85].

It should be noted that in models with conventional global symmetries, such as particle-number conservation or SU(M), the degree of fragmentation must be assessed within each quantum number sector of the global symmetries individually, and different quantum number sectors can host different degrees of fragmentation.

2.3 Two Simple Fragmented Models

We now present two examples of Hilbert space fragmentation. The first, in Section 2.3.1, is a simple example arising from embedding a spin-1/2 system into a spin-1 system. This is an example of what we call a "deeply frozen" model, and we will study these in more detail in Chapter 5. The second, in Section 2.3.2, is the paradigmatic example of a dipole-conserving chain with local interactions. These are discussed in depth in Chapter 4.

2.3.1 Example 1: An Embedded XYZ Chain

In this example, we shall see a simple case where fragmentation comes from defining a spin-chain Hamiltonian that only acts on a subspace of the local Hilbert space on each site. We consider a spin-1 chain, with spin levels $\{-, 0, +\}$ and L sites. We define the usual onsite raising, lowering, and z-spin operators as

$$S_j^+ = |+_j\rangle\langle 0_j| + |0_j\rangle\langle -_j|\,,\; S_j^- = |-_j\rangle\langle 0_j| + |0_j\rangle\langle +_j|\,,\; S_j^z = |+_j\rangle\langle +_j| - |-_j\rangle\langle -_j|\,, \quad \text{for } j = 1, \ldots, L. \tag{2.13}$$

We may then construct "embedded" spin-1/2 operators as

$$\tilde{\sigma}_j^x = (S_j^+)^2 + (S_j^-)^2,\ \tilde{\sigma}_j^y = -i(S_j^+)^2 + i(S_j^-)^2,\ \tilde{\sigma}_j^z = S_j^z, \tag{2.14}$$

from which we build an embedded spin-1/2 XYZ chain with a random onsite magnetic field:

$$H = \sum_{j=1}^{L}(J_j^x \tilde{\sigma}_j^x \tilde{\sigma}_{j+1}^x + J_j^y \tilde{\sigma}_j^y \tilde{\sigma}_{j+1}^y + J_j^z \tilde{\sigma}_j^z \tilde{\sigma}_{j+1}^z) + \sum_{j=1}^{L} c_j \tilde{\sigma}_j^z, \tag{2.15}$$

where the J_j^x, J_j^y, J_j^z, and c_j are distinct arbitrary coefficients. It is immediately apparent that $[H, (S_j^z)^2] = 0\ \forall\, j$, with $(S_j^z)^2$ acting as a projector onto the onsite spin-1/2 subspace made of the states $|+_j\rangle$ and $|-_j\rangle$. Hence, the commutant algebra in this case is generated by the $(S_j^z)^2$:

$$\mathcal{C} = \langle\!\langle \{(S_j^z)^2\}_{j=1}^{L} \rangle\!\rangle. \tag{2.16}$$

It is clear that $\dim(\mathcal{C}) = 2^L$, and hence that the model is fragmented. Furthermore, since $\mathcal{C}$ is abelian, all of its irreps have dimension $d_\lambda = 1$, and so $K = 2^L$ as well. In this case, each Krylov subspace corresponds to a different choice of which sites are in the spin-1/2 subspace with spins + and −, and which sites have onsite spin 0 and are hence inactive. As the largest Krylov subspace has dimension 2^L (consisting of the subspace where all sites are in their local spin-1/2 subspace), whereas the total Hilbert space grows as 3^L, the model is strongly fragmented, and is also an example of classical fragmentation. We furthermore note that entanglement entropy growth in these systems for a given initial state is typically limited, as each site with onsite spin 0 dynamically disconnects the regions to its right and left. In Chapter 5, we will see how the study of similar models can lead to a greater understanding of the properties of certain approximately fragmented systems.

2.3.2 Example 2: Dipole-Conserving Chains

We next move on to the richer example of fragmentation in quantum chains with strictly local interactions that conserve a global charge and its dipole moment. These were the first examples of Hilbert-space-fragmented models discovered [31–33]. The

fragmentation in this case is due to kinetic constraints that arise from the interplay of the locality of interactions and the conserved charges. For example, consider a model of hopping hardcore bosons, with an interaction range of $k = 4$:

$$H = \sum_{j=1}^{L-3} J_j h_j, \quad h_j = b_j^\dagger b_{j+3}^\dagger b_{j+2} b_{j+1} + \text{h.c.}, \tag{2.17}$$

where the J_j are arbitrary coefficients and the $b_j^\dagger$, b_j are onsite hardcore-bosonic creation and annihilation operators satisfying the usual commutation relations. Each h_j conserves particle number $N = \sum_j n_j$ and dipole moment $X = \sum_j j n_j$, where $n_j = b_j^\dagger b_j$ and X/N is the centre of mass. Thus for a particle to move in this system there must be another particle within $k = 4$ sites for it to interact with. Hence, particles cannot propagate independently of each other, leading to fractonic dynamics. If we work in a product-state basis, where each state has definite values for the occupation numbers n_j, then we may decompose the various (N, X) symmetry sectors into Krylov subspaces which cannot be dynamically connected by the hopping terms h_j. An example of this decomposition, for a system with $L = 6$ and in the sector $(N = 2, X = 5)$, is shown in Fig. 1.1 in Chapter 1. Since these Krylov subspaces are closed under each h_j in the Hamiltonian, projectors onto the Krylov subspaces are elements of the commutant algebra, and hence this construction of the Krylov subspaces is consistent with our definitions in Section 2.2. To show Hilbert space fragmentation, we therefore need to show that the number of Krylov subspaces obtained via this decomposition grows exponentially with system size.

Following an approach similar to the ones in [33, 43], the simplest way to do this is to enumerate a subset of the "frozen" states in the spectrum. These are product states which are annihilated by each term in the Hamiltonian individually, and hence cannot dynamically evolve (a particularly simple example would be an empty state with $N = 0$). Given a frozen state $|\psi_F\rangle$, we therefore have that $[|\psi_F\rangle\langle\psi_F|, h_j] = 0 \ \forall \ j$, and so $|\psi_F\rangle\langle\psi_F| \in \mathcal{C}$. Hence frozen states form one-dimensional Krylov subspaces and are dynamically disconnected from the rest of the spectrum. To prove fragmentation, it is then sufficient to prove that the number of such frozen states grows exponentially with L.

To this end, let $|\psi_0\rangle$ denote the state composed solely of holes, and consider the states

$$\left|\psi_{a_1 a_2 \ldots a_{\lfloor L/4 \rfloor}}\right\rangle = \left(\prod_{j=1}^{\lfloor L/4 \rfloor} (b_{4j}^\dagger)^{a_j}\right) |\psi_0\rangle \,,$$

where the indices a_j take values in $0, 1$. There are $2^{\lfloor L/4 \rfloor}$ different possible choices for these indices, and each choice yields a different frozen state, since the particles in each $\left|\psi_{a_1 a_2 \ldots a_{\lfloor L/4 \rfloor}}\right\rangle$ are too far apart to interact with each other in a system with range $k = 4$ interactions. Thus $\dim(\mathcal{C}) \geq 2^{\lfloor L/4 \rfloor}$, indicating Hilbert space fragmentation. We note that the above derivation can also be used if the range k of interactions or the onsite Hilbert space dimension d are increased, with the general result $\dim(\mathcal{C}) \geq 2^{\lfloor L/k \rfloor}$.

Of course, Krylov subspaces of dimension greater than 1 also exist in these models. The degree of fragmentation (strong vs weak) present in the various (N, X) symmetry sectors is closely linked to the charge density $\nu \equiv N/L$. At very low (or very high) densities ν, particle mobility is highly restricted as particles (or holes) will be very isolated from each other. The individual Krylov subspaces will then tend to be quite small, and most states will be in strongly fragmented (N, X) sectors. On the other hand, for values of the filling ν close to half-filling, particles have much more freedom of movement as each particle will usually have several nearby particles with which to interact. States at these fillings will therefore typically be in weakly fragmented (N, X) sectors. We analyse these properties in detail in Chapter 4, where we study the phase transition such models undergo from a strongly fragmented non-thermalising phase to a weakly fragmented thermalising phase as ν is varied.

2.4 Quantum Many-Body Scars

We now review an alternate scenario in which weak violations of ETH can arise. Quantum many-body scars (QMBS) are, broadly speaking, rare ETH-violating eigenstates in an otherwise ETH-respecting spectrum [6, 12–15]. By "rare", we mean that for an ETH-violating state to be considered a quantum many-body scar, the total set of ETH-violating eigenstates in the Hilbert space must form

a measure-0 subset of the Hilbert space as a whole (when global symmetries are present, the rarity of ETH-violating states must instead be assessed separately in each of the individual symmetry sectors). Quantum many-body scars were experimentally discovered via the observation of anomalously long-lived revivals in a Rydberg-atom quantum simulator [12]. These revivals were attributed to the presence of a small set of nonthermal eigenstates in the spectrum of the PXP model describing the physics of the experiment [13, 16]. Quantum many-body scars were independently discovered analytically in the spin-1 AKLT model [17, 18], which was shown to possess a "tower" of exact ETH-violating eigenstates with equally spaced eigenvalues. QMBSs have been found since then in a range of other models as well, such as domain-wall-conserving models [20], an extended Hubbard model [21], models with "rainbow states" [22], and transverse-field Ising models [23]. Furthermore, several unifying formalisms have been proposed which identify common structures between QMBSs arising in different models [24–30]. Further details can be found in the review articles [6, 14, 15].

In [30], it was noted that many examples of quantum many-body scars in local Hamiltonians can also be characterised using the commutant algebra formalism. Assuming that global symmetries have been resolved, let $\mathcal{H}_n$ denote the resolved Hilbert spaces of the various symmetry sectors, and for each of these let $\mathcal{K}_{n,\max}$ denote the largest Krylov subspace. Two conditions are together sufficient for an eigenstate $|\psi_{\text{scar}}\rangle$ to be a quantum many-body scar, namely

$$|\psi_{\text{scar}}\rangle\langle\psi_{\text{scar}}| \in \mathcal{C} \ , \qquad \frac{\dim(\mathcal{K}_{n,\max})}{\dim(\mathcal{H}_n)} \xrightarrow{L\to\infty} 1, \tag{2.18}$$

where $\mathcal{C}$ is a non-trivial commutant algebra. The first condition ensures that the scar state violates ETH, since it implies that the scar state is an eigenstate of a family of Hamiltonians, whereas ETH-obeying eigenstates generically have a unique parent Hamiltonian [30, 86, 87]. The second condition ensures that the scar state is a rare exception in a symmetry sector dominated by thermal eigenstates. We note that $|\psi_{\text{scar}}\rangle$ need not have area-law entanglement entropy [22, 30]. Additionally, if the number of scars in a model grows exponentially with system size L, then

by Eq. (2.18) the dimension of the commutant algebra grows exponentially as well, leading to Hilbert space fragmentation. The fragmentation in this case is weak, because the second condition of Eq. (2.18) says that the symmetry sectors containing scars are dominated by individual large Krylov subspaces. We note that the frozen states of the dipole-conserving models introduced in Section 2.3.2 are good candidates for quantum many-body scar states, as they satisfy the first condition of Eq. (2.18). Whether or not they are scars then depends on if they are situated in strongly fragmented symmetry sectors (in which case they violate the second condition of Eq. (2.18) and are not scars) or weakly fragmented symmetry sectors (in which case they satisfy Eq. (2.18) and are scars).

In the following chapter, we study a quantum system where the fragmentation is entirely due to the presence of an exponentially growing number of states that satisfy the first condition in Eq. (2.18). However, none of the states constitute QMBSs as they are all situated in symmetry sectors that do not have a large thermal subspace. We will show that by perturbing the model in question and destroying its global symmetries, we can endow it with a large thermal subspace. Hence the states in question become QMBSs of the perturbed model.

3

Bipartite Sachdev-Ye Models with Read-Saleur Symmetries

In this chapter, we introduce an SU(M)-symmetric bipartite spin model which exhibits Hilbert space fragmentation even in the presence of random and long-range couplings. As such, it offers a rare example of a fragmented system that is intrinsically "zero-dimensional", i.e. without a notion of spatial distance. This is in stark contrast with, for example, the dipole-conserving spin chains discussed in Section 2.3.2, where the strict locality of interactions is a crucial ingredient for fragmentation. Although some examples of non-local fragmented models exist in the literature [54, 76, 77], they are scarce. Indeed, it is in general more "challenging" for a model with non-local interactions to be fragmented than a 1D local model because non-local models possess a higher number of terms in their Hamiltonian. As such, they have significantly more generators for their bond algebra (2.5). This places strong constraints on the dimension of the commutant algebra (2.6) of long-range models. Nonetheless, the non-local model we present here has a non-trivial commutant algebra with a rich underlying structure, leading to fragmentation. This chapter is based on the work published in [1].

The model we study is composed of $2N$ spins, half of which are in the fundamental $\mathbf{M}$ representation of SU(M), and half of which are in its conjugate $\overline{\mathbf{M}}$. The Hamiltonian consists of a sum over projectors onto the spin-singlet state for each

$\mathbf{M}, \overline{\mathbf{M}}$ pair. This Hamiltonian constitutes a long-range generalisation of the nearest-neighbour Temperley-Lieb spin chains, such as the "biquadratic" spin-1 chain [80, 88]. Temperley-Lieb chains are notable for being the first known examples of "quantum" Hilbert-space-fragmented models, where the Krylov subspace decomposition can only be performed in an entangled basis [34]. The fragmentation stems from the chains' large commutant algebra, which was first derived by Read and Saleur and which leads to large degeneracies throughout the models' spectra for $M \geq 3$ [78]. As we shall see, some of the Read-Saleur commutant algebra survives the generalisation to long-range interactions, leading to HSF in the model we introduce in this chapter.

This chapter is organised as follows. In Sec. 3.1, we define our Hamiltonian in more detail and demonstrate its key properties. We provide a simple proof that the Hamiltonian has a nullspace whose dimension grows exponentially with increasing system size for $M \geq 3$ in SU(M). As we shall discuss, states in this nullspace are frustration-free, i.e. are annihilated by each of the projectors in the Hamiltonian. Hence, projectors onto these nullstates are part of the commutant algebra, implying the model is fragmented. We also compare our model to the Sachdev-Ye model [89, 90], an SU(M)-symmetric all-to-all model with several similarities to our system but which is not Hilbert-space-fragmented.

In Sec. 3.2, we solve the uniform-coupling version of our model, and use this solution to derive an exact formula for the dimension of the nullspace of the full model. We show that the fragmented sectors can be identified solely by the SU(M) symmetry: states in certain SU(M) representations are always part of the nullspace, whereas those in other representations never belong to the nullspace. As a result, some of the SU(M) quantum number sectors are entirely composed of nullstates and hence exhibit strong HSF. We also explore the impact of SU(M)-symmetric perturbations on the fragmentation structure of the model, as well as generalisations of the model in which spins in antisymmetric representations of SU(M) on each site are considered.

The large nullspace our model possesses arises as a consequence of a non-trivial commutant algebra, which we discuss in Sec. 3.3. This algebra is a subalgebra of

the Read-Saleur (RS) algebra [78], whose elements commute with all the generators of certain representations of the Temperley-Lieb algebra, including those used to build the nearest-neighbour analogs of our model [34]. Remarkably, here we find that some of the HSF and the commutant algebra present in the nearest-neighbour chains survive their generalisation to our model. This is in spite of the fact that much of the structure of the Temperley-Lieb algebra is destroyed by the generalisation to long-range interactions.

In Sec. 3.4, we show how to modify our Hamiltonian using a long-range variant of Shiraishi-Mori spectral embedding [24]. The product states in the nullspace are then spread throughout the spectrum and constitute quantum many-body scars. The existence of these states results in weak fragmentation and a weak violation of ETH in the modified model, and the scars can be arranged so as to lead to periodic revivals, a hallmark of scars in experimental setups.

We provide concluding remarks in Sec. 3.5.

3.1 Basic Properties

In this section, we introduce our Hamiltonian H_M and derive some of its key properties. We explain how it can be thought of as a bipartite version of the well-known Sachdev-Ye model, an all-to-all SU(M)-symmetric model. Despite the resemblance, we show that it has certain significantly different properties. Namely, we demonstrate that the dimension of the nullspace of H_M grows exponentially with increasing system size. The states in this nullspace are frustration-free and correspond to ground states for ferromagnetic couplings. A consequence is that our model is Hilbert-space-fragmented, with each map between two nullspace eigenstates constituting an element of the commutant algebra.

3.1.1 Defining The Hamiltonian

We study a spin-S SU(M)-symmetric bipartite system, with $M = 2S + 1$. The system is composed of $2N$ spins, with N spins transforming in the fundamental representation $\mathbf{M}$ of SU(M) and N transforming in the conjugate representation

$\overline{\mathbf{M}}$. We will usually label the spins of the former by upper indices i and of the latter by lower indices j with $1 \leq i, j \leq N$. The corresponding states for each spin are labeled respectively as $|a^i\rangle$ and $|a_j\rangle$ with $1 \leq a \leq M$. We work in a basis where the symmetry generators are built from operators acting on a given spin as

$$T_b^{a,i} = \left|a^i\right\rangle\!\left\langle b^i\right|, \qquad S_{b,j}^a = -\left|b_j\right\rangle\!\left\langle a_j\right| \ , \tag{3.1}$$

while acting trivially on the others. The operators

$$J_b^a = \sum_{i=1}^N T_b^{a,i} + \sum_{j=1}^N S_{b,j}^a. \tag{3.2}$$

generate a $U(M)$ algebra, but the $U(1)$ generator $\sum_a J_a^a$ vanishes on any state in our Hilbert space. Thus effectively the symmetry is SU(M).

We study a bipartite model with two-spin interactions between each pair (i,j) with i in the $\mathbf{M}$ half and j in the $\overline{\mathbf{M}}$ half. The spins in each half do not interact amongst themselves. The SU(M)-invariant two-spin interaction can be written in terms of the (unnormalised) projector onto a singlet, which is given in this basis by

$$P_j^i = -\sum_{a,b=1}^M T_b^{a,i} S_{a,j}^b = \sum_{a,b=1}^M \left|a^i a_j\right\rangle\!\left\langle b^i b_j\right| \ . \tag{3.3}$$

The eigenstate of P_j^i with non-vanishing eigenvalue M is

$$\left|\psi_j^{0,i}\right\rangle = \sum_{a=1}^M \left|a^i a_j\right\rangle \ . \tag{3.4}$$

The most general such Hermitian Hamiltonian is comprised of a sum over singlet projectors for each pair with arbitrary real coefficients r_j^i:

$$H_M = \sum_{i,j=1}^N r_j^i P_j^i \ . \tag{3.5}$$

For $M = 2$, the projector is the usual spin-$\frac{1}{2}$ Heisenberg interaction. When $M = 3$, the Hamiltonian can be rewritten in terms of the "biquadratic" spin-1 interaction. Namely, we let $\boldsymbol{S}^i = ((S^x)^i, (S^y)^i, (S^z)^i)$ denote the usual spin-1 SU(2) generators acting on spin i, and likewise for $\boldsymbol{S}_j$ acting on spin j. The projector then can be unitarily transformed into

$$\begin{aligned} U_3 P_i^j U_3^\dagger &= (\boldsymbol{S}^i \cdot \boldsymbol{S}_j)^2 - \mathbb{1}, \\ \text{where} \quad U_3 &= \prod_{j=1}^N \exp\left(i\pi S_j^z\right) \exp\left(i\pi S_j^x\right) \ . \end{aligned} \tag{3.6}$$

The nearest-neighbour uniform chain analog of H_M is found by setting $r^i_j = 0$ unless $j = i, i+1$, yielding a chain with $2N$ sites and nearest-neighbour interactions:

$$H_{\text{nn}} = \sum_{i=1}^{N} \left(r^i_i P^i_i + r^i_{i+1} P^i_{i+1} \right) . \tag{3.7}$$

This Hamiltonian has elicited significant academic interest because its generators obey the Temperley-Lieb algebra [80, 88]. With uniform couplings, the model is integrable, and many properties can be computed utilising the XXZ chain whose generators satisfy the same algebra.

Remarkably, H_{nn} has a large commutant algebra whose generators were derived by Read and Saleur (RS) [78]. Each element of this algebra commutes with each projector in Eq. (3.7) individually, and so commutes with H_{nn} for any couplings. For $M = 2$, where H_{nn} is the Heisenberg chain, the commutant algebra is simply SU(2). However, for $M \geq 3$, the dimension of the RS algebra grows exponentially with system size, leading to exponentially large degeneracies in the spectrum. We discuss the RS algebra in more detail in Sec. 3.3.

3.1.2 Hilbert Space Fragmentation

The Hamiltonian H_M with completely arbitrary couplings r^i_j has for $M \geq 3$ a nullspace whose dimension grows exponentially with N. As a consequence, the model exhibits Hilbert space fragmentation. We provide a basic derivation of these facts here. We later derive an exact formula for the dimension of this nullspace in Sec. 3.2, and show how the SU(M) symmetry allows us to precisely characterise the corresponding states. In Sec. 3.3, we furthermore connect this result to the survival of a non-trivial subalgebra of the RS algebra.

Since H_M from Eq. (3.5) is a sum of projectors, its nullspace $\mathcal{N}$ for arbitrary couplings consists of those states annihilated by each projector P^i_j individually. Such states are said to be frustration-free. An exponentially large number of states in $\mathcal{N}$ are product states, and so can be found easily. We write a product state $|\psi_{\mathcal{N}}\rangle$ as

$$|\psi_{\mathcal{N}}\rangle = \otimes \left| t^1 t^2 \dots t^N s_1 s_2 \dots s_N \right\rangle , \tag{3.8}$$

where each $t^i, s_j \in \{1, \ldots, M\}$ denotes the state of the spin i, j in the $\mathbf{M}$ and $\overline{\mathbf{M}}$ irreps respectively. As apparent from (3.3), if we choose t^i and s_j such that

$$t^i \leq z < s_j, \text{ for any } z \in \{1, \ldots, M-1\} \tag{3.9}$$

then $|\psi_{\mathcal{N}}\rangle$ will be annihilated by each projector in Eq. (3.5). The total number of possible values for all the levels t^i and s_j such that the above constraint is satisfied is $(z(M-z))^N$ for each value of z.

It is clear that, for $M \geq 3$, the number of product states in the nullspace obeying (3.9) grows exponentially with N. Since all these product states belong to non-trivial SU(M) multiplets, their number provides a lower bound to the dimension $D_{\mathcal{N}}$ of the nullspace:

$$D_{\mathcal{N}} \geq \sum_{z=1}^{M-1} z^N (M-z)^N \tag{3.10}$$

For N large, this bound is sharply peaked around $z \approx M/2$, so we expect the exponential growth to be

$$D_{\mathcal{N}} \propto \begin{cases} \left(\frac{M}{2}\right)^{2N} & M \text{ even}, \\ \left(\frac{M^2-1}{4}\right)^N, & M \text{ odd}. \end{cases} \tag{3.11}$$

For ferromagnetic couplings ($r^i_j > 0$ for all i and j), each state in the nullspace is a ground state, yielding an exponentially growing ground-state degeneracy.

For $M = 3$, it is also possible to simply derive the polynomial growth order of $D_{\mathcal{N}}$, demonstrating that $D_{\mathcal{N}} \propto 2^N N^2$. This is done by directly constructing a basis spanning a significant fraction of the total nullspace for $M = 3$. We perform this calculation explicitly in Appendix A.1.

For any couplings, the large nullspace results in Hilbert space fragmentation. In its analysis we use the approach of bond and commutant algebras developed in [34] and reviewed in Section 2.2. The bond algebra $\mathcal{A}$ of H_M is generated by the projectors P^i_j and the identity operator, with the elements of $\mathcal{A}$ being given by linear combinations of arbitrary products of the generators. The commutant algebra $\mathcal{C}$ is the algebra of operators O that commute with each generator of $\mathcal{A}$ individually. Since the states in the nullspace $\mathcal{N}$ are annihilated by each P^i_j individually, maps

between them that leave all other states invariant are elements of $\mathcal{C}$. Indeed, for any two nullstates $|\psi_A\rangle, |\psi_B\rangle \in \mathcal{N}$, we have that

$$\left[P_j^i,\, |\psi_A\rangle\langle\psi_B|\right] = 0, \;\; \text{for}\, 1 \leq i,j \leq N, \tag{3.12}$$

and hence $|\psi_A\rangle\langle\psi_B| \in \mathcal{C}$. Therefore $\dim(\mathcal{C}) \geq (\dim(\mathcal{N}))^2$, and so the size of the commutant algebra grows exponentially with N. This leads to Hilbert space fragmentation, with each state in $\mathcal{N}$ constituting its own one-dimensional Krylov subspace. In Sections 3.2.2 and 3.2.3, we derive an exact formula for the dimension of the nullspace and find precisely which SU(M) representations are present in it.

3.1.3 Comparing H_M to the Sachdev-Ye Model

As an SU(M)-symmetric spin model with disordered long-range interactions, H_M is reminiscent of the well-known Sachdev-Ye (SY) model [89, 90]. The SY model is a disordered all-to-all variation on the SU(M)-symmetric Heisenberg model [89], and its Hamiltonian is given by

$$H_{\text{SY}} = \frac{1}{\sqrt{MN}} \sum_{i<j}^{N} \sum_{a,b=1}^{M} g_{ij} \mathcal{S}_{b,i}^{a} \mathcal{S}_{a,j}^{b}, \tag{3.13}$$

where $\mathcal{S}_{b,i}^{a}$ are generators of SU(M) acting non-trivially at site i, and the g_{ij} are independent and identically distributed Gaussian random variables with vanishing means and variances that do not scale with N or M.

The crucial distinction between the SY model and ours is that all sites in the former transform in the same SU(M) irreducible representation. When that representation is the fundamental $\mathbf{M}$, each operator $\mathcal{S}_{b,i}^{a}\mathcal{S}_{a,j}^{b}$ is equal (up to a constant shift) to the permutation operator $\mathbb{P}_{ij}$ swapping the spins on sites i and j. As a consequence, H_{SY} and H_M have different physical properties. The permutation operators $\mathbb{P}^{ij}$ in H_{SY} with sites in $\mathbf{M}$ split the M^2 states into $M(M+1)/2$ (symmetric) and $M(M-1)/2$ (antisymmetric) dimensional subspaces. The singlet-projector operators P_j^i comprising H_M have rank 1, annihilating all but one of the basis states in the M^2-dimensional Hilbert space formed by two spins. It is therefore not surprising that the H_M has a non-trivial nullspace, unlike SY. We would also

expect the ranks of the projectors P^i_j to influence the rest of the spectrum, with H_M having a higher density of states close to energy zero than this SY model. We have checked this behaviour numerically and indeed confirmed it at small N. Some of the numerical results can be found in Appendix A.2.

The SY model is expected to obey ETH, as tested in its fermionic analog, the Sachdev-Ye-Kitaev (SYK) model [91, 92]. A reason is that when all sites are in the fundamental representation, the SY model has the same bond algebra as the SU(M) Heisenberg model. Indeed any $\mathbb{P}_{ij}$ is the product of nearest-neighbour permutation operators, e.g. for $j > i$, $\mathbb{P}_{ij} = \mathbb{P}_{i,i+1}\mathbb{P}_{i+1,i+2}\cdots\mathbb{P}_{j-1,j}$ [93]. The same bond algebra implies the same commutant algebra as well, and including random all-to-all couplings will not increase the symmetry. The SU(M) Heisenberg model for $M > 2$ is not integrable and has no known symmetry algebra beyond SU(M). It therefore obeys ETH, and so the SY model should as well.

3.2 Exact Results

We here obtain the nullspace $\mathcal{N}$ of H_M. As $\mathcal{N}$ is defined as the set of states annihilated by all the projectors, it is independent of the couplings. We thus can find it by solving the "clean" case, where all couplings are the same. In Section 3.2.1, we define the clean model and solve it. In Section 3.2.2, we identify the SU(M) irreps that are in the clean model's nullspace, and hence also in the nullspace of H_M. In Section 3.2.3, we derive an exact formula for the nullspace's exponentially large dimension. In Section 3.2.4, we show that the SU(M) symmetry sectors which contain nullstates are entirely composed of nullstates, and so are strongly fragmented. In Section 3.2.5, we discuss certain SU(M)-symmetric perturbations to the model which preserve its Hilbert space fragmentation. In Section 3.2.6, we discuss a generalisation of H_M where its spins are in antisymmetric representations of SU(M), and show that it is also fragmented.

3.2.1 The Energies of the Clean Model

The clean version of H_M is given by setting all couplings r_j^i in Eq. (3.5) to one:

$$H_{\text{clean}} = \sum_{i,j=1}^{N} P_j^i = -\sum_{i,j=1}^{N}\sum_{a,b=1}^{M} T_b^{a,i} S_{a,j}^b \ . \tag{3.14}$$

This Hamiltonian is invariant under permutations of the N spins in the $\mathbf{M}$ representation amongst themselves, and likewise for those in the $\overline{\mathbf{M}}$. This symmetry enhancement allows the spectrum of H_{clean} to be computed from a purely group-theoretical analysis.

The method for solving H_{clean} is to write it as a sum of Casimir invariants. Any representation of a Lie algebra possesses a quadratic Casimir operator that commutes with all the generators of the algebra in that representation. The full system we are studying is comprised of N spins in the $\mathbf{M}$ representation of SU(M) and N in the $\overline{\mathbf{M}}$, i.e. the representation is $\mathbf{M}^{\otimes N} \otimes \overline{\mathbf{M}}^{\otimes N}$ with generators given in ((3.1),3.2). The corresponding Casimir operator is

$$C_{\mathbf{M}^{\otimes N}\otimes\overline{\mathbf{M}}^{\otimes N}} = \sum_{a,b=1}^{M} J_b^a J_a^b. \tag{3.15}$$

We also need the SU(M) Casimir operators for just the $\mathbf{M}$ spins and for just the $\overline{\mathbf{M}}$ spins, which are

$$\begin{aligned} C_{\mathbf{M}^{\otimes N}} &= \sum_{a,b=1}^{M} \mathcal{T}_b^a \mathcal{T}_a^b = -\frac{N^2}{M} + \sum_{i,j=1}^{N}\sum_{a,b=1}^{M} T_b^{a,i} T_a^{b,j} \,, \\ C_{\overline{\mathbf{M}}^{\otimes N}} &= \sum_{a,b=1}^{M} \mathcal{S}_b^a \mathcal{S}_a^b = -\frac{N^2}{M} + \sum_{i,j=1}^{N}\sum_{a,b=1}^{M} S_{b,i}^a S_{a,j}^b \,, \end{aligned} \tag{3.16}$$

where the SU(M) generators acting on the $\mathbf{M}^{\otimes N}$ and $\overline{\mathbf{M}}^{\otimes N}$ subspaces are respectively

$$\mathcal{T}_b^a = \sum_{i=1}^{N} \Big(T_b^{a,i} - \tfrac{1}{M}\delta_b^a \Big), \quad \mathcal{S}_b^a = \sum_{j=1}^{N} \Big(S_{b,j}^a + \tfrac{1}{M}\delta_b^a \Big),$$

giving traceless operators as needed.

The clean Hamiltonian therefore can be written in terms of these three Casimir operators as

$$H_{\text{clean}} = \tfrac{N^2}{M} + \tfrac{1}{2}\Big(C_{\mathbf{M}^{\otimes N}} + C_{\overline{\mathbf{M}}^{\otimes N}} - C_{\mathbf{M}^{\otimes N}\otimes\overline{\mathbf{M}}^{\otimes N}} \Big). \tag{3.17}$$

Other models consisting of a sum of SU(M) Casimirs have been analyzed [94–97], but all spins in these models are in the **M** representation.

The key property of the quadratic Casimir operator is that for an irreducible representation it is proportional to the identity. Irreducible representations of SU(M) are characterised by an M-dimensional vector $\rho = [\rho_1, \rho_2, \ldots, \rho_M]$ comprised of integers satisfying

$$\rho_1 \geq \rho_2 \geq \ldots \geq \rho_M \geq 0. \tag{3.18}$$

Each such vector can be written as a partition $P_{S,k}$ of $S = \sum_a \rho_a$ into k positive integers, where $k \leq M$. For any partition with $k < M$, we set $\rho_b = 0$ for $b > k$. The vector corresponding to the fundamental **M** representation is [1,0,0,...0], while for the conjugate $\overline{\mathbf{M}}$ it is [1,1,...,1,0]. SU(M) representations related by shifting all $\rho_a \to \rho_a + 1$ or $\rho_a \to \rho_a - 1$ (until $\rho_M = 0$) are equivalent.

The quadratic Casimir operator obeys

$$C_\rho = c_\rho \mathbb{1} \quad \text{for } \rho \text{ irreducible.} \tag{3.19}$$

For any representation of a semisimple Lie algebra, the number c_ρ can be determined by standard techniques. For SU(M), it is [98]

$$c_\rho = \sum_a \Big(\rho_a^2 \ + \ (M + 1 - 2a)\rho_a \Big) - \frac{1}{M} \Big(\sum_a \rho_a \Big)^2. \tag{3.20}$$

where here and everywhere unlabeled sums over a run from 1 to M. The Casimir c_ρ is indeed invariant under the shift $\rho_a \to \rho_a \pm 1$.

Group theory alone yields all the eigenvalues of H_{clean}. Finding them requires decomposing the Hilbert space $\mathbf{M}^{\otimes N} \otimes \overline{\mathbf{M}}^{\otimes N}$ into irreducible representations of SU(M). Since (3.17) involves also the Casimir operators for the two types of spins alone, we must also keep track of the representations of SU(M) in the corresponding subspaces. The simplest way to understand tensor products of SU(M) representations is via Young diagrams. The Young diagram for an irreducible representation ρ is a collection of boxes glued together such that the ath row has ρ_a boxes in it. To take the tensor product of two representations, one glues the

boxes from the corresponding Young diagrams together subject to certain rules (see e.g. [99] or any text on Lie algebras).

We first need to decompose the tensor products $\mathbf{M}^{\otimes N}$ and $\overline{\mathbf{M}}^{\otimes N}$ into a direct sum over irreducible representations λ and $\overline{\gamma}$ respectively, and then decompose the tensor product of each λ and $\overline{\gamma}$ pair. The irreducible representations λ in the decomposition of $\mathbf{M}^{\otimes N}$ obey $\sum_a \lambda_a = N$. They can therefore be written as integer partitions of N into at most M parts:

$$\mathbf{M}^{\otimes N} = \oplus m(\lambda)\, \lambda, \qquad \lambda \in P_{N,k} \text{ for } k \leq M. \tag{3.21}$$

where $m(\lambda)$ is the "multiplicity", the number of times λ appears in this direct sum. We give its value below. The decomposition of $\overline{\mathbf{M}}^{\otimes N}$ can be characterised similarly by taking advantage of conjugate representations. The conjugate $\overline{\gamma}$ is defined via $\overline{\gamma}_a = \gamma_1 - \gamma_{M+1-a}$. The conjugate of a tensor product is the tensor product of the conjugates. We then utilise (3.21) to get

$$\overline{\mathbf{M}}^{\otimes N} = \oplus m(\gamma)\, \overline{\gamma}, \quad \gamma \in P_{N,l} \text{ for } l \leq M. \tag{3.22}$$

Here $\sum_a \overline{\gamma}_a = M\gamma_1 - N$.

To decompose the full Hilbert space into irreducible representations, we then take the tensor product of each pair to give $\lambda \otimes \overline{\gamma} = \oplus \rho$. The Hilbert space thus can be decomposed into sectors labeled by $(\lambda, \overline{\gamma}, \rho)$. The clean Hamiltonian is diagonal in such a basis, with any state $|\psi_{\lambda,\overline{\gamma},\rho}\rangle$ in a given sector obeying

$$H_{\text{clean}} |\psi_{\lambda,\overline{\gamma},\rho}\rangle = \left(\tfrac{N^2}{M} + \tfrac{1}{2}\Big(c_\lambda + c_{\overline{\gamma}} - c_\rho\Big)\right) |\psi_{\lambda,\overline{\gamma},\rho}\rangle \ . \tag{3.23}$$

This spectrum of the clean model is highly degenerate, and below we compute its ground-state degeneracy.

3.2.2 The Ground States of the Clean Model

To find the dimension of the nullspace of H_M, we first construct the states annihilated by H_{clean}. Since eigenvalues of H_{clean} and Casimirs of SU(M) are always non-negative, from (3.23) we have

$$c_\rho \leq 2\tfrac{N^2}{M} + c_\lambda + c_{\overline{\gamma}}, \tag{3.24}$$

with ground states given by those representations $\rho \in \lambda \otimes \overline{\gamma}$ satisfying the equality.

Thus for a given pair $\lambda, \overline{\gamma}$, candidates for ground states must maximise c_ρ. To find this maximum, we exploit a useful inequality for SU(M) representations: for any $\rho \in \lambda \otimes \overline{\gamma}$, then [100]

$$\sum_{a=1}^{b} \left(\lambda_a + \overline{\gamma}_a\right) \geq \sum_{a=1}^{b} \rho_a \tag{3.25}$$

for any b. It follows from the explicit expression (3.20) that this c_ρ is maximised when ρ obeys the equality in (3.25), i.e. $\rho = \lambda + \overline{\gamma}$. Here the Young diagram for ρ is given by gluing those for λ and $\overline{\gamma}$ together horizontally.

The zero-energy ground states of H_{clean} are therefore those $\boldsymbol{\lambda}$ and $\overline{\boldsymbol{\gamma}}$ for which

$$c_{\boldsymbol{\lambda}+\overline{\boldsymbol{\gamma}}} = 2\tfrac{N^2}{M} + c_{\boldsymbol{\lambda}} + c_{\overline{\boldsymbol{\gamma}}}. \tag{3.26}$$

By construction $\sum_a \boldsymbol{\lambda}_a = N$ and $\sum_a \overline{\boldsymbol{\gamma}}_a = M\boldsymbol{\gamma}_1 - N$, so that (3.20) yields

$$\begin{aligned} c_{\boldsymbol{\lambda}+\overline{\boldsymbol{\gamma}}} - c_{\boldsymbol{\lambda}} - c_{\overline{\boldsymbol{\gamma}}} &= 2\sum_a \boldsymbol{\lambda}_a \overline{\boldsymbol{\gamma}}_a - 2N\boldsymbol{\gamma}_1 + 2\tfrac{N^2}{M} \\ &= -2\sum_a \boldsymbol{\lambda}_a \boldsymbol{\gamma}_{M+1-a} + 2\tfrac{N^2}{M} \ . \end{aligned} \tag{3.27}$$

The condition (3.26) then reduces to

$$\sum_a \boldsymbol{\lambda}_a \boldsymbol{\gamma}_{M+1-a} = 0 \ . \tag{3.28}$$

In (3.21,3.22) we defined λ and γ as partitions of N. Since both $\boldsymbol{\lambda}_a$ and $\boldsymbol{\gamma}_{M+1-a}$ are non-negative, one of these two must vanish for all a for (3.28) to be satisfied.

The condition (3.28) therefore is equivalent to the remarkably simple constraint $k + l \leq M$. We thus find that the ground states of H_{clean} and the nullspace of H_M are all those $|\psi_{\boldsymbol{\lambda},\overline{\boldsymbol{\gamma}},\boldsymbol{\lambda}+\overline{\boldsymbol{\gamma}}}\rangle$ with

$$\boxed{\boldsymbol{\lambda} \in P_{N,k}, \quad \boldsymbol{\gamma} \in P_{N,l}, \quad k + l \leq M.} \tag{3.29}$$

This constraint is both necessary and sufficient for obtaining a zero-energy ground state of H_{clean}.

We thus have proved that the Hilbert space of H_M is fragmented: all states satisfying (3.29) are part of the nullspace. Since there are many such SU(M)

representations, this degeneracy goes well beyond the consequences of this global symmetry. In section 3.2.4, we prove an even stronger statement: any state in a representation ρ that obeys $\rho = \boldsymbol{\lambda} + \overline{\boldsymbol{\gamma}}$ is in the nullspace, as long as $\boldsymbol{\lambda}$ and $\boldsymbol{\gamma}$ satisfy the conditions of (3.29). Hence, those SU(M) quantum number sectors which contain nullstates are strongly fragmented as they are entirely composed of 1D Krylov subspaces.

3.2.3 Exact Dimension of the Nullspace

We present here an exact formula for the dimension of the nullspace $\mathcal{N}$ of H_M as a function of M and N. As discussed in section 3.1.2, all states in the nullspace are annihilated by each projector P_j^i. Because H_{clean} is a sum over these projection operators with positive coefficients, its eigenvalues are non-negative, and all eigenstates with zero eigenvalue are annihilated by all P_j^i. Hence the nullstates for any r_j^i are given by the zero-energy ground states of the clean model. We therefore may make use of the solution of the latter to derive the nullspace dimension $D_{\mathcal{N}}$, which follows from purely group-theoretical calculations.

The nullspace is spanned by all the states in (3.29). The multiplicities $m(\boldsymbol{\lambda})$ and $m(\boldsymbol{\gamma})$ in (3.21,3.22) give rise to one kind of degeneracy: any of the copies of $\boldsymbol{\lambda}$ and $\overline{\boldsymbol{\gamma}}$ can be used to make $\rho = \boldsymbol{\lambda} + \overline{\boldsymbol{\gamma}}$. The second kind of degeneracy comes from the fact that any of the states in the ρ representation give rise to a ground state. The number of these is $d(\boldsymbol{\lambda} + \overline{\boldsymbol{\gamma}})$, the dimension of this representation. The resulting number of ground states, and hence the dimension of the nullspace $\mathcal{N}$, is then

$$D_{\mathcal{N}} = \sum_{\substack{k,\ell=1 \\ k+\ell\leq M}}^{M-1} \sum_{\boldsymbol{\lambda}\in P_{N,k}} \sum_{\boldsymbol{\gamma}\in P_{N,\ell}} m(\boldsymbol{\lambda}) m(\boldsymbol{\gamma}) d(\boldsymbol{\lambda} + \overline{\boldsymbol{\gamma}}), \tag{3.30}$$

which indicates that this degeneracy is significantly greater than can be explained via any obvious symmetry of the model.

The multiplicities and dimensions of these representations follow from standard group-theory methods. The N spins in the $\mathbf{M}$ representation are exchanged amongst each other by elements of the permutation group S_N, which in the clean model is a symmetry. The multiplicities $m(\boldsymbol{\lambda})$ in (3.21) are given by the dimension of the

corresponding irreducible representation of S_N. Both this representation and the SU(M) representation $\boldsymbol{\lambda}$ are labeled by the same Young diagram, a fact known as Schur-Weyl duality. The dimension of an S_N representation is given by

$$m(\boldsymbol{\lambda}) = \frac{N!}{h(\boldsymbol{\lambda})}, \qquad h(\boldsymbol{\lambda}) \equiv \prod_{a,b} h_{a,b} \tag{3.31}$$

where $h_{a,b}$ denotes the "hook length" of the box at row a, column b of the Young diagram for $\boldsymbol{\lambda}$, and the product in $h(\boldsymbol{\lambda})$ is over all boxes. A hook comprises the box (a,b), all the boxes to the right of it in the same row a, and all the boxes below it in the same column b. The hook length $h_{a,b}$ is the number of such boxes. The dimension $d(\rho)$ of a SU(M) representation also involves the product of hook lengths. It is

$$d(\rho) = \frac{1}{h(\rho)} \prod_{a=1}^{M} \frac{(\rho_a + M - a)!}{(M-a)!} \tag{3.32}$$

For $M=2$, the formula (3.30) exhibits no great surprises. Here both k and l must be 1, and the only partition $P_{N,1}$ is $[N,0]$, which has $m([N,0])=1$. The corresponding SU(2) representation has dimension $d([2N,0]) = 2N+1$, so we find $D_{\mathcal{N}} = 2N+1$, the dimension of the usual ferromagnetic multiplet.

As we noted in (3.11), for $M \geq 3$ the nullspace dimension grows exponentially with N. For $M=3$ the precise asymptotic is

$$D_{\mathcal{N}}\Big|_{M=3} \approx \frac{9}{4}\, 2^N N^2 \quad \text{for large } N. \tag{3.33}$$

The derivation of (3.33) was done in collaboration with Paul Fendley [1], and is as follows. We first note that using the explicit expressions (3.31,3.32) for the multiplicities and the dimension in the exact formula (3.30) for $M=3$ yields

$$\begin{aligned} D_{\mathcal{N}}\Big|_{M=3} &= (N+1)^3 + \sum_{n=1}^{\lfloor N/2 \rfloor} \mathcal{P}_n \binom{N}{n}, \\ \mathcal{P}_n &= (1+N-2n)^2(2+2N-n)\frac{1+N+n}{1+N-n}\ . \end{aligned} \tag{3.34}$$

We define α via $n = N/2 - \alpha N$, so that the binomial is sharply peaked at α small. We take N large and α small, and use Stirling's formula to approximate it as

$$\binom{N}{\frac{N}{2} - \alpha N} = 2^N \sqrt{\frac{2}{N\pi}} e^{-2\alpha^2 N} \Big(1 + \mathcal{O}\big(\alpha^2, \alpha^4 N, N^{-1}\big)\Big).$$

This expression is exponentially small unless α is order $1/\sqrt{N}$ or smaller, justifying neglecting the other terms. We then can approximate

$$\mathcal{P}_n = 18\,\alpha^2 N^3 + \mathcal{O}\Big(\alpha N^2, \alpha^3 N^3\Big) \tag{3.35}$$

and replace the sum over n in (3.34) with an integral over $N d\alpha$, giving

$$D_{\mathcal{N}}\Big|_{M=3} \approx 2^N \cdot 18 N^3 \sqrt{\frac{2N}{\pi}} \int_0^{\frac{1}{2}} d\alpha\, \alpha^2\, e^{-2N\alpha^2}\ .$$

Since the integrand is sharply peaked around $\alpha = 0$, we can extend the upper limit of integration to ∞ and then do the Gaussian integral, yielding (3.33). The corrections are suppressed by $1/N$: the terms in (3.35) suppressed by only $1/\sqrt{N}$ cancel after doing the integral.

Another limit of Eq. (3.30) worth considering is the large M limit for fixed N. Since the rank of each projector P^i_j remains fixed at 1, and the total number of projectors is fixed at N^2, we expect the nullspace to dominate in the large M limit. This is indeed the case: we show in App. A.3 that the limiting form is the dimension of the total Hilbert space:

$$\lim_{M\to\infty} \frac{D_{\mathcal{N}}}{M^{2N}} = 1. \tag{3.36}$$

We note that this effect does not happen in the SY model with spins in the fundamental representation: the permutation operators $\mathbb{P}^{ij}$ split the Hilbert space of two spins into symmetric and antisymmetric subspaces, which have comparable dimensions in the large M limit.

3.2.4 Strong Fragmentation in Certain SU(M) Symmetry Sectors

We have demonstrated degeneracies in the spectrum of H_M going well beyond SU(M), as for $M > 2$ many different representations obey the nullspace condition (3.29). The number of each such representation is the product of multiplicities $m(\boldsymbol{\lambda})m(\boldsymbol{\gamma})$, and it grows exponentially with N. For example, the binomial in the SU(3) formula (3.34) arises from the multiplicities, not the degeneracies coming from a particular SU(3) representation.

However, we see no evidence for degeneracies and fragmentation outside the nullspace. Thus despite its being exponentially large, the nullspace for H_M still comprises a vanishing fraction of the full Hilbert space for M finite. Thus fragmentation occurs only in a set of measure zero of the full Hilbert space, and almost all states presumably obey ETH.

The SU(M) representations appearing in the nullspace defined by (3.29) are rather special. The reason is that all the projectors P^i_j must annihilate states in the nullspace, and when forming $\rho \in \lambda \otimes \overline{\gamma}$, no singlets can appear.

This property leads to an interesting feature of H_M. We show here that determining whether a given eigenstate is in the nullspace requires only knowing how it transforms under SU(M). Namely, any eigenstate of H_M in the SU(M) representation $\boldsymbol{\rho} = \boldsymbol{\lambda} + \overline{\boldsymbol{\gamma}}$ satisfying the conditions of (3.29) must be in the nullspace. Any eigenstates of H_M in any other representations are not in the nullspace. This furthermore implies that those SU(M) symmetry sectors which contain nullstates are entirely composed of nullstates, since states in a same symmetry sector must be in the same type of SU(M) irrep. Thus, though the impact of the exponentially degenerate nullspace is weak in the spectrum as a whole, it leads to strong Hilbert space fragmentation in certain symmetry sectors where it entirely freezes the dynamics.

To derive this result, we begin by noting that any eigenstate of H_M can be labeled non-uniquely by the triple λ, γ, ρ where $\lambda, \gamma \in P_{N,M}$ and $\rho \in \lambda \otimes \overline{\gamma}$, just as shown in (3.23) for H_{clean}. In general the eigenvalues depend on more data than just these representations, but eigenstates in the nullspace of H_M satisfy the more restrictive properties given in (3.29). We prove that the only way to have $\rho = \boldsymbol{\rho}$ for any such $\boldsymbol{\rho}$ is if the corresponding $\lambda = \boldsymbol{\lambda}$ and $\gamma = \boldsymbol{\gamma}$ as well.

Assume $\boldsymbol{\lambda}$ and $\boldsymbol{\gamma}$ satisfy Eq. (3.29), with $\boldsymbol{\rho} = \boldsymbol{\lambda} + \overline{\boldsymbol{\gamma}}$. Say $\boldsymbol{\rho}$ also occurs in the decomposition of some other $\lambda \otimes \overline{\gamma}$. In the decomposition, the boxes in the Young diagram for λ will be rearranged according to the tensor product rules into rows of length $n_1, \ldots, n_M$, with $\sum_{a=1}^{M} n_a = N$, as they are attached to the rows in the diagram of $\overline{\gamma}$ to construct $\boldsymbol{\rho}$. Row by row in the diagram of $\boldsymbol{\rho}$,

this yields the set of equations

$$\boldsymbol{\gamma}_1 - \boldsymbol{\gamma}_{M-a+1} + \boldsymbol{\lambda}_a + m = \gamma_1 - \gamma_{M-a+1} + n_a, \tag{3.37}$$

where the integer m accounts for the fact SU(M) irreps are equivalent up to a constant shift in the lengths of all rows. Summing the left- and right-hand sides of Eq. (3.37) yields $\boldsymbol{\gamma}_1 + m = \gamma_1$, giving

$$-\boldsymbol{\gamma}_{M-a+1} + \boldsymbol{\lambda}_a = -\gamma_{M-a+1} + n_a \tag{3.38}$$

for each $a = 1 \dots M$. Let k be the number of nonzero elements in $\boldsymbol{\lambda}$, and ℓ the number of nonzero elements in $\boldsymbol{\gamma}$, with $k + \ell \leq M$ by Eq. (3.29). Summing the first k equations in Eq. (3.38) then yields

$$N = \sum_{a=1}^{k} n_a - \sum_{a=1}^{k} \gamma_{M-a+1}. \tag{3.39}$$

Because the first sum here is at largest N and the second non-negative, we must have $\sum_{a=1}^{k} n_a = N$ and so $n_a = 0$ for $a \geq k+1$. Using this result in Eq. (3.38) yields $m = 0$, $\gamma = \boldsymbol{\gamma}$, and $n_a = \boldsymbol{\lambda}_a$ for all values of a.

The final step comes from noting that the tensor product rules do not allow boxes in a Young diagram to move upward from their original row. Hence the Young diagram of λ must have k rows or fewer, and the boxes in these rows can only be moved downward in the construction of the Young diagram of $\boldsymbol{\rho}$ to obtain $n_a = \boldsymbol{\lambda}_a$ for $a \leq k$. However, since $\overline{\gamma}_a = \overline{\boldsymbol{\gamma}}_a = \overline{\boldsymbol{\gamma}}_1$ for $a \leq k$, any such downward movement would not be consistent with the tensor product rules: boxes originally in the same row cannot end up in the same column after taking the tensor product. (The reason is that tensor indices are symmetrised in the rows of Young diagram, antisymmetrised in the columns.) Thus the only consistent possibility for $\rho = \boldsymbol{\lambda} + \overline{\boldsymbol{\gamma}} \in \lambda \otimes \overline{\gamma}$ satisfying (3.29) is to have both $\gamma = \boldsymbol{\gamma}$ and $\lambda = \boldsymbol{\lambda}$, as claimed.

3.2.5 SU(M)-Symmetric Perturbations

It is possible to add certain SU(M)-symmetric perturbations to H_M while maintaining Hilbert space fragmentation. The simplest such perturbation is the addition

of permutation operators $\mathbb{P}_{ij}$ linking some spins which share a same sublattice. For example, setting N to be even, we consider the perturbed Hamiltonian

$$H'_M = H_M + \sum_{i=1}^{N/2} c^i \mathbb{P}^{2i-1,2i} + \sum_{i=j}^{N/2} d_j \mathbb{P}_{2j-1,2j}, \tag{3.40}$$

where the c^i and d_j are arbitrary distinct real coefficients, and upper and lower indices denote different spin sublattices as before. The permutation operators introduced in H'_M split the original nullspace of H_M into degenerate subspaces, the eigenvalues of which depend on how the interacting spins on each sublattice are divided into symmetrised and antisymmetrised pairs. It is apparent that projectors onto the resulting eigenstates form part of the commutant algebra. It is also simple to show that many of these subspaces grow exponentially in dimension with N. For example, the dimension of the subspace where each interacting pair of spins on a same sublattice is symmetrised can be lower bounded by

$$\sum_{\substack{k,\ell=1 \\ k+\ell\leq M}}^{M-1} \sum_{\boldsymbol{\lambda}\in P_{N/2,k}} \sum_{\boldsymbol{\gamma}\in P_{N/2,\ell}} m(\boldsymbol{\lambda}) m(\boldsymbol{\gamma}) d(2\boldsymbol{\lambda} + 2\overline{\boldsymbol{\gamma}}),$$

where $2\boldsymbol{\lambda}$ refers to the irrep obtained by gluing two copies of $\boldsymbol{\lambda}$ together horizontally. Hence the perturbed model H'_M is also Hilbert-space-fragmented.

It is also possible to maintain fragmentation while adding in SU(M)-symmetric interactions involving multiple spins on a same sublattice. In this scenario, a sufficient condition for fragmentation is that it must be possible to divide at least one of the two sublattices of the perturbed Hamiltonian into a linear-in-N number of further sublattices, such that none of the newly-formed sublattices are directly linked by a term in the Hamiltonian. In this case, one can again show the presence of fragmentation by considering the subspace in which all spins in each of the newly-formed sublattices are symmetrised amongst themselves. One can then demonstrate that the number of ways of constructing suitable irreps satisfying these symmetrisation constraints and with the same eigenvalue still grows exponentially. On the other hand, we have numerically verified at small N that adding all-to-all permutation interactions on both of the sublattices removes any exponentially growing degeneracies, and hence also removes Hilbert space fragmentation.

3.2.6 Spins in Antisymmetric Representations

A natural generalisation of H_M is to take spins in representations other than the fundamental ones. We utilise the antisymmetric representation $\mathbf{A}_m$ of SU(M), which has a Young diagram with one column and m rows. We consider N spins in the $\mathbf{A}_m$ representation and $\widetilde{N}$ in the $\overline{\mathbf{A}}_m = \mathbf{A}_{M-m}$ representation. The Hamiltonian we obtain is the obvious generalisation of (3.5), namely

$$H_{M,m} = \frac{1}{\sqrt{MN}} \sum_{i=1}^{N} \sum_{j=1}^{\tilde{N}} g_j^i P_j^i \tag{3.41}$$

where the projectors are as in (3.3) with the sum running instead to $d_m = \binom{M}{m}$, the number of states per site. We have included random couplings g_j^i and allow for $N \neq \tilde{N}$.

The generalised Hamiltonian $H_{M,m}$ remains a sum of positive semidefinite operators, so the nullspace still consists of those states annihilated by each two-site term individually. The calculation of the nullspace dimension thus proceeds similarly to Sec. 3.2. The clean model Hamiltonian is written in terms of Casimirs as

$$H_{M,m}^{\text{clean}} = \frac{m^2\left(N^2+\tilde{N}^2\right)}{2M} + \frac{1}{2}\left(C_{\mathbf{A}_m^{\otimes N}} + C_{\overline{\mathbf{A}}_m^{\otimes \tilde{N}}} - C_{\mathbf{A}_m^{\otimes N} \otimes \overline{\mathbf{A}}_m^{\otimes \tilde{N}}}\right)$$

just like (3.23). The tensor products can be decomposed into irreducible representations $\lambda \in \mathbf{A}_m^{\otimes N}$, $\overline{\gamma} \in \overline{\mathbf{A}}_m^{\otimes \tilde{N}}$ and $\rho \in \gamma \otimes \lambda$. One then finds as in (3.29) that the ground states are states where $\rho = \lambda + \overline{\gamma}$ and $k + l \leq M$, with Young diagrams for λ and γ having k and l rows respectively.

For $m \neq M/2$, similar arguments to those for $m = 1$ show that the dimension of the nullspace grows exponentially with N, and hence that $H_{M,m}$ is Hilbert-space-fragmented. We prove this result explicitly in Appendix A.4. For $m = M/2$, the model is equivalent to the SY model with spins in the representation $A_{M/2}$. We thus expect no Hilbert space fragmentation. Indeed, all but one of the possible λ have more than $M/2$ rows, and likewise for γ. Hence there is only one SU(M) representation in the nullspace, the one with a rectangular Young diagram with $m = M/2$ rows and $N + \tilde{N}$ columns. It has multiplicity one in the tensor products, so fragmentation does not occur.

3.3 The Read-Saleur Symmetry Algebra and its Remnant

A remarkable feature of the nearest-neighbour chain H_{nn} (3.7) is the presence of a large commutant algebra discovered by Read and Saleur [78]. The resulting degeneracies occur throughout almost all the spectrum. Their number grows exponentially with system size, resulting in Hilbert space fragmentation [34]. We have shown that the exponentially large dimension of the nullspace and the ensuing fragmentation survive the introduction of the many additional couplings in H_M. As described in section 3.1.2, this behaviour automatically results in a commutant algebra acting within this nullspace. In this section we demonstrate that this algebra is a subalgebra of the RS algebra.

3.3.1 The Read-Saleur Algebra

Here we describe the Read-Saleur (RS) commutant algebra of the nearest-neighbour chain (3.7). To make the structure more apparent, we renumber the sites as $p = 1, \ldots, 2N$, with odd p labeling spins in the $\mathbf{M}$ representation and even p labeling those in the $\overline{\mathbf{M}}$. We also relabel the generators of $H_{\rm nn}$ as $e_{2i-1} \equiv P^i_i$ and $e_{2i} \equiv P^i_{i+1}$ so

$$H_{\rm nn} = \sum_{p=1}^{2N-1} r_p e_p, \quad e_p = \sum_{a,b=1}^{M} |a_p a_{p+1}\rangle\langle b_p b_{p+1}| \ . \tag{3.42}$$

with r_p the non-vanishing random couplings. Each projector e_p onto a nearest-neighbour SU(M) singlet has only one non-vanishing eigenvalue out of the M^2 possibilities. Since the nearest-neighbour chain has only $2N$ such projectors, one expects large degeneracies for large enough M.

The generators e_p satisfy the Temperley-Lieb algebra [80]:

$$\Big(e_p\Big)^2 = M e_p \ , \qquad e_p e_{p\pm1} e_p = e_p \tag{3.43}$$

and $e_p e_{p'} = e_{p'} e_p$ with $|p - p'| > 1$. Many interesting lattice Hamiltonians are written in terms of the e_p, such as the spin-1 biquadratic chain [80]. Read and Saleur [78] showed how the degeneracies in H_{nn} are independent of the couplings r_p. They did so by constructing the irreducible representations of the Temperley-Lieb

algebra in this chain. The resulting degeneracies are completely independent of the couplings, following solely from understanding how the Temperley-Lieb algebra works here. Not surprisingly, the nullspace has the largest degeneracy, but large degeneracies are found for all but a small set of states.

A key tool of Read and Saleur's results is the construction of the commutant algebra $\mathcal{C}^{\mathrm{RS}}$ of the e_p. It is generated by $\mathbf{J}^{(s)}$ that satisfy

$$e_p \mathbf{J}^{(s)} = \mathbf{J}^{(s)} e_p = 0 \tag{3.44}$$

for all p. Read and Saleur find a linear basis set for the generators in terms of the same building blocks (3.1) used to construct the SU(M) generators, namely

$$J^a_{b,2i-1} = T^{a,i}_b, \qquad J^a_{b,2j} = S^a_{b,j}. \tag{3.45}$$

Generators of $\mathcal{C}^{\mathrm{RS}}$ are of the form

$$\begin{aligned} \mathbf{J}^{(s)} &= \sum_{a_1,b_1,\ldots} \widetilde{g}^{b_1 b_2 \ldots b_s}_{a_1 a_2 \ldots a_s} \mathbf{J}^{a_1 a_2 \ldots a_s}_{b_1 b_2 \ldots b_s}, \\ \mathbf{J}^{a_1 a_2 \ldots a_s}_{b_1 b_2 \ldots b_s} &\equiv \sum_{1 \le p_1 < p_2 < \ldots < p_s \le 2N} J^{a_1}_{b_1,p_1} J^{a_2}_{b_2,p_2} \cdots J^{a_s}_{b_s,p_s} \end{aligned} \tag{3.46}$$

for $0 \le s \le 2N$. Setting $s=1$ yields the SU(M) generators. For (3.44) to be satisfied, the necessary and sufficient conditions on the coefficients are

$$\sum_{\hat{a}=1}^{M} \widetilde{g}^{\ldots,\hat{a},b_{p+1}\ldots}_{\ldots a_p,\hat{a},\ldots} = \sum_{\hat{a}=1}^{M} \widetilde{g}^{\ldots,b_p,\hat{a},\ldots}_{\ldots,\hat{a},a_{p+1},\ldots} = 0 \tag{3.47}$$

for all p. More explicit expressions for the $\mathbf{J}^{(s)}$ can be found in Ref. [78].

As apparent from (3.46), the RS algebra includes the universal enveloping algebra $\mathfrak{U}(\mathrm{SU}(M))$ (i.e. products of the SU(M) generators in this representation). It is straightforward to check that the $J^{(s)}$ map between different representations of SU(M), and so go beyond $\mathfrak{U}(\mathrm{SU}(M))$.

3.3.2 The Commutant Algebra of H_M

We have shown explicitly in Sec. 3.2.3 that degeneracies in the nullspace survive the inclusion of all N^2 couplings in H_M, and that one can define elements of the commutant algebra mapping between them. We show here that these elements form a subalgebra of the RS algebra, in particular of the algebra generated by the $\mathbf{J}^{(2N)}$.

In the nearest-neighbour case, the $\mathbf{J}^{(2N)}$ act non-trivially on the nullspace of H_{nn} and annihilate all other states. The reason is that the $\mathbf{J}^{(2N)}$ annihilate any state with at least one nearest-neighbour SU(M) singlet, and the eigenstates of H_{nn} with non-zero eigenvalues are solely composed of such states [78]. Furthermore, for any two states in the nullspace of H_{nn}, there is an operator amongst the $\mathbf{J}^{(2N)}$ that maps between them.

We generalise this result here. Since all nullstates of H_M are also nullstates of H_{nn}, maps between the former are given by operators $\mathbf{J}^{(2N)}$ that satisfy certain additional constraints. For notational ease, we relabel the indices as

$$\mathbf{J}^{(2N)} = \sum g^{b^1\cdots b^N d_1\cdots d_N}_{a^1\cdots a^N c_1\cdots c_N} T^{a_1,1}_{b_1}\cdots T^{a^N,N}_{b^N} S^{c_1}_{d_1,1}\cdots S^{c_N}_{d_N,N}. \tag{3.48}$$

where this sum and all those in this section are over the appropriate a^i, b^i, c_j, d_j from 1 to M. To be in the commutant algebra of H_M, these operators obey

$$\mathbf{J}^{(2N)} P^i_j = P^i_j \mathbf{J}^{(2N)} = 0, \quad \text{for } 1 \le i,j \le N. \tag{3.49}$$

These constraints require that the coefficients satisfy

$$\sum_{\{b\},\{c\}} \delta^{c_i}_{b^j}\, g^{\cdots b^j \cdots\cdots}_{\cdots\cdots c_i\cdots} = \sum_{\{a\},\{d\}} \delta^{a^i}_{d_j}\, g^{\cdots\cdots d_j\cdots}_{\cdots a^i\cdots\cdots} = 0 \tag{3.50}$$

for all $1 \le i,j \le N$.

A general nullstate of H_M is given by

$$|\psi\rangle = \sum_{\{a\},\{d\}} \psi^{d_1\cdots d_N}_{a^1\cdots a^N} \left| a^1\cdots a^N d_1\cdots d_N \right\rangle, \tag{3.51}$$

where the a^i and d_j transform in the $\mathbf{M}$ and $\overline{\mathbf{M}}$ representations respectively, and the coefficients satisfy

$$\sum_{\{a\},\{d\}} \delta^{a^i}_{d_j} \psi^{d_1\cdots d_N}_{a^1\cdots a^N} = 0, \text{ for } 1 \le i,j \le N. \tag{3.52}$$

The resemblance to the constraints on $\mathbf{J}$ is not coincidental. We can find a solution to (3.50) by taking any two solutions ψ, χ of (3.52) and defining

$$g^{b^1\cdots b^N d_1\cdots d_N}_{a^1\cdots a^N c_1\cdots c_N} = \psi^{d_1 d_2\cdots d_N}_{a^1 a^2\cdots a^N} \left(\chi^{c_1\cdots c_N}_{b^1\cdots b^N}\right)^*. \tag{3.53}$$

We thus have proved that $|\psi\rangle\langle\chi|$ can be written as an operator $\mathbf{J}^{(2N)}$ from Eq.(3.46).

Regarding the other energy levels of H_M, our numerics found no sign of degeneracies other than those arising from the global SU(M) symmetry. This suggests that the only operators $\mathbf{J}^{(s)}$ which act nontrivially on eigenstates outside the nullspace are elements of $\mathfrak{U}(\mathrm{SU}(M))$. This suggestion is consistent with Read and Saleur's derivation of the symmetry generators for the nearest-neighbour chain [78]. Their construction utilises a "dimer" basis for the Hilbert space, where each state is written as a product of spin-singlet (dimer) states. Operators in the Temperley-Lieb algebra act non-trivially on the dimers, whereas those in the RS algebra leave the dimers untouched. The non-local projectors P^i_j in H_M, however, mix the dimer states in a much more complicated way, and so there is no reason to expect degeneracies beyond SU(M). Indeed, from this point of view it is rather surprising that even a non-trivial nullspace survives.

3.4 Scars from the Shiraishi-Mori Construction

We have established that each eigenstate in the nullspace of H_M does not mix with the others under time evolution. As such, it is tempting to label these eigenstates as quantum many-body scars [6, 12–15]. The numerous product eigenstates identified in Sec. 3.1.2 have area-law entanglement entropy scaling, a signal of a scar. However, as we discussed in Section 2.4, typically a scar is a rare ETH-violating exception in an otherwise thermal spectrum. Here the situation is rather different, as states in certain SU(M) representations are in the nullspace, while all others are not.

We show in this section how to perturb H_M to yield more conventional scars. We utilise the Shiraishi-Mori (SM) embedding formalism [24] to break the SU(M) symmetry, converting some of the original nullspace eigenstates into quantum many-body scars. To do so, we must address subtleties involved in applying this formalism to non-local models.

Assume we have split our Hilbert space into SU(M)-quantum-number sectors $\mathcal{H}_n$, where n is an index labeling the different sectors. Defining $\mathcal{K}_{n,\max}$ to be the largest Krylov subspace of $\mathcal{H}_n$, it was argued in [30] that two conditions

are sufficient for an eigenstate $|\psi_{\text{scar}}\rangle$ of a local Hamiltonian to be a quantum many-body scar. These conditions are

$$|\psi_{\text{scar}}\rangle\langle\psi_{\text{scar}}| \in \mathcal{C} \ , \qquad \frac{\dim(\mathcal{K}_{n,\max})}{\dim(\mathcal{H}_n)} \xrightarrow{N\to\infty} 1, \tag{3.54}$$

where $\mathcal{C}$ is a non-trivial commutant algebra. As we discussed in Section 2.4, the first condition ensures that the scar state violates ETH by implying that the scar state is an eigenstate of a family of Hamiltonians. Indeed, ETH-obeying eigenstates of local models generically have a unique parent Hamiltonian [30, 86, 87]. The second condition ensures that most eigenstates in the SU(M) quantum number sector in question are part of a dominant subspace and hence thermal, with the scar state constituting a rare exception. We therefore see that the nullstates of H_M are not scars as they violate the second condition of Eq. (3.54). Indeed, as we showed in Section 3.2.4, the quantum number sectors containing nullstates are entirely composed of 1D Krylov subspaces, so the ratio in Eq. (3.54) must vanish.

To make the nullstates of H_M scars, following Refs. [24, 30], we perturb H_M as

$$H_{\text{SM}} = \sum_{i,j=1}^{N} P_j^i h_{[j]}^{[i]} P_j^i + H_{\text{pert}}, \tag{3.55}$$

where the $h_{[j]}^{[i]}$ are finite-support operators that are sufficiently general to break the SU(M) symmetry, and H_{pert} is chosen to split the degeneracies between the nullspace eigenstates. Each operator $h_{[j]}^{[i]}$ need not have support on the spins i and j, so these indices merely serve as labels. The original Hamiltonian H_M from Eq. (3.5) corresponds to setting $h_{[j]}^{[i]} = r_j^i \mathbb{1}$ and $H_{\text{pert}} = 0$.

Because the SU(M) symmetry of H_M is broken, the perturbed Hamiltonian H_{SM} acquires a dominant thermal subspace, and hence satisfies the second condition of Eq. (3.54). Furthermore, when $H_{\text{pert}} = 0$, the nullspaces of H_{SM} and H_M are the same, and so states in the nullspace satisfy the first condition of Eq. (3.54) as well. However, satisfying these conditions does not automatically guarantee that states in the nullspace of a non-local model are quantum many-body scars. This is because a thermal eigenstate is generally understood to uniquely specify a parent Hamiltonian only for spatially local systems [86, 87]. In the absence of

locality, we thus cannot conclude that the first condition is sufficient to imply that an eigenstate violates ETH.

However, the product eigenstates in the nullspace identified in Sec. 3.1.2 have area-law scaling and so violate ETH. Moreover, we can choose H_{pert} such that the product eigenstates of H_M are split from the remainder of the nullspace. Namely, we perturb by the diagonal on-site U(M) generators defined in Eq. (3.1) via

$$H_{\text{pert}} = \sum_{\alpha=1}^{M} \left(\sum_{i=1}^{N} c^{\alpha,i} T_{\alpha}^{\alpha,i} + \sum_{j=1}^{N} d_j^{\alpha} S_{\alpha,j}^{\alpha} \right), \tag{3.56}$$

where the $c^{\alpha,i}$ and d_j^{α} are arbitrary distinct real coefficients. The product states from $\mathcal{N}$ remain eigenstates of H_{SM}, and now are situated in quantum-number sectors of H_{SM} that have a dominant thermal Krylov subspace. They thus satisfy the conditions in Eq. (3.54), and furthermore violate ETH due to their area-law entanglement entropy scaling. The product states hence constitute quantum many-body scars of H_{SM}. In particular, when the coefficients $c^{\alpha,i}$ and d_j^{α} are rational, any initial state composed of a sum of these product states would exhibit revivals when time-evolved with H_{SM}, a hallmark of scars [14]. Additionally, since the number of such product states grows exponentially with N, the perturbed model H_{SM} has an exponentially growing number of quantum many-body scars and is Hilbert-space-fragmented.

3.5 Concluding Remarks

The non-local model introduced in this chapter possesses a number of remarkable properties. In spite of its long-range interactions, the dimension of its nullspace grows exponentially with increasing system size. Furthermore, maps between eigenstates in the nullspace are elements of the commutant algebra. The exponentially growing degeneracy thus leads to strong Hilbert space fragmentation in some of the SU(M) quantum number sectors of the spectrum. The commutant algebra itself is a non-trivial subalgebra of the Read-Saleur algebra of Temperley-Lieb chains. The Shiraishi-Mori embedding formalism can be utilised to perturb many of the eigenstates in the nullspace into quantum many-body scars.

Non-local models with Hilbert space fragmentation are rarer in the literature than those with quantum many-body scars. Non-local models have a large bond algebra: for example, the number of generators of the bond algebra of H_M grows quadratically with N, as opposed to the linear growth associated with a 1D spin chain. This strongly constrains the dimension of the commutant algebra, making fragmentation less likely.

Previous works have considered how scars and fragmentation can be stable against the addition of longer-range interactions to local Hamiltonians [28, 54, 76, 77, 101–104]. However, the model studied here is apparently an unusual example of one where the non-local terms are the leading contribution to the problem, and cannot be ascribed a notion of spatial distance: it is intrinsically "zero dimensional". It would be interesting to explore at a future point other problems of this nature which share some features of our model, for instance the model of Ref. [105] which is also SYK-like and has extensive degeneracies in its eigenspectrum.

4

Universal Freezing Transitions of Dipole-Conserving Chains

In the study of ergodicity in quantum systems, a particular point of interest is how systems can undergo phase transitions between ergodicity-breaking and ergodicity-restoring phases. One class of models in which this has been studied is many-body localised models [5, 9, 10], where an ergodicity-breaking phase is conjectured to emerge as the result of quenched disorder. However, such models have proven to be challenging to study analytically. Following the recent discovery of fractons [36–40], a promising alternative route to studying such transitions is to look at systems with local range-k interactions that exhibit Hilbert space fragmentation in the presence of dipole conservation [31–33]. Such systems can arise in the quantum Hall effect [43, 106, 107] and in systems of charged particles exposed to a strong electric field [75, 108–111]. In these systems, the conservation of a charge N and its dipole moment X combined with strict locality of interactions greatly inhibit dynamical evolution. Isolated charges in these models cannot propagate on their own, as they require other nearby charges to interact with so as to ensure the conservation laws are respected. Hence, states in the same (N, X) quantum number sector can be dynamically disconnected, leading to Hilbert space fragmentation.

Dipole-conserving chains with local range-k interactions can undergo a continuous transition from a strongly Hilbert-space-fragmented phase (where ergodicity is broken) to a weakly Hilbert-space-fragmented phase (where ergodicity is mostly

restored) when the charge density $\nu \equiv N/L$ (where L is the chain length) is increased past a critical density ν_c [2, 41, 42, 112]. In the strongly fragmented phase, almost all states belong to strongly fragmented (N, X) symmetry sectors, whereas in the weakly fragmented phase, almost all states belong to weakly fragmented (N, X) sectors. In [41], where this phase transition was first discussed, it was proposed that the strongly fragmented phase could be characterised by the presence of a finite density of "frozen sites" in a typical state, where a frozen site is a site whose onsite value of the global conserved charge remains the same under dynamical evolution up to infinitely late times. The mean density of frozen sites thus serves as an order parameter for the strongly fragmented phase. These frozen sites have the effect of spatially dividing typical states into finite-sized dynamically disconnected "active bubbles" in the strongly fragmented phase. In the weakly fragmented phase, the density of frozen sites vanishes and transport can occur. The study of this phase transition opens up new possibilities for a rigorous characterisation of ergodicity-breaking transitions in quantum many-body systems, as the underlying mechanisms of the transition rely only on symmetries and locality, which are easier to work with compared to the quenched disorder in the MBL case.

In this chapter, which is based on [2], we present a number of analytic and numerical results that significantly advance our understanding of this phase transition in locally interacting dipole-conserving chains. We argue that these chains transition from a strongly fragmented phase to a weakly fragmented phase at a critical charge density of $\nu_c = (k-2)^{-1}$, where k is the range of interactions. The density ν_c is thus universal in that it is independent of the details of the dynamics as well as of the onsite Hilbert space dimension d. This leads to the d-independent phase diagram of Fig. 4.1. In arguing for this result, we develop several new concepts and approaches for characterising strongly and weakly fragmented phases and the transition between them.

Quantum chains with charge-dipole symmetry, onsite Hilbert space dimension d, and range-k interactions can be analysed by reformulating them as problems of hopping particles on a 1D lattice with maximal onsite occupation $d-1$ and

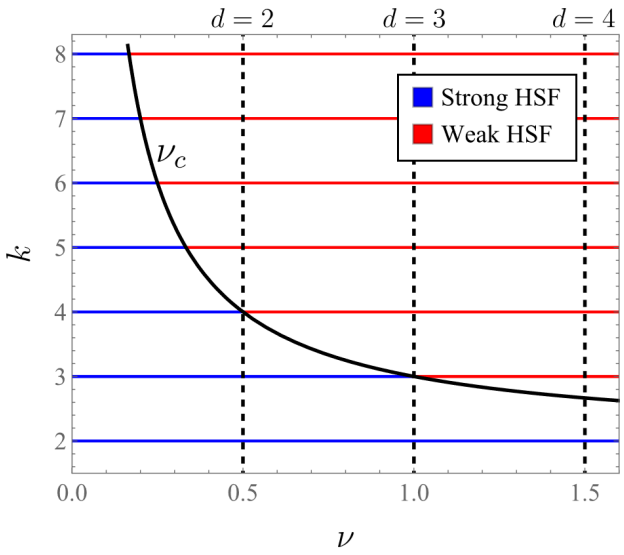

Figure 4.1: The conjectured universal phase diagram of charge- and dipole-conserving quantum chains with local range-k interactions. The relevant variables are the continuous particle filling $\nu \geq 0$ and the local range of interactions k, and the diagram is "discrete" in the sense that only integer values of k can be considered. A first phase transition from strong to weak fragmentation occurs at $\nu_c = 1/(k-2)$, a value independent of the onsite Hilbert space dimension d. We note that for each value of d, the above figure only depicts the phase diagram for $\nu < (d-1)/2$, i.e. half-filling (depicted by the dashed vertical lines). Beyond half-filling, the phase diagram is mirrored by particle-hole symmetry, with a second (not-depicted) weak-to-strong transition at $d - 1 - \nu_c$. For $k = 2$ and any d (as well as $k = 3$ and $d = 2$), no hopping moves which respect the global conservation laws are possible, leading to trivial strong fragmentation for all ν. We refer to such models as deeply frozen and discuss them further in Chapter 5.

with range-k hopping moves that conserve both total particle number N and centre of mass X/N [41, 42]. For example, a spin-S chain can be reformulated as a hopping-particle model with $d = 2S + 1$. Such hopping models will therefore be the focus of our analysis. We introduce the concept of "blockages" to characterise the strongly fragmented phase at $\nu < \nu_c$. For a given Krylov subspace, we define blockages as regions of the system across which transport of particle number and dipole moment (i.e. center of mass) quanta cannot occur within the subspace. Blockages constitute a generalisation of the "bottlenecks" introduced in Ref. [33]. The simplest example of a blockage is a contiguous sequence of $k-1$ or more frozen sites. Indeed, such a sequence necessarily dynamically disconnects the regions to its left and right from each other. On the other hand, there are also blockages

that do not involve any frozen sites at all.

Another crucial ingredient in our study of the strongly fragmented phase is that of a "fully extended state" (FES), introduced in Ref. [42] and whose scope we expand substantially. An FES consists of a configuration of particles in a $d = \infty$ system in which the particles are as spread out as the local range of interactions k will allow. We prove, for general interaction ranges k, that there exists a unique FES within each Krylov subspace of a $d = \infty$ system, and furthermore that the structure of a given FES can be used to determine the spatial locations of blockages within states in that Krylov subspace. Importantly, we shall show that blockages can be located using FESs for states in finite-d systems as well. This is done by embedding states in finite-d chains into "auxiliary" $d = \infty$ chains and mapping them to their corresponding FES, from which the location of some blockages in the finite-d system can be determined. We shall refer to this approach as the "FES picture".

Using the FES picture, we analytically demonstrate that, for particle fillings $\nu < \nu_c$ and for $d = 2$ and $d = \infty$, a given random configuration of particles will almost always feature a finite density of frozen sites forming blockages, and that this implies that almost all states at each such filling ν belong to symmetry sectors that are strongly fragmented. We also use the FES picture to obtain numerical evidence at large system sizes that this is the case for $\nu < \nu_c$ for other (less analytically tractable) values of d as well. We furthermore use the FES picture to analytically lower bound the average densities of different kinds of "active bubbles", which are local groups of interacting particles shielded from their surroundings by blockages made of frozen sites.

To identify the weakly fragmented phase, we numerically show that for $\nu > \nu_c$ and arbitrary d, almost all configurations of particles at a given ν belong to weakly fragmented (N, X) sectors. The dominant Krylov subspaces of these sectors do not have blockages, and can be characterised by the fact that they contain a particular state which we call a "blockage-free extended state" (BES). We show that there is a unique BES in each (N, X) sector, and numerically demonstrate that for $\nu > \nu_c$, random particle configurations almost always belong to the Krylov

subspaces which contain BESs, indicating that these subspaces are dominant in their (N, X) sectors. We will also see that for any value of d, the filling ν_c is the smallest filling at which it is possible to construct blockage-free Krylov subspaces. This is why the critical filling is d-independent.

Our FES picture can be used to analytically characterise the degree of fragmentation not just of individual (N, X) symmetry sectors, but of whole families of symmetry sectors at arbitrary onsite dimensions d, while also providing several insights concerning the dynamical impacts of strong fragmentation on the model. Furthermore, the numerical algorithms we develop are not only efficient at large system sizes but also exactly simulate the dynamics of the systems, in contrast to the approximate numerical methods developed in [41].

The remainder of the chapter is organised as follows. In Section 4.1, we begin by introducing our family of models and reviewing various probes that can be used to distinguish between the strongly and weakly fragmented phases. In Section 4.2, we introduce the concepts of fully extended states (FESs) and blockages, and derive several results concerning these concepts. In Section 4.3, we employ these concepts to develop the FES picture, which we use to derive several analytic and numerical results concerning the strongly fragmented phase. In Section 4.4, we present numerical evidence that, for $\nu > \nu_c$ and arbitrary d, the dominant symmetry sectors to which most states belong possess a dominant Krylov subspace and hence are weakly fragmented. We provide concluding remarks in Section 4.5.

4.1 Fragmentation in Dipole-Conserving Chains

In Section 2.3.2, we gave a preliminary introduction to fragmentation in locally interacting dipole-conserving systems as a basic example of Hilbert space fragmentation. We also refer the reader to the seminal papers [31–33] on the matter. We now introduce the range-k dipole-conserving hopping-particle model which is the focus of this chapter. It is important to note, however, that the Krylov subspace decompositions we compute for this model are also generally applicable to any 1D lattice system with local range-k interactions conserving a global charge and its

dipole moment. Hence, almost all of the results we derive in this chapter (and in particular the universal nature of the critical density) also hold in general for 1D range-k dipole-conserving quantum chains.

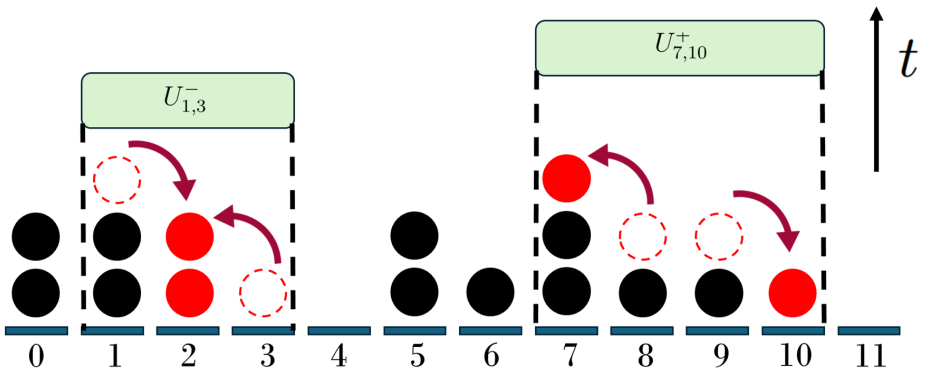

Figure 4.2: An example with $k = 4$ and $d = 4$ of the classical Markovian circuit dynamics considered in this chapter. The particles in a state are acted on by a series of hopping gates randomly chosen from the set $\{U^{\pm}_{i,j}\}$, where operators $U^{+}_{i,j}$ denote an outward hop (where particles on sites $i+1$ and $j-1$ both hop one site away from each other) and operators $U^{-}_{i,j}$ denote an opposite inward hop. Hence, the site index i ranges from 0 to $L-3$ and the site index j ranges from $i+2$ to $i+k-1$. A hopping gate is only applied if the final state to which it leads is consistent with the onsite dimension d and chain length L.

Here we study a system of N indistinguishable "bosonic" particles on a 1D lattice composed of L sites with open boundaries. Each site on the lattice can hold at most $d-1$ particles, where $d \in \{2, 3, \ldots, \infty\}$ denotes the onsite Hilbert space dimension. The particles are acted on by a random sequence of range-k (with k finite) hopping gates which conserve total particle number $N = \sum_i n_i$ and dipole moment $X = \sum_i i n_i$, where n_i counts the number of particles on each site. We define the corresponding intensive quantities to be the particle filling $\nu = N/L$ and the intensive centre of mass $\nu_X = X/NL$.

Since the Hilbert space fragmentation in this model is classical, we may restrict ourselves when determining its Krylov subspace decomposition to considering how the model acts on product states, where each n_i has a definite value, and we may set our hopping gates to be "classical" in that they map one such product state to another. In fact, it is sufficient to consider a classical Markov circuit with local

range-k gates that act on pairs of particles, making them both hop one site towards or away from each other. We refer to these as inward and outward hops respectively. We depict these dynamics explicitly in Fig. 4.2.

Due to the classical nature of our analysis, we will generally refer to product states corresponding to specific configurations of particles simply as "states", and use the terms "quantum state" and "eigenstate" when we are referring to more general vectors on the Hilbert space. We also restrict our attention to fillings $0 \leq \nu \leq (d-1)/2$. This is because by particle-hole symmetry, we obtain identical physics under the transformation $\nu \to d-1-\nu$ (including a weak-to-strong transition at $\nu = d-1-\nu_c$), and so all of our conclusions apply equally well there.

4.1.1 Characterising the Strongly and Weakly Fragmented Phases

For a given symmetry sector with quantum numbers (N, X) of a system with size L and onsite Hilbert space dimension d, let $D^{(d)}(N, X, L)$ denote the dimension of the symmetry sector, and let $D^{(d,k)}_{\max}(N, X, L)$ denote the size of the largest Krylov subspace within it for a model with local range-k interactions. We fix $N = \nu L$ and $X = \nu\nu_X L^2$ such that they scale with L (this also defines ν_X, the intensive dipole moment). The distinction between strong and weak fragmentation in the (N, X) sector can then be defined using the ratio

$$r_{d,k}(N, X, L) = \frac{D^{(d,k)}_{\max}(N, X, L)}{D^{(d)}(N, X, L)} \,, \tag{4.1}$$

$$\lim_{L\to\infty} r_{d,k}(N, X, L) = \begin{cases} 0 & \text{strong fragmentation} \\ 1 & \text{weak fragmentation} \end{cases} \,, \tag{4.2}$$

For a fixed value of ν, we define the model to be in its strongly fragmented phase if in the thermodynamic limit a randomly drawn configuration of $N = \nu L$ particles almost always belongs to a strongly fragmented (N, X) sector. Likewise, we define the model to be in its weakly fragmented phase if a randomly drawn state of $N = \nu L$ particles almost always belongs to a weakly fragmented (N, X) sector. We can

diagnose if the model is in its weakly or strongly fragmented phase using the function

$$R_{d,k}(N,L) = \frac{\sum_X D^{(d,k)}_{\max}(N,X,L)}{D^{(d)}(N,L)} \ , \tag{4.3}$$

$$\lim_{L\to\infty} R_{d,k}(N,L) = \begin{cases} 0 & \text{strongly fragmented phase} \\ 1 & \text{weakly fragmented phase} \end{cases} \ , \tag{4.4}$$

where the sum in the numerator is over all centres of mass X compatible with N and L, and $D^{(d)}(N,L) \equiv \sum_X D^{(d)}(N,X,L)$ is the dimension of the N sector, i.e. the subspace spanned by all possible states with N particles. Note that Eqs. (4.1) and (4.3) thus differ by the sum over all possible dipole moments X in Eq. (4.3), as opposed to (4.1) which considers only a particular value of X.

An alternate approach to characterising the two phases was proposed in [41], where it was suggested that the mean density of "frozen sites" in states at a given ν could be used as an order parameter. A frozen site in a given state is a site whose particle occupation number cannot change under dynamical evolution. In other words, for all states in the Krylov subspace to which the state belongs, the frozen site has the same particle occupation number. We note that this implies that all states in a given Krylov subspace have the same density of frozen sites. Thus, let $\rho_F(i)$ denote the density of frozen sites in the i-th Krylov sector $\mathcal{K}_i^{(d,k)}$ of a given N sector for some indexing $i = 1, \ldots, K_{d,k}(N)$. We may then define the mean density of frozen sites to be given by

$$\overline{\rho}_F^{(d)}(k,N,L) = \frac{\sum_{i=1}^{K_{d,k}(N)} \rho_F(i)\ \dim(\mathcal{K}_i^{(d,k)})}{D^{(d)}(N,L)} \tag{4.5}$$

The authors of [41] argued based on numerical results that the strongly fragmented phase could be characterised by the presence of a finite mean density of frozen sites in states with $\nu < \nu_c$, which would prevent ergodicity. In Section 4.3.3, we add analytic credence to these claims by proving for $d = 2$ and $d = \infty$ that $\overline{\rho}_F^{(d)}(k,N,L)$ has a finite value in the thermodynamic limit for $\nu < \nu_c$, and that this implies the model is in its strongly fragmented phase. We also provide numerical evidence that this is the case for other values of d as well. In Section 4.4, we numerically show that the density of frozen sites vanishes in the weakly fragmented phase, and

hence that this is a valid order parameter. These results are significant because, as we discuss in Section 4.3.1, a finite density of frozen sites is not a necessary condition for strong fragmentation: there exist Krylov subspaces which contain no frozen sites and yet still form a vanishing part of their symmetry sectors. Our results show that such Krylov subspaces constitute a measure-0 fraction of the spectrum, and hence that typical randomly drawn states feature a finite density of frozen sites in the strongly fragmented phase.

4.2 Characterising Krylov Subspaces via Fully Extended States

We turn our attention to systems with $d = \infty$, which do not have an upper bound on the number of particles that can be stacked on a given site. For a $d = \infty$ system, we define a "fully extended state" (FES) (as introduced in [42]) to be a configuration of particles in which no pair of particles can perform an outward hop with each other. It is clear that this implies that all particles in the bulk of the system must be separated by at least $k - 3$ holes from their neighbours (where k is, as before, the finite range of interactions) and cannot be stacked. If this was not the case, it would still be possible for some pairs of particles to perform outward hops. For systems with open boundary conditions, the only exceptions to these rules are at the boundaries: an indefinite number of particles can be stacked on the leftmost and rightmost sites of the system, and there is no lower bound on the number of holes separating each of these boundary stacks from the next closest particle. An example of an FES with $k = 6, N = 10, X = 130$ (with the leftmost site being site 0) is

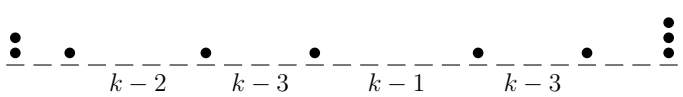

In this section, we show how FESs can be used to characterise the different Krylov subspaces of a $d = \infty$ system. In Section 4.2.1, we show that each Krylov subspace contains exactly one FES, which is unique to that subspace. In Section 4.2.2, we then show that the structure of the FES determines whether a Krylov subspace

contains any blockages, and where those blockages are spatially located within the states in the subspace. In Section 4.2.3, we discuss the structure of blockage-free FESs (BFESs), which can be used to identify Krylov subspaces without blockages and are important to our discussion of the weakly fragmented phase in Section 4.4. The results in this section also have implications for finite-d systems, which we discuss in greater detail in Section 4.3.

4.2.1 Uniqueness of Fully Extended States

In this subsection, we derive a number of key results concerning fully-extended states (FESs) for $d = \infty$ systems with open boundaries (we leave the analysis of FESs in systems with closed boundaries for future work). The main result is uniqueness: each Krylov subspace contains exactly one FES, and therefore FESs can be used to label different Krylov subspaces. Our result holds for any local interaction range k, and hence generalises the results of Ref. [42], where this property was proven in the case of $k = 3$.

We begin by providing a few intermediate results. We first note the following theorem, originally derived in Ref. [42]:

Starting from any initial state in a $d = \infty$ system with open boundaries, a sequence of outward hops must necessarily eventually terminate after a finite number of moves, with the resulting state corresponding to an FES.

The proof of this, which we paraphrase, is quite simple and makes use of the quadrupole moment:

$$Q = \sum_{i=0}^{L-1} i^2 \, n_i \ , \tag{4.6}$$

where n_i counts the number of particles on each site. It is simple to check that any outward hop performed by two particles necessarily increases the value of Q by at least 2. However, for finite N and L, there is a clear upper bound on Q, given by the quadrupole moment of the particle configuration in which all particles are stacked on the right boundary site. This proves that, starting from any initial

configuration of particles, an FES must be reached after a finite number of outward hops. It also implies that all Krylov subspaces must have at least one FES.

Turning to our results, we now make use of this property to prove an important lemma that is useful for proving each Krylov subspace has a unique FES:

Assume that a Krylov sector contains more than one FES. Then it must be possible to map each FES in that sector to at least one other FES in the same sector by a sequence of only inward hops followed by a sequence of only outward hops.

In the following derivation, we will for simplicity generically denote outward hop gates involving two particles both hopping one site away from each other with the letter O, and inward hop gates involving a pair of particles hopping one site towards each other with the letter I. We use subscripts to indicate the order in which we apply the gates. For example, a sequence involving a single inward hop followed by two outward hops and then two further inward hops would be designated by

$$I_5\, I_4\, O_3\, O_2\, I_1 \ . \tag{4.7}$$

In the reasoning that will follow, the exact nature of each of these hops (i.e. where the hop is performed, and the number of sites separating the hopping particles) is not important, hence permitting the above simplified notation.

Consider a given initial FES and assume that it is not the unique FES within its Krylov sector. There must therefore exist a sequence of hops that will map it to a different FES. This sequence of moves necessarily starts with some number $n > 0$ of consecutive inward hops I_i, with $i = 1, \ldots, n$. Let O_{n+1} denote the first outward hop performed. The sequence of hops up to this point is hence given by

$$\ldots O_{n+1} I_n \ldots I_1 \ . \tag{4.8}$$

Before acting with the next hop in the sequence, we consider "inserting the identity":

$$\ldots (\widetilde{I}_m \ldots \widetilde{I}_1)(\widetilde{O}_m \ldots \widetilde{O}_1)\, O_{n+1} I_n \ldots I_1 \ , \tag{4.9}$$

for some set $\{\widetilde{O}_i\}_{i=1}^m$ of outward hops with $\widetilde{I}_{m-i+1} = \widetilde{O}_i^{-1}\ \forall\ i$. As we established, it is always possible to reach an FES from a given configuration of particles by

applying a finite number of consecutive outward hops, and so we may choose the operators $\{\widetilde{O}_i\}_{i=1}^{m}$ such that the state after the last outward hop $\widetilde{O}_m$ in the sequence is applied is an FES. Now, if the FES obtained after the application of $\widetilde{O}_m$ is different from the initial one, we have achieved the desired result, since the sequence $(\widetilde{O}_m \dots \widetilde{O}_1)O_{n+1}I_n \dots I_1$ maps from our initial FES to a different FES by using a sequence of purely inward then purely outward hops. If on the other hand, the resulting FES is identical to the starting one, we have learnt that the subsequence $O_{n+1}I_n \dots I_1$ of inward and outward hops can be replaced by the sequence of only inward hops $\widetilde{I}_m \dots \widetilde{I}_1$. Iterating this reasoning for every further outward hop O_i appearing in the overall hopping sequence, we see that at some point we will arrive at a sequence of purely inward and purely outward hops connecting our initial FES to a different FES, either by virtue of finding such a sequence of inward and outward hops at some intermediate step, or by virtue of successfully changing the original sequence of mixed inward and outward hops into an equivalent sequence of purely inward hops followed by purely outward hops.

We now prove our main result:

Each Krylov sector of a $d = \infty$ system with local range-k interactions and open boundaries contains a unique FES.

We proceed inductively. The cases of 1 and 2 particles are easy to verify. Assume that uniqueness holds up to FESs containing $N-1$ particles and consider an FES composed of N particles. We shall prove that there is no sequence of purely inward hops followed by purely outward hops that maps this FES to a different FES. Thus, uniqueness will follow as a direct consequence of our previous lemma. In what follows, we refer to a sequence of purely inward then purely outward hops as an O/I sequence. We now explore different structures of FESs on a case-by-case basis.

Case 1. Assume that in the FES there is at least one pair of particles separated by a sequence of $k-1$ or more empty sites:

$$\cdots \bullet \underbrace{\_ \cdots \_}_{\geq k-1} \bullet \cdots \quad . \tag{4.10}$$

We apply an O/I sequence with the aim of obtaining a different FES. During the application of the inward hops, the particles to the right and left of the separation of $k-1$ holes cannot interact with each other since the range-k gates can only act on particles separated by $k-2$ sites or fewer. Hence, the particles on each side of the $k-1$ empty sites form in their own right independent FESs, and so by our inductive hypothesis, the subsequent sequence of outward hops can only map the particles to the left and right of the $k-1$ holes back to their initial positions. Hence, the original FES is re-obtained.

Case 2. Assume that in the FES there is no pair of particles separated by $k-1$ or more holes, but there are two pairs or more separated by $k-2$ holes. Assume first that two of these pairs overlap.

$$\cdots\bullet\underbrace{\_\cdots\_}_{k-2}\bullet\underbrace{\_\cdots\_}_{k-2}\bullet\cdots \tag{4.11}$$

If the particle in the middle does not move during the inward hops of the O/I sequence, then the particles to its left cannot interact with the particles to its right, and by induction the only FES that can be reached is the original one via the same logic as in case 1. If the particle in the middle moves as part of the inward hops, then in performing an inward hop with one of its neighbouring particles, it will necessarily create a spacing of at least $k-1$ holes between itself and its other neighbouring particle. For example, if the middle particle performed an inward hop with the particle to its left, we would then have the configuration

$$\cdots\_\underbrace{\bullet\cdots\bullet}_{k-4}\_\underbrace{\_\cdots\_}_{k-1}\bullet\cdots \tag{4.12}$$

This has placed the middle particle out of range of the particle to its right, and so the two sides cannot interact during the inward hop sequence. If on the other hand the middle particle had originally hopped to the right, we would have

$$\cdots\bullet\underbrace{\_\cdots\_}_{k-1}\_\underbrace{\bullet\cdots\bullet}_{k-4}\_\cdots \tag{4.13}$$

once again disconnecting the two regions. This again splits the state into disconnected left and right regions during the O/I sequence, and we may use our

inductive hypothesis to see that the same FES will be retrieved after the outward hops have been applied.

We next assume that there are no two sequences of $k-2$ holes next to each other in the FES, i.e. there is at least one sequence of $k-3$ holes separating each pair of sequences of $k-2$ holes. Consider then the two sequences of $k-2$ holes that are closest to each other:

$$\cdots\bullet\underbrace{\_\cdots\_}_{k-2}\bullet\underbrace{\_\cdots\_}_{k-3}\bullet\cdots\bullet\underbrace{\_\cdots\_}_{k-3}\bullet\underbrace{\_\cdots\_}_{k-2}\bullet\cdots \tag{4.14}$$

If, during the inward hops of the O/I sequence, any of the particles between the two sets of $k-2$ holes remains immobile, then we again have by our induction hypothesis that the original FES is retrieved after the outward hops. Assume that this is not the case, i.e. all particles between the two sets of $k-2$ holes perform an inward hop at some point. Consider the second particle from the left in Eq. (4.14). If this particle performs an inward hop with the particle to its right, this will necessarily separate it by at least $k-1$ holes from the particle on its left:

$$\cdots\bullet\underbrace{\_\cdots\_}_{k-1}\_\bullet\underbrace{\cdots\bullet}_{k-5}\_\cdots\bullet\underbrace{\_\cdots\_}_{k-3}\bullet\underbrace{\_\cdots\_}_{k-2}\bullet\cdots \tag{4.15}$$

Hence the inductive hypothesis can be applied again to show the O/I sequence must yield the same FES. If this particle performs a hop instead with the particle to its left, this will create a spacing of at least $k-2$ holes between it and the particle to its right:

$$\cdots\_\bullet\underbrace{\cdots\bullet}_{k-4}\_\underbrace{\_\cdots\_}_{k-2}\bullet\cdots\bullet\underbrace{\_\cdots\_}_{k-3}\bullet\underbrace{\_\cdots\_}_{k-2}\bullet\cdots \tag{4.16}$$

If the new spacing equals $k-2$ holes, then once more, unless the two particles on either side of this new sequence of $k-2$ holes perform an inward hop, the regions on either side of them will be dynamically disconnected and the inductive hypothesis can be applied. A hop between the two particles, however, will again necessarily create a new spacing of at least $k-2$ holes to its right.

By iterating the above analysis, we see that at each step we reduce the distance between the sequence of $k-2$ holes on the right of the configuration in Eq. (4.14) and the next-nearest sequence of $k-2$ holes on its left. Eventually, we must again

arrive at a scenario with two neighbouring sequences of $k-2$ holes separated by a single particle, and we may use the same reasoning as in the scenario in Eq. (4.11).

Case 3. Assume that in the FES there is at most one pair of particles separated by $k-2$ holes, with all the other pairs being separated by $k-3$ holes (or less when there is overlap with the boundary). For reasons that will later be apparent, we refer to these as "blockage-free" FESs (BFESs). We now prove that two different BFESs must have different dipole moments X. Given that the dynamics considered in this work conserve X and that the FESs from cases 1 and 2 have already been shown to be unique, this proves uniqueness of the BFESs as well.

We first consider the case of BFESs that do not overlap with the boundary sites. We denote by i_0 the site of the leftmost particle and assume that the m-th particle from the left is separated from the previous one by $k-2$ holes, with all other pairs of particles being separated by $k-3$ holes.

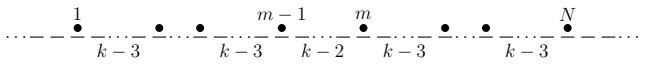

(4.17)

If there is no pair of particles separated by $k-2$ holes, we choose by convention to set $m = N+1$, hence $2 \leq m \leq N+1$. The dipole moment of the configuration in Eq. (4.17) is then

$$X = N\, i_0 - m + h(k,N)\ , \tag{4.18}$$

where $h(k,N) = (k-2)N(N-1)/2 + N + 1$ does not depend on m or i_0. We now imagine a different BFES that does not overlap with the boundary, which must possess different values of i_0, m or both. Its dipole moment would thus read

$$X' = N\, i_0' - m' + h(k,N)\ . \tag{4.19}$$

It is elementary to see that the equation $X = X'$ has no solution because $|i_0 - i_0'|$ is an integer and $2 \leq m' \leq N+1$. Hence when there is no overlap with the boundary, we have shown that BFESs of the type of Eq. (4.17) are uniquely determined.

We next allow for the possibility of overlap with the boundary. Hence we are considering BFESs in which at most one pair of particles is separated by $k-2$ sites,

and all other pairs are separated by $k-3$ sites, up to the possible exception of particles stacking on the boundary and a separation of fewer than $k-3$ sites between particles on the boundary and the next-nearest particles. An example of such a BFES for $k=6$, $L=21$, $N=12$, $X=133$ (with the leftmost site being site 0) is given by

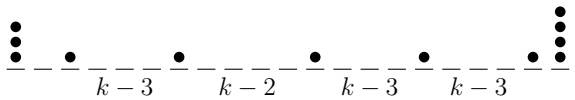

(4.20)

We shall show that the dipole moment X of a BFES uniquely determines the number of particles stacked on the right and left boundary sites. To begin with, we consider the case of the left boundary site. Say there are $N_L > 0$ particles stacked on top of it. The highest dipole moment $X_{\max}$ achievable in this case is attained when we place the remaining particles in the system as far to the right as possible, leading to the configuration

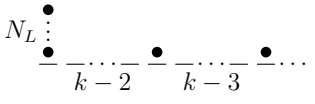

(4.21)

In the above configuration, after the sequence of $k-2$ holes, we repeat only sequences of $k-3$ holes until either all N particles are positioned or, if the right boundary is reached first, all remaining particles are stacked on the right boundary. Next, consider an integer $a \leq N_L$ and say we construct our BFES with $N_L - a \geq 0$ particles on the left boundary. In this case the lowest dipole moment $X'_{\min}$ is achieved with the configuration

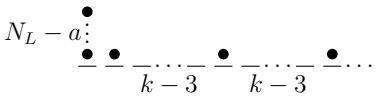

(4.22)

Here again, we only repeat sequences of $k-3$ holes between particles until all N particles are placed or we reach the right boundary and the remaining particles are stacked. By comparing Eq. (4.21) and Eq. (4.22), it is clear that $X'_{\min} > X_{\max}$. Thus a BFES with $N_L > 0$ particles on the left boundary cannot be dynamically connected to a BFES with $N_L - a \geq 0$ particles on it and vice versa.

We have thus shown that, for a BFES, the dipole moment X uniquely determines the number of particles N_L on the left boundary. Likewise, an identical demonstration shows that X also determines the number N_R of particles on the right boundary site. What remains to be determined are the positions of the particles in the bulk of the system; but with N_L and N_R already known. However, the positions of the remaining particles are also uniquely determined by the dipole moment using the same logic as for the BFES configuration with no boundary stacking in Eq. (4.17). This completes the proof.

A notable property of the BFESs discussed above is that, unlike the FESs discussed in cases 1 and 2, they do not have any regions that are necessarily disconnected during a sequence of inward hops. Their particular structure is of import to our discussion of the weakly Hilbert-space-fragmented phase in Section 4.4, where we identify dominant Krylov sectors in typical symmetry sectors of $d = \infty$ systems as those sectors that contain BFESs. We also discuss some of their properties further (in particular their "blockage-free" nature) in Section 4.2.3.

4.2.2 Blockages

In this subsection, we discuss how the FES associated with a Krylov sector in a $d = \infty$ chain can be used to analyse the dynamical structure of the states that sector contains. In particular, the FES can be used to search for the presence of "blockages": regions of the chain across which transport of particle number and dipole moment cannot occur within the Krylov subspace. When blockages are present in a Krylov subspace, then for all states in that subspace, no particles or dipole quanta are exchanged between the regions to the right and left of the blockage.

In the upcoming discussion, we will make use of the following result, which is an immediate corollary of the uniqueness of FESs:

Any state in a Krylov subspace of a $d = \infty$ system can be reached by applying a sequence of purely inward hops to that subspace's FES.

This result will be useful for identifying blockages. There are two general classes of blockages in locally interacting dipole-conserving systems, which we label as "frozen" and "active" blockages. They are defined as follows.

Frozen blockage: A frozen blockage is a sequence of at least $k-1$ frozen sites. As such, a frozen blockage prevents any kind of interaction between the regions to its left and right. Hence, particle number N and dipole moment X are independently conserved on either side of a frozen blockage. In a $d = \infty$ system, frozen blockages can be identified using FESs. Say in an FES there are two particles separated by a sequence of at least $k-1$ holes.

$$\cdots \bullet \underbrace{\_ \cdots \_}_{\geq k-1} \bullet \cdots \tag{4.23}$$

Since it is not possible for two particles separated by $k-1$ or more sites to interact, and since every state in the Krylov subspace can be reached by starting from the FES and applying inward hops, these $k-1$ sites remain empty throughout the subspace. Hence they form a frozen blockage, and the regions to their right and left are dynamically disconnected.

Active blockage: These kinds of blockages, discovered by Riccardo Senese [2], prevent the regions to their right and left from exchanging particles and dipole quanta. As such, they are similar to frozen blockages. However, active blockages do not contain sequences of $k-1$ or more frozen sites. The prohibition of transport of particles and dipole quanta arises rather from the particular configurations of particles that occur within the blockage. In $d = \infty$ systems, active blockages can also be identified using FESs. To see how, we first define an active "edge" to be a pair of particles separated by $k-2$ holes in the FES:

$$\cdots \bullet \underbrace{\_ \cdots \_}_{k-2} \bullet \cdots \tag{4.24}$$

Consider the case of a local region of an FES in which either two active edges overlap (as in Eq. (4.11)) or two active edges are separated by a sequence of pairs of particles themselves separated by $k-3$ holes (as in Eq. (4.14)). Then the region enclosed by

the two active edges constitutes an active blockage. The derivation follows identical logic to that used in Case 2 of the uniqueness proof of Section 4.2.1, where it is shown that there is no sequence of inward hops in which the regions to the right and to the left of two active edges interact. Hence, although the regions to the right and the left of an active blockage can exchange particles and dipole quanta with the region between the two active edges, they cannot make any such exchange with each other.

In this chapter, we mainly focus on the impact of frozen blockages, though we discuss some results concerning active blockages as well. A more in-depth discussion of the impact of active blockages can be found in [2].

4.2.3 Blockage-Free FESs

A particularly interesting class of FESs is those devoid of any blockage. We refer to such an FES as a "blockage-free fully extended state" (BFES). As first discussed in Section 4.2.1, the general structure of a BFES is that of an FES where only one pair of occupied sites is separated by $k-2$ holes and all other pairs are separated by $k-3$ holes, up to the possible exception of fewer than $k-3$ holes separating particles on the boundaries from those in the bulk. An example of a BFES was provided in Eq. (4.20). For $\nu < \nu_c$, it is impossible to construct a BFES in which the particles span the whole of the system: there will necessarily be a finite density of frozen sites separating either the rightmost particle of the state from the right boundary or the leftmost particle from the left boundary. Hence, although BFESs with $\nu < \nu_c$ are "blockage-free" in the sense that there is nothing preventing particles in one region of the BFES from interacting with particles in another region, nonetheless the dimension of their Krylov subspace is heavily restricted by the finite density of frozen sites, often leading to strong fragmentation. The critical density ν_c is the smallest density at which it is possible to construct a BFES in which the particles span the whole system. BFESs are important in our analysis of the weakly fragmented phase in Section 4.4, where we show that the Krylov subspaces which contain BFESs (or their finite-d equivalent) are dominant in their (N, X) sectors at densities $\nu > \nu_c$. To this end, we note the following important property:

There is exactly one BFES in each (N, X) symmetry sector.

Indeed, we have already shown in Section 4.2.1 that the structure of a BFES is uniquely determined by the (N, X) symmetry sector in which it is found. We furthermore show in Appendix B.1.1 that for each (N, X) sector, we can construct a BFES compatible with the values of N and X, completing the proof of the above statement.

Another important result which will be useful in our analysis of the strongly fragmented phase is as follows. We define a "sub-BFES" to be a subregion of contiguous sites in an FES which, if it were to be embedded in an otherwise empty chain, would have the structure of a BFES. We derive the following result concerning sub-BFESs in Appendix B.1.2:

Say an initial state is expanded via a series of outward hops to an FES. The resulting FES can then be divided into sub-BFESs such that no particles in different sub-BFESs interacted during the outward expansion.

We make use of this result in Section 4.3.2 to place bounds on the propagation of particles in the strongly fragmented phase.

4.3 Exact and Numerical Results for the Strongly Fragmented Phase

We now make use of the properties of FESs and blockages discussed in the previous section to derive numerous analytic and numerical results characterising the strongly fragmented phase of the model for general d, with a particular focus on $d = 2$ and $d = \infty$. We begin in Section 4.3.1 by developing "the FES picture": a useful approach for analysing the strongly fragmented phase in systems with finite d by using the results derived for $d = \infty$. We then use the FES picture in Section 4.3.2 to derive a constraint on how far particles can propagate from their point of origin in systems with general d. Restricted particle mobility is a key feature of the strongly fragmented phase, and indeed this sufficient constraint only generally occurs for

$\nu < \nu_c$. We use this constrained mobility to derive a sufficient condition for a given set of $k-1$ sites to constitute a frozen blockage. We then use this sufficient condition in Section 4.3.3 to prove that for states with $\nu < \nu_c$ in systems with $d = 2$ and $d = \infty$, the mean density of frozen sites $\overline{\rho}_F^{(d)}$ is non-vanishing and the model is in its strongly fragmented phase. We make further use of the FES picture in Section 4.3.4 to analytically study how for $d = 2$ and $d = \infty$, the frozen blockages subdivide typical random states into finite-sized dynamically disconnected "active bubbles" in the strongly fragmented phase. We conclude by providing numerical evidence in Section 4.3.5 supporting the analytic results derived, as well as showing the presence of a finite mean density of frozen sites at $\nu < \nu_c$ for other values of d, illustrating that the model is strongly fragmented for $\nu < \nu_c$ for other values of d as well.

4.3.1 The FES Picture

In Section 4.2.2, we saw how certain types of local configurations of particles and holes in the FES of a $d = \infty$ system allow us to identify blockages and frozen sites that characterise states in the entire Krylov sector. In fact, we can also use FESs to derive important results concerning systems at finite d as well. The concept of the "FES picture" presented here was developed in collaboration with Riccardo Senese and Abhishodh Prakash [2].

Given a state in a system S with d finite, we consider the same state in the context of an auxiliary system $\tilde{S}$ with $\tilde{d} = \infty$, and map the state to its FES in $\tilde{S}$. We may then use the resulting FES to search for the presence of blockages, noting that blockages identified in the auxiliary system $\tilde{S}$ are also blockages in the context of the original system S. Indeed, the Krylov sector $\mathcal{K}$ to which the state belongs in system S is a subsector of the Krylov sector $\tilde{\mathcal{K}}$ to which it belongs in $\tilde{S}$. Hence, if a series of $k-1$ holes are frozen for all states in $\tilde{\mathcal{K}}$, they are also frozen for all states in $\mathcal{K}$, forming a frozen blockage. Likewise, if two regions are separated by an active blockage for all states in $\tilde{\mathcal{K}}$, they must at least be separated by an active blockage in $\mathcal{K}$ as well (though the separation may also be a frozen blockage for finite d, since sites that are active at $\tilde{d} = \infty$ may be frozen at finite d).

In the following, we will refer to the approach outlined above, in which the presence of certain blockages in a state in a system S is determined by studying its corresponding FES in an auxiliary $\tilde{d} = \infty$ system, as the "FES picture". One notable consequence of the FES picture is that it implies that any state of a finite-d system with $\nu < \nu_c$ has a finite density of sites in blockages. This is because it is impossible to construct an FES at a density $\nu < \nu_c$ that does not have either a finite density of frozen sites in frozen blockages or a finite density of active edges (leading to active blockages). In [2], this is used to demonstrate that our model is in its strongly fragmented phase for $\nu < \nu_c$ for any value of d, and that even Krylov subspaces with only type-2 blockages (and hence no frozen sites) can form an exponentially vanishing fraction of their symmetry sectors. Here, we focus on proving that the model is strongly fragmented for $d = 2$ and $d = \infty$, where the strongest analytic results can be obtained, though we also present some analytic results and numerical studies indicative of the presence of strong fragmentation at higher values of d.

We also note that the FES picture will not necessarily capture all blockages present in a state at finite d, as the state may contain frozen sites and blockages that are invisible to the $\tilde{d} = \infty$ dynamics. For example, at finite d, a sequence of $k - 1$ sites each containing the maximal number $d - 1$ of particles may constitute a frozen blockage, but such a blockage would be invisible to the FES picture. We account for the possible presence of finite-d blockages in Section 4.4, where we numerically show the presence of the weakly fragmented phase for $\nu > \nu_c$.

4.3.2 A Sufficient Condition for Frozen Blockages

We here make use of the FES picture to establish a sufficient condition which, when satisfied by a group of particles, places strong bounds on how far they can propagate from their point of origin. This in turn leads to a sufficient condition for a set of $k - 1$ contiguous sites to form a frozen blockage. The frozen blockage condition we derive can only generally be satisfied in the strongly fragmented phase, where fractonic restrictions on particle mobility give rise to the presence of a finite density of frozen sites, leading to blockages and local active bubbles. As such, the

condition we shall establish can be used to efficiently identify many (though not all) of the frozen blockages in a system. We use it in the following subsections to analytically lower bound the average density of frozen sites for $d = 2$ and $d = \infty$, as well as the average density of active blockages in these systems.

We consider a system S with onsite dimension d and size L. Pick a site of the chain as the origin, that is, call it site 0. Assume that there are N_R particles in the region $\mathcal{R}$ of the chain that goes from site 0 to the right boundary of the chain, and let $L_R < L$ denote the total number of sites in $\mathcal{R}$. Assume furthermore for simplicity that the rest of the system is empty, though it will be clear that the results we derive also hold in the presence of other particles provided the particles to the left of site 0 are sufficiently far away that they never interact with the particles in $\mathcal{R}$. Label the initial positions of the particles in $\mathcal{R}$, from leftmost to rightmost, as $\{i_n^0\}_{n=1}^{N_R}$, and say those positions satisfy

$$i_n^0 \geq (n-1)(k-2). \tag{4.25}$$

We note that this constraint requires $L_R \geq (N_R - 1)(k-2) + 1$, which implies that in the thermodynamic limit $\lim_{L\to\infty} N_R/L_R \leq \nu_c$. We now show that condition Eq. (4.25) ensures that, under dynamical evolution of the system S, none of those N_R particles ever leaves the region $\mathcal{R}$.

Assume, for the sake of contradiction, that it is possible to start from an initial state with particles in $\mathcal{R}$ satisfying Eq. (4.25) and to move at least one of those particles to the left of site 0. This implies that in the FES picture, if the state were to be mapped to its corresponding FES in an auxiliary $\tilde{d} = \infty$ system, the position of the leftmost particle initially in $\mathcal{R}$ would be mapped to a position i_1 in the FES that satisfies $i_1 < 0$. From the results on BFESs of Appendix B.1, we know that it will be possible to divide this resulting FES into sub-BFESs such that the particles in each sub-BFES had no interaction with particles in other sub-BFESs during the outward expansion. Consider the leftmost of these sub-BFESs, and say that it is constituted of m particles in total. Since these particles only interacted

amongst themselves during the expansion in $\tilde{S}$, by Eq. (4.25) the local dipole moment X_0 of this leftmost BFES must satisfy

$$X_0 = \sum_{j=1}^{m} i_j \geq \sum_{j=1}^{m} (j-1)(k-2) = \frac{m(m-1)}{2}(k-2). \tag{4.26}$$

We next consider what sub-BFES made of m particles would have the highest possible dipole moment while satisfying $i_1 < 0$. Clearly, this is given by $i_1 = -1$ and $i_j = (j-1)(k-2)$ for $j = 2, \ldots, m$. Hence, the leftmost sub-BFES must have a local dipole moment of at most

$$-1 + \sum_{j=2}^{m} (j-1)(k-2) = -1 + \frac{m(m-1)}{2}(k-2) < X_0 \,. \tag{4.27}$$

As this is less than the lower bound in Eq. (4.26), the leftmost particle cannot propagate past site 0 in the auxiliary system with $\tilde{d} = \infty$, and also consequently cannot propagate past site 0 in the system with finite d. Hence, regardless of the value of d, particles that have initial positions satisfying Eq. (4.25) cannot propagate left of site 0 by interacting solely among themselves.

An immediate corollary of this is as follows:

Say a given state has a sequence of $k-1$ holes, and the particles to the right and left of these holes satisfy mirrored versions of the condition in Eq. (4.25)*. Those holes are then frozen sites, and constitute a frozen blockage.*

By "mirrored versions" of Eq. (4.25), we mean the following. Consider a sequence of $k-1$ holes:

$$\cdots \overset{\overset{k-1}{\overbrace{\_\cdots\_}}}{\vdots\quad\vdots} \cdots \tag{4.28}$$

We then impose that the particles to the right of the right vertical dashed line satisfy the no-propagation constraints in Eq. (4.25) (with site 0 corresponding to the first site after the vertical line), and the particles to the left of the left line satisfy a mirrored version of the constraints, $i_n^0 \leq -k - (n-1)(k-2)$ (labeling particles from rightmost to leftmost). It is then clear from the derived result that

the particles on either side of the $k-1$ holes are unable to cross the vertical dashed lines, and the $k-1$ holes form a frozen blockage. We note that these conditions can only be generally satisfied for $\nu < \nu_c$, i.e. in the strongly fragmented phase.

4.3.3 Average Density of Frozen Sites and Active Blockages

We shall now make use of the sufficient condition in Eq. (4.25) to derive an expression for a lower bound on the mean density of frozen sites $\overline{\rho}_F^{(d)}(k, \nu L, L)$ (as defined in Eq. (4.5)) for $\nu < \nu_c$. For $d = 2$ and $d = \infty$, we can furthermore take the thermodynamic limit of this expression, showing that the mean density of frozen sites is non-vanishing for $\nu < \nu_c$. We argue that this implies the model is in its strongly fragmented phase. We shall also derive a lower bound on the mean density of active blockages, showing it to be non-vanishing for $\nu < \nu_c$ and $d = 2, \infty$ as well.

Rephrasing the formula in Eq. (4.5), we may compute the mean density of frozen sites in a state with N particles, L sites, and local range-k interactions by calculating

$$\overline{\rho}_F^{(d)}(k, N, L) = \frac{1}{L} \frac{\beta_F^{(d)}(k, N, L)}{D^{(d)}(N, L)}, \tag{4.29}$$

where $\beta_F^{(d)}(k, N, L)$ is a sum counting the number of frozen sites in each of the $D^{(d)}(N, L)$ possible states with N particles. We proceed to put a lower bound on $\beta_F^{(d)}(k, N, L)$ using the results of Section 4.3.2. We again consider the case of $k-1$ holes:

$$\cdots \underbrace{\_ \cdots \_}_{k-1} \cdots \tag{4.30}$$

with the particles on either side satisfying mirrored versions of the constraint in Eq. (4.25). As stated before, this implies the $k-1$ holes in the configuration are frozen and constitute a frozen blockage. Hence, by counting the number of times the configuration in Eq. (4.30) occurs in a given state with these constraints satisfied, we can lower bound $\beta_F^{(d)}(k, N, L)$. In particular, we lower bound it by summing first over all $\mathcal{O}(L)$ possible positions in the chain at which the sequence of $k-1$ holes in Eq. (4.30) can be situated, and then for each such position counting the number of states for which the particles on either side of the $k-1$ holes satisfy mirrored

versions of the no-propagation constraints in Eq. (4.25). Each such occurrence of $k-1$ holes contributes at least one new frozen site to the total; we cannot count more than a single frozen site per occurrence, as then there would be a risk of double-counting from when two sequences of $k-1$ holes overlap. This yields

$$\begin{aligned}\beta_F^{(d)}(k,N,L) \geq \\ \sum_{L_R=0}^{L-k+1} \sum_{N_R=N_{\min}}^{N_{\max}} b^{(d)}(k,N_R,L_R) b^{(d)}(k,N-N_R,L-L_R-k+1) \\ \equiv \tilde{\beta}_F^{(d)}(k,N,L)\ .\end{aligned} \tag{4.31}$$

In the expression above, the summation variable L_R denotes the number of sites to the right of the $k-1$ holes in Eq. (4.30), and N_R denotes the number of particles to the right of the holes. The function $b^{(d)}(k,N_R,L_R)$ denotes the total number of ways to arrange N_R particles over L_R sites with onsite dimension d such that the particles obey the constraint in Eq. (4.25). Hence $b^{(d)}(k,N_R,L_R)$ gives the number of possible particle arrangements to the right of the $k-1$ holes, and $b^{(d)}(k,N-N_R,L-L_R-k+1)$ gives the analogous quantity for the region to their left. The upper and lower bounds on the summation over N_R in Eq. (4.31) are

$$N_{\min} = \max(0, N - \lfloor (L-L_R-2)/(k-2) \rfloor) \tag{4.32}$$

$$N_{\max} = \min(N, \lfloor (L_R+k-3)/(k-2) \rfloor)\ , \tag{4.33}$$

where the brackets $\lfloor \ldots \rfloor$ denote the floor function. These bounds ensure that the number of particles to the right and left of the $k-1$ holes is small enough that the conditions of Eq. (4.25) can be satisfied.

For most values of d, the summations above have to be performed numerically. However, for $d=2$ and $d=\infty$, there are simple closed-form expressions for the function $b^{(d)}(k,N_R,L_R)$. This makes it possible to analytically take the thermodynamic limit of Eq. (4.29), resulting in a simple lower bound on the density of frozen sites. We perform these calculations next.

Case 1: $d = 2$

In this case, the total dimension of an N sector is simply given by $D^{(2)}(N, L) = \binom{L}{N}$, the number of ways of arranging N particles amongst L sites. The function $b^{(2)}(k, N_R, L_R)$ can be written out as the explicit summation

$$b^{(2)}(k, N_R, L_R) = \sum_{i_{N_R}=(N_R-1)(k-2)}^{L_R-1} \cdots \sum_{i_2=(k-2)}^{i_3-1} \sum_{i_1=0}^{i_2-1} 1, \tag{4.34}$$

where we are counting all possible positions i_1 for the first particle, i_2 for the second particle, and so on, consistent with the constraints in Eq. (4.25). We perform this summation explicitly in Appendix B.2.1, arriving at the closed-form expression

$$b^{(2)}(k, N_R, L_R) = \binom{L_R + (k-2)}{N_R} \frac{L_R - (N_R - 1)(k-2)}{L_R + (k-2)}. \tag{4.35}$$

In the thermodynamic limit, the sums in Eq. (4.31) become integrals, and the sum over N_R can be approximated using Laplace's method. Referring to the general thermodynamic-limit equation (B.19) derived in Appendix B.2.2, the final result is

$$\lim_{L\to\infty} \overline{\rho}_F^{(2)}(k, \nu\, L, L) \geq (1-\nu)^{-(k-3)}(1-\nu/\nu_c)^2 \ , \tag{4.36}$$

where $\nu_c = (k-2)^{-1}$ as before. We note this is non-vanishing up to $\nu = \nu_c$, following which some of the assumptions made in writing the sum Eq. (4.31) are no longer valid.

Case 2: $d = \infty$

Here, the dimension of the N sector is given by $D^{(\infty)}(N, L) = \binom{L+N-1}{N}$, since due to the unlimited stacking, the top of every particle counts as its own independent site. We also have that

$$b^{(\infty)}(k, N_R, L_R) = \sum_{i_{N_R}=(N_R-1)(k-2)}^{L_R-1} \cdots \sum_{i_2=(k-2)}^{i_3} \sum_{i_1=0}^{i_2} 1, \tag{4.37}$$

where the adjusted upper summation bounds reflect that particles can now be stacked. This summation can also be performed explicitly (see Appendix B.2.1), yielding

$$b^{(\infty)}(k, N_R, L_R) = \frac{L_R - (N_R - 1)(k-2)}{L_R + k - 2} \binom{L_R + N_R + k - 3}{N_R}. \tag{4.38}$$

Referring to the general expression (B.21) derived in Appendix B.2.2, the thermodynamic limit of Eq. (4.31) can then be taken, resulting in

$$\lim_{L\to\infty} \overline{\rho}_F^{(\infty)}(k, \nu L, L) \geq (1+\nu)^{k-3}(1-\nu/\nu_c)^2, \tag{4.39}$$

which is again non-vanishing for $\nu < \nu_c$.

We now explain why a non-zero mean density of frozen sites, and in particular of frozen holes, implies the model is in its strongly fragmented phase. In Appendix B.3, we argue by self-averaging that the derived lower bounds on the mean density $\overline{\rho}_F^{(d)}(k, \nu\, L, L)$ for $d = 2$ and $d = \infty$ should also individually apply to almost all states in the thermodynamic limit, i.e. almost all states with filling ν should have a density of frozen sites greater than that in Eq. (4.36). This in turn implies that almost all states belong to Krylov subspaces $\mathcal{K}$ whose dimensions form an exponentially vanishing fraction of their respective (N, X) sector as L is increased. Indeed, for the case of $d = 2$, we recall that $D^{(2)}(N, L) = \binom{L}{N}$. The dimension of a Krylov subspace with a density ρ_F^0 of frozen holes is on the other hand upper bounded by

$$\dim(\mathcal{K}) \leq \binom{(1-\rho_F^0)L}{N}. \tag{4.40}$$

Hence, $\dim(\mathcal{K})$ grows at an exponentially slower rate with L than $D^{(2)}(N, L)$. On the other hand, since there are only polynomially many values of X compatible with a given N, the dominant (N, X) symmetry sectors must have a dimension $D^{(2)}(N, X, L)$ that grows at the same exponential rate as $D^{(2)}(N, L)$, and is at most polynomially suppressed in L:

$$D^{(2)}(N, X, L) \sim L^{-\alpha} D^{(2)}(N, L) \text{ for dominant } (N, X) \text{ sectors}$$

for some power α depending on X. Hence,

$$\dim(\mathcal{K})/D^{(2)}(N, X, L) \xrightarrow{L\to\infty} 0 \text{ for dominant } (N, X) \text{ sectors.}$$

We thus see that almost all states at $\nu < \nu_c$ for $d = 2$ are part of Krylov subspaces that form a vanishingly small part of their (N, X) symmetry sectors. This implies that the dominant (N, X) sectors to which these states belong do not have a

dominant Krylov subspace and are strongly fragmented. Thus the model is in its strongly fragmented phase by the test of Eq. (4.2). The same reasoning can also be applied to our results for a finite density of frozen sites for $d = \infty$. In [2], it is analytically shown that a finite mean density of frozen holes implies strong fragmentation for other values of d as well.

As an aside, similarly to the case of frozen blockages, one can also use the no-propagation constraints of Section 4.3.2 to put a loose lower bound on the mean density of active blockages in states at a given ν, showing that active blockages are present in typical states at all fillings $\nu < \nu_c$ for $d = 2$ and $d = \infty$ as well. To this end, we consider the following particle configuration:

$$\cdots \vdots \underbrace{\circ\cdots\circ}_{k-3} \bullet \underbrace{\circ\cdots\circ}_{k-2} \bullet \underbrace{\circ\cdots\circ}_{k-2} \bullet \underbrace{\circ\cdots\circ}_{k-3} \vdots \cdots , \tag{4.41}$$

where again the particles on either sides of the vertical dashed lines satisfy the no propagation constraints of Eq. (4.25). Let $\overline{\rho}^{(d)}_{AB}(k, N, L)$ denote the mean number of occurrences of this configuration in a random state with N particles and L sites, with the no-propagation constraints satisfied on both sides. In the thermodynamic limit, this value can be computed following an identical procedure to that used to lower bound the mean density of frozen sites. Referring to Eqs. (B.19) and (B.21) in Appendix B.2.2, the final result is

$$\lim_{L\to\infty} \overline{\rho}^{(2)}_{AB}(k, \nu L, L) = \nu^3(1-\nu)^{2k-3}(1-\nu/\nu_c)^2 \tag{4.42}$$

and

$$\lim_{L\to\infty} \overline{\rho}^{(\infty)}_{AB}(k, \nu L, L) = \nu^3(1+\nu)^{2k}(1-\nu/\nu_c)^2. \tag{4.43}$$

By self-averaging, we also expect this to lower bound the density of active blockages of the type in Eq. (4.41) in a typical thermodynamically large state.

4.3.4 Active Bubble Density Function

As we have shown, models with $\nu < \nu_c$ at $d = 2$ or $d = \infty$ feature a finite density of frozen blockages in typical states. Hence, dynamical evolution for almost all initial states is confined to local regions that are dynamically disconnected from each other. Following the terminology of Ref. [41], we refer to these regions as "active bubbles". More specifically, we define an active bubble to be a set of contiguous sites containing at least 2 particles such that:

- Nowhere in the active bubble is there a frozen blockage, i.e. a sequence of $k-1$ or more frozen sites.
- The leftmost and rightmost sites of the active bubble are not frozen sites.
- The first $k-1$ sites to the left and right of the active bubble each constitute a frozen blockage.

Hence no regions within an active bubble are dynamically disconnected. We note that active bubbles by this definition can contain active blockages: this is because active blockages do not prevent the regions to their right and left from interacting, but rather simply prevent the transport of particles and dipole quanta. Since neighbouring active bubbles are completely dynamically disconnected from each other, we may independently map out the local Krylov sectors associated with each active bubble, where a local Krylov sector consists of all particle configurations available to an active bubble under dynamical evolution. A simple example in a $d = 2$, $k = 5$ system is an active bubble consisting of $x = 2$ particles spread out over $\ell = 4$ sites, which would have two states in its local Krylov sector:

$$\{\_\ \underline{\bullet}\ \underline{\bullet}\ \_\ ,\ \underline{\bullet}\ \_\ \_\ \underline{\bullet}\}\,. \tag{4.44}$$

An active bubble with $x = 2, \ell = 5$ would also have two states:

$$\{\_\ \underline{\bullet}\ \_\ \underline{\bullet}\ \_\ ,\ \underline{\bullet}\ \_\ \_\ \_\ \underline{\bullet}\}\,. \tag{4.45}$$

We shall refer to the different particle configurations within local Krylov sectors as "active bubble configurations".

Similarly to how we studied the mean density of frozen sites in Section 4.3.3, we now study the average densities of different types of active bubbles for $d = 2$ and $d = \infty$. We again take the average over the entire N sector for each value of ν, and we expect self-averaging to occur in thermodynamically large states as argued in Appendix B.3. We begin by considering the case of $d = 2$. We define the active bubble density function, $A_2(x, k, N, L)$, to give the average density of occurrences of active bubbles that contain exactly x particles in states of size L with N particles. We may expand $A_2(x, k, N, L)$ as a sum over ℓ, where ℓ is the total number of sites a given active bubble occupies:

$$A_2(x, k, N, L) = \sum_{\ell=\ell_{2,\min}(x,k)}^{\ell_{2,\max}(x,k)} m_2(x, \ell, k) a_2(x, \ell, k, N, L). \tag{4.46}$$

In the above expression, $\ell_{2,\min}(x, k)$ and $\ell_{2,\max}(x, k)$ are respectively the smallest and largest number of sites compatible with an active bubble with x particles at interaction range k; the multiplicity function $m_2(x, \ell, k)$ gives the total number of active bubble configurations compatible with a particular x, ℓ, and k; and the function $a_2(x, \ell, k, N, L)$ gives the average density of occurrences of any particular active bubble configuration compatible with x, ℓ, and k in states with N particles and L holes (we note that this density is independent of how the x particles are actually arranged amid the ℓ sites). The value of the function $\ell_{2,\min}(x, k)$ has to be determined on a case-by-case basis; $\ell_{2,\max}(x, k)$, on the other hand, has an exact expression. Since an active bubble cannot have any sequences of $k - 1$ frozen sites, the most dilute active bubble configuration possible is constituted of a series of particles each separated by $k - 2$ holes. Hence, we have that

$$\ell_{2,\max}(x, k) = 1 + (k - 1)(x - 1). \tag{4.47}$$

As a simple example, returning to the case of $k = 5$ and $x = 2$ mentioned above, we see from Eqs. (4.44) and (4.45), that

$$\begin{aligned} \ell_{2,\min}(2, 5) &= 4, \\ \ell_{2,\max}(2, 5) &= 5, \\ m_2(2, 4, 5) = m_2(2, 5, 5) &= 2. \end{aligned} \tag{4.48}$$

To lower bound the function $a_2(x, \ell, k, N, L)$, we restrict our attention to active bubbles for which the $k-1$ frozen sites to the right and left of the active bubble are holes, and for which the remaining particles beyond those frozen sites obey mirrored versions of the no-propagation condition in Eq. (4.25). This allows us to lower bound $a_2(x, \ell, k, N, L)$ using an identical approach to the one used for the average density of frozen blockages in Section 4.3.3. Referring to Eq. (B.19) in Appendix B.2.2, we find that in the thermodynamic limit

$$\lim_{L\to\infty} a_2(x, \ell, k, \nu L, L) \geq \nu^x (1-\nu)^{\ell-x+2}(1-\nu/\nu_c)^2. \tag{4.49}$$

Applying this to the $x = 2, k = 5$ example, we may lower bound the average density of active bubbles containing 2 particles, and we find that in the thermodynamic limit

$$\begin{aligned}\lim_{L\to\infty} A_2(x=2,&k=5,\nu L, L)\\ &\geq 2\nu((1-\nu)^4 + (1-\nu)^5)(1-3\nu)^2.\end{aligned} \tag{4.50}$$

In Appendix B.4, we also work out $\lim_{L\to\infty} A_2(x, k = 5, \nu L, L)$ for $x = 3$ to $x = 5$ by computing the necessary values of the multiplicity function $m_2(x, \ell, k)$. We plot the derived lower bounds explicitly in Fig. 4.3, where we compare them to the results of exact numerical simulations at large L.

The active bubble density function $A_\infty(x, k, N, L)$ for $d = \infty$ can be lower bounded following almost identical steps. We again decompose in terms of the different active bubble configuration densities:

$$A_\infty(x, k, N, L) = \sum_{\ell=\ell_{\infty,\min}(x,k)}^{\ell_{\infty,\max}(x,k)} m_\infty(x, \ell, k) a_\infty(x, \ell, k, N, L). \tag{4.51}$$

The above functions have the same definitions as their $d = 2$ counterparts, with the only difference being they take into account $d = \infty$ dynamics. It's apparent that $\ell_{\infty,\max}(x, k) = 1 + (x-1)(k-1)$; furthermore, since an active bubble in a $d = \infty$ system can always be expanded out to its local sub-FES, we also have that

$$\ell_{\infty,\min}(x, k) = 1 + (x-1)(k-2), \tag{4.52}$$

corresponding to an FES where all pairs of particles are separated by $k-3$ holes.

In the thermodynamic limit, we have from the general expressions (B.21) derived in Appendix B.2.2 that

$$\begin{aligned}\lim_{L\to\infty} a_\infty(x,\ell,&k,\nu L,L)\\ &\geq \nu^x(1+\nu)^{-(x+\ell+2)}(1-\nu/\nu_c)^2\end{aligned} \tag{4.53}$$

Returning to our $x = 2, k = 5$ example, we note that

$$\begin{aligned}\ell_{\infty,\min}(2,5) &= 4,\\ \ell_{\infty,\max}(2,5) &= 5,\\ m_\infty(2,4,5) &= 2,\\ m_\infty(2,5,5) &= 3.\end{aligned} \tag{4.54}$$

The difference in value between $m_\infty(2,5,5)$ and $m_2(2,5,5)$ arises due to the possibility for particles to be stacked when $d = \infty$. Hence we find that

$$\begin{aligned}\lim_{L\to\infty} \mathcal{A}^\infty(x=2,&k=5,\nu L,L)\\ &\geq \nu^2(2(1+\nu)^{-8}+3(1+\nu)^{-9})(1-3\nu)^2.\end{aligned} \tag{4.55}$$

We work out the lower bounds for $x = 3$ to $x = 6$ for this function in Appendix B.4 by computing the necessary values of the multiplicity function $m_\infty(x,\ell,k)$, and plot these in Fig. 4.3. In the following subsection, we numerically confirm that the derived lower bounds are valid at all ν and tight for $\nu \ll \nu_c$. Hence, the constraints in Eq. (4.25) lead to an accurate analytic understanding of how typical states in the $\nu \ll \nu_c$ regime subdivide into active bubbles of different sizes, while also giving some understanding concerning the distribution of bubbles at higher ν.

4.3.5 Numerical Results

We now proceed to numerically confirm the results of the previous subsections, as well as to provide evidence that models with $d = 3$ and $d = 4$ are strongly fragmented for $\nu < \nu_c$ as well. We begin by numerically computing the mean densities of frozen sites and of different sizes of active bubbles for $d = 2$ and $d = \infty$, and comparing these to the analytic lower bounds derived in Section 4.3.3 and Section 4.3.4. We then make use of the FES picture to numerically show for various values of k that models with $d = 3$ and $d = 4$ have a finite density of frozen sites for

$\nu < \nu_c$, indicating them to be in the strongly fragmented phase at these densities as well. We also show that the standard deviation of the density of frozen sites decreases with increasing system size, indicating the presence of self-averaging.

On several occasions in this section, we map various initial states to their corresponding FES to make use of the FES picture. We have developed an efficient algorithm to perform this procedure taking advantage of some of the special properties of sub-BFESs derived in Appendix B.1. We do not describe the algorithm here for lack of space; however, the interested reader is directed to the appendices of [2] for the details.

Comparison with analytic bounds:

We assess here the validity of the analytic lower bounds computed in Section 4.3.3 and Section 4.3.4 by comparing them to the results of numerical computations at large system sizes.

In Fig. 4.3(a), we compare analytic and numerical results for the mean active bubble densities of a $d = \infty$ system with $k = 7$. The analytic lower bounds are given by the formulas in Eq. (4.51) and Eq. (4.53), with the multiplicity function $m_\infty(x, \ell, k)$ being calculated in Appendix B.4. As concerns the numerical trends, for each density ν, 100 random states with $L = 10^6$ were generated and mapped to their corresponding FESs. Frozen blockages could then be directly identified from the FES as sequences of $k - 1$ or more holes, from which the FES was divided into active bubbles. The densities of active bubbles with different particle numbers were then computed and averaged over to yield the numerical data.

We note that for small fillings ν, the analytic lower bounds are very close to the numerical densities in this figure, whereas the two start to diverge for intermediate values of ν. The close match for small ν indicates that for most active bubbles in the system at low particle densities, the no-propagation conditions in Eq. (4.25) are satisfied by the particles outside the active bubble. This is to be expected: for the condition to be violated, there would have to be a dense group of particles close to the active bubble with a local density greater than ν_c, which is highly unlikely for $\nu \ll \nu_c$.

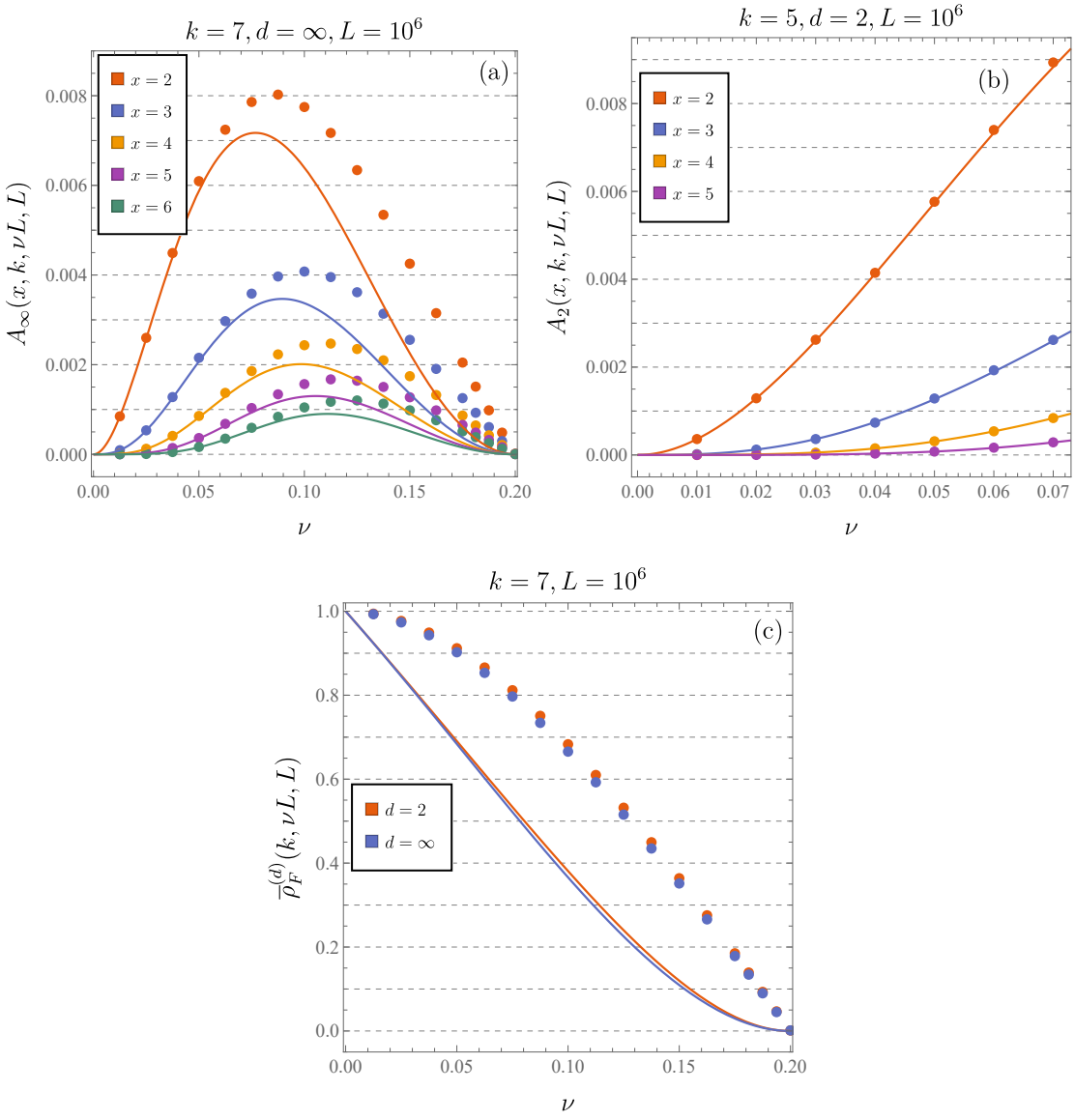

Figure 4.3: Comparisons between numerical densities and analytic lower bounds for systems of size $L = 10^6$. The functions used for the lower bounds are presented in Appendix B.4 for (a) and (b) and Eqs. (4.36) and (4.39) for (c). In (a), the active bubble densities of 100 random states were averaged over for each value of ν at $k = 7$ and $d = \infty$. In (b) 10 random states were sampled per value of ν at $k = 5$. We note the tightness of the bound for $\nu \ll \nu_c$ in both cases. In (c), the density of frozen sites was determined by averaging over the densities of 100 random states per value of ν for a system with $k = 7$ and $L = 10^6$. The frozen sites were identified using the FES picture, and hence the numerical density is exact for $d = \infty$ and a lower bound for $d = 2$. The standard error on the data, given by the standard deviation divided by the square root of the number of samples, is too small to see on the plots.

In Fig. 4.3(b), we perform the same comparison for a $d = 2$ system with $k = 5$. The analytic lower bounds are given by Eq. (4.46) and Eq. (4.49), with $m_2(x, \ell, k)$ being calculated in Appendix B.4. For the numerical calculations in this model, the FES picture could not be used, as some of the frozen blockages in a $d = 2$ system would be invisible to it. Instead, the numerical active bubble densities were determined by dividing randomly drawn states with filling ν into "initial" active bubbles of unfrozen sites, mapping out the local Krylov sectors of these active bubbles while unfreezing neighbouring sites as necessary, merging active bubbles which then overlapped, and then continuing to map out local Krylov sectors of the newly merged active bubbles and merging the results until no further merging occurred. As this was a numerically intensive procedure, only small values of ν could be studied, with 10 samples per data point. The invisible standard error in the resulting data, however, indicates that self-averaging was ensuring the accuracy of the data collected. We note again that there is close agreement between the exact numerical data and the analytic lower bound at small ν.

In Fig. 4.3(c), we compare analytical and numerical results for the density of frozen sites for systems with $d = 2$ and $d = \infty$, and with $k = 7$ and $L = 10^6$. The analytic lower bounds are given by Eq. (4.36) and Eq. (4.39). The numerical values were averaged from 100 random initial states for each value of ν. For both $d = 2$ and $d = \infty$, the number of frozen sites was computed by mapping the states to their corresponding FESs, and counting the number of sites that were part of frozen blockages. For $d = \infty$, this yields the exact number of frozen sites in a given state; for $d = 2$, this yields a lower bound, as the FES picture can miss the presence of some frozen sites. Nonetheless, we expect it to be a tight lower bound, as most frozen blockages should be constituted of holes for $\nu < \nu_c$. The numerical results also confirm the validity of the analytic $d = 2$ lower bound.

For both values of d, we again note a closer match for $\nu \ll \nu_c$. We also note that for ν close to ν_c, the numerical results show the same critical scaling $\rho_F \sim (\nu_c - \nu)$ of the frozen sites as that observed in [41]; the analytic lower bound, on the other hand, shows a weaker $\rho_F \sim (\nu_c - \nu)^2$ scaling.

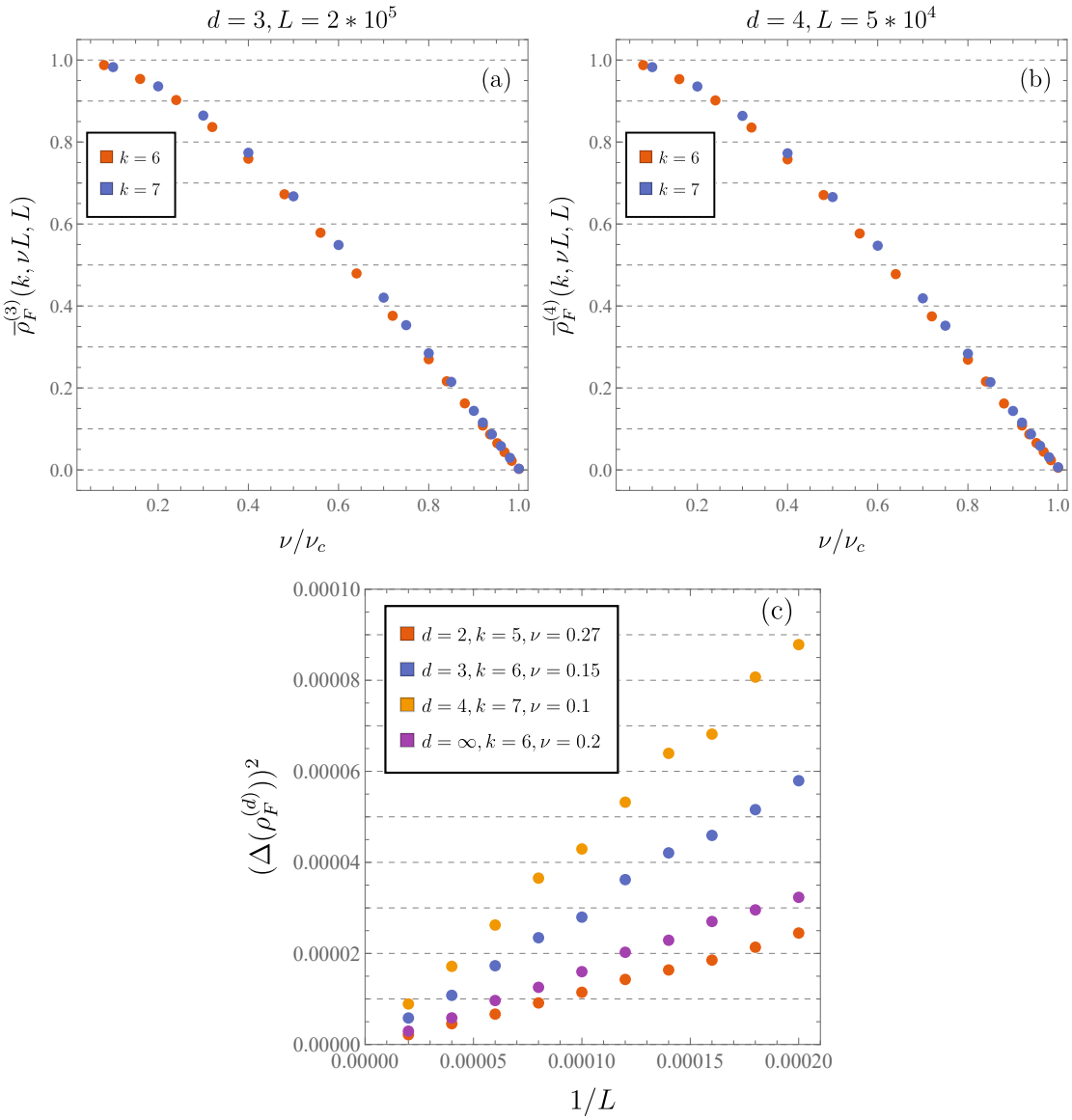

Figure 4.4: In (a) and (b), a numerical lower bound on the mean density of frozen sites is presented for systems with $d = 3$, $L = 2 * 10^5$ and $d = 4$, $L = 5 * 10^4$ respectively. The lower bounds were computed using the FES picture. 200 random states were sampled per data point in (a) and 1000 per data point in (b). In both plots the standard error is too small to see. In (c), the variance in the numerically determined lower bound of frozen sites is plotted as a function of $1/L$ for various systems. The linear trend is indicative of strong self-averaging [113].

Strong fragmentation for $d = 3$ and $d = 4$:

We here present numerical evidence that typical states at fillings $\nu < \nu_c$ in systems with $d = 3$ and $d = 4$ also have a finite density of frozen sites, and hence that these models are in the strongly fragmented phase at these fillings as well. Fig. 4.4(a)

presents a lower bound for $d = 3$ and $k = 6, 7$, and Fig. 4.4(b) does the same for $d = 4$. The numerical lower bounds were obtained using the FES picture as was done in the $d = 2$ case. The $d = 3$ and $d = 4$ data sets are very similar. However, the true densities of frozen sites in both systems may be more distinct due to the possible presence of frozen blockages not detected by the FES picture. It is worth noting that in all cases a critical scaling of $\rho_F \sim (\nu_c - \nu)$ is observed near the critical point.

Fig. 4.4(c) presents some self-averaging tests done at various values of d, ν, and k. Similar tests were also done for the mean active bubble densities. These tests show strong self-averaging occurring, with the variance vanishing as $\sim 1/L$ as L is increased. This ensures that the analytic and numerical lower bounds determined for the average densities of frozen sites in these models also apply to individual states in the thermodynamic limit. The observed self-averaging is also useful as it indicates that even with our relatively small number of samples, we should still be getting precise results due to the large system sizes considered.

4.4 Numerical results for the Weakly Fragmented Phase

In this section, we provide numerical evidence that, for $\nu > \nu_c$ and general d, the model is in its weakly fragmented phase. This means that in the thermodynamic limit almost all states at these fillings belong to the dominant Krylov subspace of a weakly fragmented (N, X) sector. Indeed, we show numerically that states with $\nu > \nu_c$ are almost always in the same Krylov sector as a special kind of state we name a "blockage-free extended state" (BES). These BESs constitute a generalisation to finite d of the structure of $d = \infty$ "blockage-free fully extended states" defined in Section 4.2.3. There is a unique BES in each (N, X) sector; hence, if random initial states are almost always in the same Krylov sector as a BES, it means that the Krylov sectors containing BESs dominate in their respective (N, X) sectors, and that these (N, X) sectors are weakly fragmented.

Our results in this section are also of interest as they provide an explanation as to why the critical density ν_c is independent of d. For any value of d, ν_c is the

smallest density at which it is possible to construct a BES in which the particles span the entire system. Hence, ν_c is the smallest density for any d at which one obtains "blockage-free" Krylov subspaces that do not contain any frozen sites nor any active blockages. Furthermore, since there is a unique BES per (N, X) sector, there is also a unique blockage-free Krylov subspace per (N, X) sector for $\nu > \nu_c$. It is natural to expect these particular Krylov subspaces to dominate their symmetry sectors, and thus the model is weakly fragmented for $\nu > \nu_c$.

4.4.1 Blockage-Free Extended States and Contracted States

Blockage-free extended states (BESs) are a finite-d generalisation of the blockage-free fully extended states (BFESs) defined in Section 4.2.3. BESs are states to which no outward hop can be applied, and where there are no blockages between the sites occupied by the leftmost and rightmost particles in the state: particles in any region of a BES can interact with particles in any other region. For the case of BESs with no particles on the leftmost and rightmost boundary sites, we define them to be identical in structure to $d = \infty$ BFESs: they consist of a series of particles separated by holes, with at most one pair of particles being separated by $k-2$ holes and all other pairs being separated by $k-3$ holes. For example, a BES with $d = 4$, $k = 5$, $L = 16$, $N = 5$, $X = 43$ (with site 0 being the leftmost site) would be:

$$\_\ \_\ \overset{\bullet}{\underset{k-3}{\_}}\ \_\ \_\ \overset{\bullet}{\underset{k-3}{\_}}\ \_\ \_\ \_\ \overset{\bullet}{\underset{k-2}{\_}}\ \_\ \_\ \overset{\bullet}{\underset{k-3}{\_}}\ \_\ \_\ \overset{\bullet}{\underset{k-3}{\_}}\ \_ \ .$$

The particular value of d comes into play when the particles in the BES overlap with the boundaries, leading to a "pile-up". In a $d = \infty$ BFES, this pile-up is entirely confined to the boundary sites. The bounded maximal onsite occupancy of finite-d systems, however, implies that the pile-up must be spread out over several sites. The general form of this pile-up is as follows. Say there is a pile-up of m particles on the left boundary of the system: we then have that in a BES, the particles in the left-boundary pile-up will occupy the $\lceil m/(d-1) \rceil$ leftmost sites of the system, with the first $\lfloor m/(d-1) \rfloor$ of these sites having the maximal number $d-1$ of particles, and the last site of the pile-up containing the remaining particles

(if there are any). The next occupied site to the right of the left-boundary pile-up can be separated by $k-2$ holes or fewer from the rightmost occupied site in the pile-up; though we note that if the separation is of $k-2$ holes, then no other separations of $k-2$ holes can be present in the BES, otherwise there would be an active blockage. An identical structure characterises the right-boundary pile-up, if there is one. We note that setting $d = \infty$ in the above description, we recover the structure of a BFES from Section 4.2.3. An example of a BES with $d = 4$, $k = 5$, $L = 16$, $N = 15$, $X = 67$ would be:

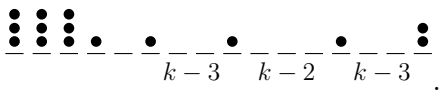

The proof that a unique BES corresponds to each (N, X) sector for finite d follows identical logic to the proof for $d = \infty$ presented in Appendix B.1, in which it is shown that a unique BFES corresponds to each (N, X) sector in a $d = \infty$ system.

We define a contracted state (CS), on the other hand, to be the particle-hole conjugate of a BES. An example of a CS with $d = 4, k = 5, L = 16, N = 29$, and $X = 258$ is given by

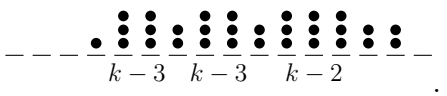

Its particle-hole conjugate can readily be shown to satisfy the definition of a BES presented above.

4.4.2 Mapping a CS to a BES

Next, we present an algorithm for mapping from a CS to a BES via a series of hopping moves for general finite d. The corresponding derivation is presented in Appendix B.5. This algorithm is central to our main algorithm for demonstrating weak fragmentation.

In what follows, we denote an outward hop gate, which sends a particle on site $i+1$ and a particle on site $j-1$ to sites i and j respectively, by $U^{+}_{i,j}$, and we denote an inward hop gate sending a pair of particles from sites i and j to sites

$i+1$ and $j-1$ by $U^{-}_{i,j}$ (with $i \leq j-2$ for both kinds of gates). A gate is only applied in the following algorithm if it is compatible with the constraints of onsite dimension d and system length L. The algorithm is given by:

- For site $i \in \{0, \ldots, L-3\}$ in increasing order, if the sites i and $i+k-1$ are within the system (i.e. are within $\{0, \ldots, L-1\}$) and both have occupancy at most $d-2$ and all sites in-between them each have occupancy $d-1$, then apply the gate $U^{+}_{i,i+k-1}$. Repeat the loop over sites until it is no longer possible to apply this gate.

- For $\ell \in \{k-4, \ldots, 0\}$ in decreasing order, for site $i \in \{0, \ldots, L-3\}$ in increasing order, if the sites i and $i+\ell+2$ are within the system and both have occupancy at most $d-2$ and all sites in-between each have occupancy $d-1$, apply the gate $U^{+}_{i,i+\ell+2}$ (where $U^{+}_{i,i+2}$ for $\ell = 0$ is an outward hop of two particles on a same site); and if the gate cannot be applied, then if the sites i and $i+\ell+3$ are within the system and both have occupancy at most $d-2$ and all sites in-between each have occupancy $d-1$, apply $U^{+}_{i,i+\ell+3}$ instead.

- For $\ell \in \{0, \ldots, k-4\}$ in increasing order, for site $i \in \{0, \ldots, L-3\}$ in increasing order, apply the gate $U^{+}_{i,i+\ell+2}$ if possible, and if not, apply the gate $U^{+}_{i,i+\ell+3}$ if possible.

For the case of $d = 2$, since no stacking can occur, ℓ ranges from $k-4$ to 1 in the second step and from 1 to $k-4$ in the third.

When the steps above are applied to a CS, the different steps have the following effects. If the CS contains a sequence of $k-2$ sites each with occupancy $d-1$, the first step of the algorithm shifts the position of that sequence towards the boundaries of the system until either that sequence is no longer present (which happens if some of the particles involved hop onto sites containing fewer than $d-2$ particles), or otherwise a boundary pile-up is obtained. Likewise, the second step of the algorithm also "unstacks" particles by shifting them toward the boundaries until no sites apart from the boundary pile-ups have occupancy greater than 1.

The third step then expands the spacings between the remaining particles not in the pile-ups until a BES is obtained.

An algorithm for mapping from the BES to the CS is obtained by replacing outward hops $U^{+}_{i,j}$ in the above algorithm with inward hops $U^{-}_{i,j}$.

It is apparent that a BES in one of the dominant symmetry sectors (which have an intensive centre of mass $\nu_X \sim 1/2$, i.e. in the middle of the system) will not have any frozen particles: all of its particles will be contained within one large active bubble devoid of frozen blockages. It is also apparent that such a BES will not contain any active blockages, as the BES-to-CS contraction algorithm involves the exchange of dipole quanta between distant regions of the chain, and such an exchange would not be possible if active blockages were present. However, for $\nu < \nu_c$, the particles in a BES cannot span the whole system, and so a BES will necessarily contain a finite density of frozen sites. For any value of d, it is only for densities $\nu \geq \nu_c$ that it is possible to construct BESs where the particles span the whole system, and hence to obtain a Krylov subspace without any blockages. In the next subsection, we use the above algorithm to show that these blockage-free Krylov subspaces dominate their symmetry sectors and the model is in its weakly fragmented phase.

4.4.3 Numerical Evidence of Weak Fragmentation

In seeking to numerically demonstrate weak fragmentation, we cannot make use of the FES picture to establish the absence of blockages, as blockages that prevent ergodicity could exist at finite d and yet not be captured by the FES picture. For example, dense groups of particles, such as a sequence of $k-1$ or more sites all containing $d-1$ particles, can potentially constitute a frozen blockage for finite-d systems, but this blockage would not be detected by the FES picture. To overcome these limitations, we develop an algorithm that, using only hopping moves compatible with finite values of d, tests for the presence of weak Hilbert space fragmentation in typical symmetry sectors for $\nu > \nu_c$.

In particular, the algorithm attempts to map from a random initial state at a given ν and L to either the corresponding BES or CS of its (N, X) symmetry sector.

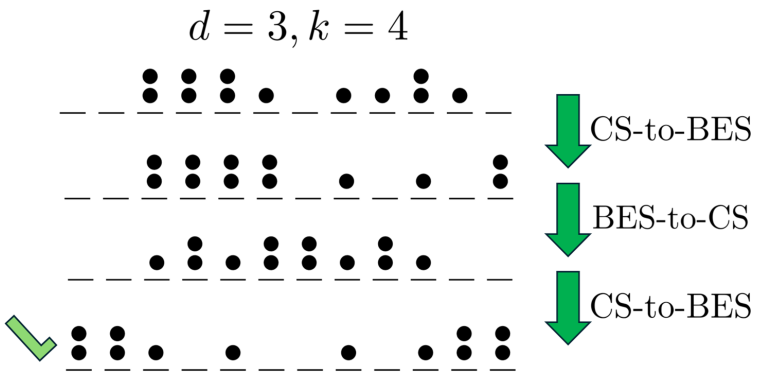

Figure 4.5: The algorithm for testing if a state shares a Krylov subspace with a BES, as applied to an arbitrary state of a $d = 3$ system with $k = 4$ range interactions. In the first step, the CS-to-BES algorithm is applied; however, as part of the expansion, a set of 4 contiguous sites on the left becomes fully occupied. This prevents further expansion. This dense region is melted in the subsequent step, where the BES-to-CS algorithm is applied. If we were to again apply the CS-to-BES algorithm (as depicted above), we would obtain a BES. In fact, the algorithm does not perform this last step: it recognises the before-last state as a CS and registers a success at that point.

The success rate of the algorithm hence lower bounds the probability that a typical initial state will be in a Krylov sector with a BES. Since there is a unique BES for each (N, X) sector, if this success rate goes to 1 (as we shall see it does for $\nu > \nu_c$), that indicates that the dominant symmetry sectors to which almost all states belong are themselves dominated by the Krylov sectors which contain a BES, and therefore that the model is in its weakly fragmented phase. For $\nu < \nu_c$ however, we expect the success rate of the algorithm to drop to 0 due to strong fragmentation.

We apply the following algorithm to an arbitrary state at a particular value of ν and L:

- Apply the CS-to-BES expansion algorithm. If a BES is obtained, terminate the algorithm and register a success; if not, proceed to the next step.
- Apply the BES-to-CS contraction algorithm. Again, register a success if a CS is obtained, and proceed to the next step if not.
- Apply the previous two steps in sequence an arbitrary number Q times in total. If the algorithm still has not terminated, then register an ambiguous result.

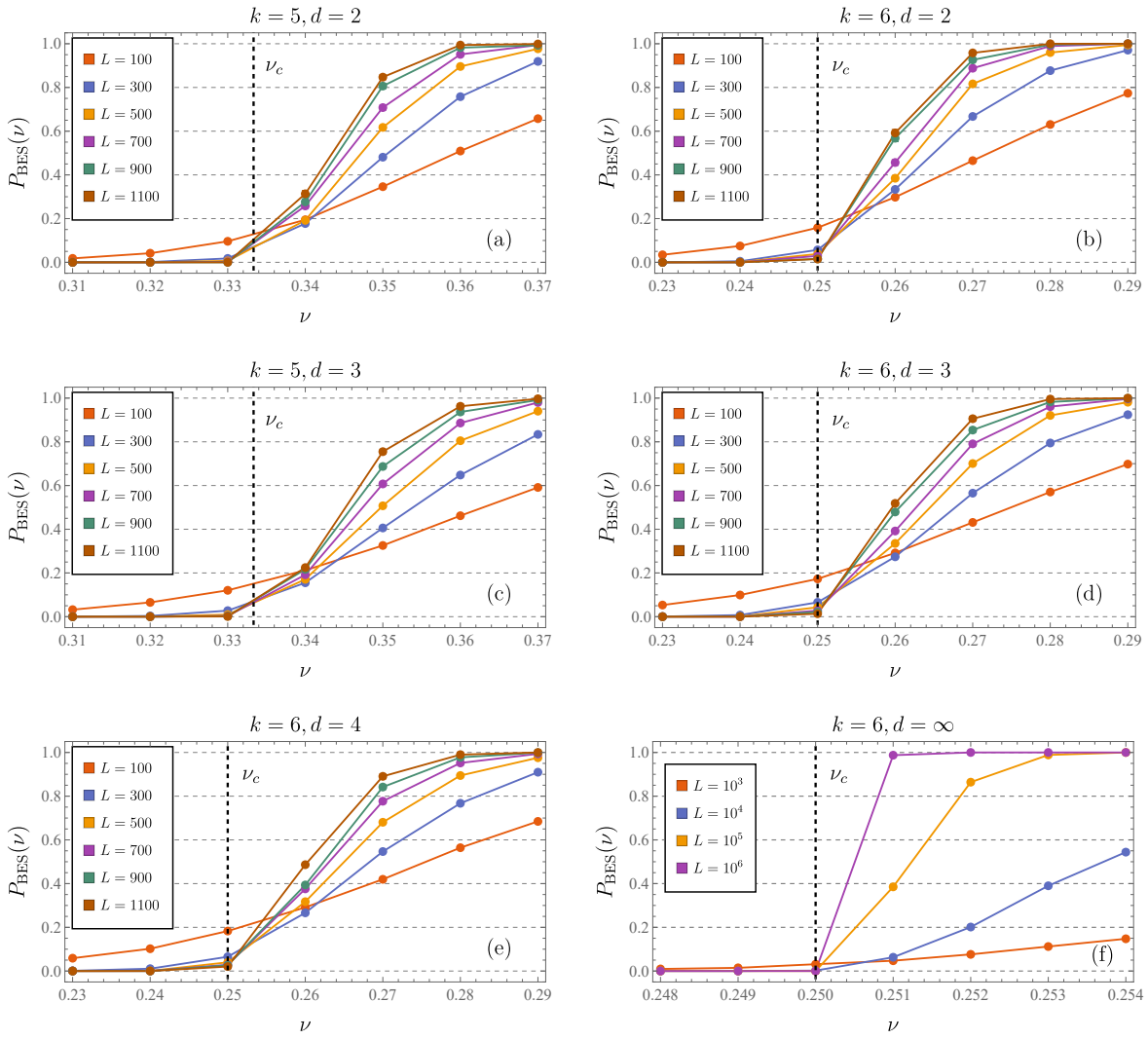

Figure 4.6: Success rate $P_{\mathrm{BES}}(\nu)$ of reaching the BES as a function of the filling ν for various choices of d and k. For plots, (a)-(e), the algorithm of Section 4.4.3 was used. Sample sizes for (a) and (b), from lowest L to highest, were 15000, 6000, 3000, 1500, 1000, and 1000. Those for (c), (d), and (e) were twice as much. For plot (f), states were mapped to their corresponding FESs, from which it was directly determined if the BFES had been reached. Sample sizes were, from lowest L to highest, 9000, 3000, 2700, and 400. The standard error, obtained by dividing the standard deviation associated with each data point by the square root of the sample size, is mostly too small to see.

In what follows, we set $Q = 4$. The rationale behind the above algorithm is as follows. After the first application of the CS-to-BES algorithm, if the state does not reach a BES, often the resulting state is found to be composed of individual sub-BESs. These will often be separated from each other by either sequences of $k-1$ or more sites containing $d-1$ particles or sequences of $k-1$ or more holes. During the subsequent BES-to-CS contraction, the sequences of $k-1$ or more sites

with $d-1$ particles are "melted" by the contraction process as their edges are peeled off, but the sequences of $k-1$ or more holes remain. These hole sequences are then potentially bridged during the following CS-to-BES expansion step, though this may introduce the presence of new dense regions of $k-1$ or more maximally occupied sites. In this alternating fashion, the aim of the algorithm is to "melt" the dense regions and "bridge" the holes separating one active region from another. We present an example of the algorithm in action in Fig. 4.5.

In Fig. 4.6(a)-(e), we present the results of applying this algorithm to randomly drawn states with various onsite dimensions d and localities k. We note that in each case studied, the success rate of the algorithm tends to 1 with increasing L for $\nu > \nu_c$, indicating the presence of weak fragmentation; whereas it progressively vanishes for $\nu < \nu_c$, which is consistent with the presence of the strongly fragmented phase.

For comparison, we also present numerical results for $d = \infty$ in Fig. 4.6(f). In this case, we map arbitrary initial states directly to their corresponding FES, as we did in Section 4.3.5; if the FES is blockage-free then we register a success, and if not then we register a failure. As such, these numerics approximate the exact probability that a state is in the same Krylov subspace as a BFES, and not just a lower bound (as is the case for finite d). As expected, we see the same overall trend of an increasing success rate for $\nu > \nu_c$ and a decreasing one for $\nu < \nu_c$, again highlighting the shared critical density for arbitrary d.

4.5 Concluding Remarks

In this chapter, we introduced a number of new approaches for characterising and studying the strongly and weakly fragmented phases of dipole-conserving 1D quantum chains with local range-k interactions. This allowed us to derive numerous new results concerning these phases and the transition between them and to develop efficient algorithms for numerically studying such models at large system sizes without relying on approximations. By mapping states in finite-d systems to their corresponding fully extended states, we demonstrated the persistence of blockages (and in particular of a finite density of frozen sites) for particle fillings

$\nu < \nu_c = (k-2)^{-1}$ for several values of d. This implied that almost all states belong to strongly fragmented symmetry sectors at these fillings. We also analytically characterised the distribution of blockages and active bubbles in this phase for $d = 2$ and $d = \infty$. For the weakly fragmented phase, we developed an efficient algorithm for general d for mapping arbitrary initial states to their corresponding blockage-free extended states at $\nu > \nu_c$. The results of our numerics indicated that almost all states belong to weakly fragmented symmetry sectors at these fillings, showing that ν_c is a universal critical filling.

Many of the topics explored in this chapter warrant further analysis. It would be useful to know more about the nature and distribution of finite-d blockages that are invisible to the FES picture in typical states, as well as to find analytic expressions for the dimensions of the various Krylov sectors at finite d. This could lead to an analytic proof that the critical density equals $\nu_c = (k-2)^{-1}$ at all d, as well as to exact results concerning the mean densities of various types of blockages and active bubbles.

Several possible generalisations of our work also present themselves. One would be investigating whether the methods introduced in this work could be applied to the case of local dipole-conserving systems in higher spatial dimensions [33, 114] as well as to fragmented systems with more complex symmetries [34, 115, 116]. Another interesting direction is to consider the inclusion of ordinary onsite and lattice symmetries, and to study their possible interplay with fragmentation. Finally, it would be useful to understand how our results on the lattice are applicable to ergodicity breaking in continuum local dipole-conserving systems [117, 118].

5

Frozen Dipole-Conserving Models

In the previous chapter, we studied a family of 1D lattice models of particles acted on by random range-k hopping gates which conserved particle number N and dipole moment X. We showed that such models undergo a phase transition between a strongly fragmented non-thermalising phase and a weakly fragmented thermalising phase as the particle density $\nu = N/L$ is tuned, where L is the system size. In particular, we showed that the critical density $\nu_c = (k-2)^{-1}$ only depends on the local range of interactions k of the model, not on the onsite Hilbert space dimension d nor on the details of the dynamics. A second weak-to-strong fragmentation transition occurs at $\nu = d - 1 - \nu_c$ by particle-hole symmetry.

We next turn our attention to special-case "frozen" models which are strongly fragmented for all values of the filling ν, and hence do not undergo a phase transition. As we shall see, the more restrictive dynamics of these models lead to greater analytic tractability, making it possible to derive a number of exact results. The work presented in this chapter is based in part on [2].

We begin in Section 5.1 by considering models with "absolute blockages", which are particular local configurations of particles or holes that, whenever they occur in a state, necessarily dynamically disconnect the regions to their right and left. Absolute blockages were introduced under the name of "bottlenecks" in [33], and were also studied under the name of "blockades" in [43]. We proceed to identify which values of d and k lead to models with absolute blockages, and show that

it is possible to exactly compute the active bubble density function for some of these models. In Section 5.2, we turn our attention to "deeply frozen" models, which we define to be models in which no hopping moves are possible and hence in which all particles are immobile. We show that by endowing the particles of these models with internal spin-1/2 degrees of freedom, we can make the models dynamically interesting as immobile particles can now interact with their neighbours. We compute how typical configurations of particles at a given filling ν are divided into dynamically disconnected "interacting islands" in deeply frozen models. We furthermore demonstrate that we can ensure a model with any finite interaction range k is deeply frozen by imposing that the model conserves certain higher-order multipole moments. We also discuss how the computed distribution of interacting islands can potentially be used to analyse related approximately fragmented models, such as a spin-1 chain with unusual entanglement signatures studied in [119].

5.1 Models With Absolute Blockages

In searching for locally interacting dipole-conserving models which are always in the strongly fragmented phase, the first step is to determine the values of the onsite Hilbert space dimension d and the range of interactions k for which the lower critical density $\nu_c = 1/(k-2)$ and the upper critical density $d-1-\nu_c$ overlap. This implies the relation

$$\frac{1}{k-2} = \frac{d-1}{2}. \tag{5.1}$$

This is satisfied for the values $d = 2$, $k = 4$ and $d = 3$, $k = 3$. The models with these parameters are particularly remarkable in that they possess "absolute blockages", which are particular local configurations of particles or holes that, whenever they occur in a state, necessarily contain a frozen blockage regardless of how the other particles in the state are arranged. Absolute blockages were first studied under the name of "bottlenecks" in Ref. [33], where it was shown that their presence necessarily dynamically disconnects the regions to their right and their left in the

chain. We discuss these absolute blockages further here, and use them to compute the exact active bubble density function for $d = 2$, $k = 4$.

5.1.1 Absolute Blockages

We begin by demonstrating with arguments similar to those in Refs. [15, 33, 43] that for $d = 2$ and $k = 4$, any sequence of 5 holes (or 5 particles by particle-hole symmetry) necessarily contains at least $k - 1 = 3$ frozen sites, making this an absolute blockage. The demonstration presented here was arrived at in collaboration with Riccardo Senese [2]. For these values of d and k, only one pair of hopping moves is consistent with particle-number and dipole-moment conservation:

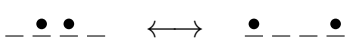

(5.2)

This restricted moveset has important implications for the mobility of particles. Indeed, say we had a particle we wished to move two sites to the right via outward hops. For it to perform its first hop, it would need a particle to its left as in the LHS of Eq. (5.2). Colouring the right particle in red and the left one in blue, the first hop would look like

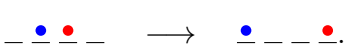

(5.3)

Hence, for the red particle to perform a second hop right, the blue particle would have to travel two sites right via outward hops first. For it to perform a first hop, there must be a particle to its left. Colouring it orange, we have

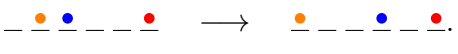

(5.4)

Thus we see for the blue particle to make a second outward hop, the orange particle would also have to do two outward hops, etc. Since this sequence never terminates, no particle can travel more than one site in a given direction via outward hops alone. Hence, whenever a sequence of 5 holes occurs in a state, the middle 3 holes must necessarily be frozen as it is impossible for a particle to hop onto them.

Thus a sequence of 5 holes (or 5 particles) constitutes an absolute blockage, as its middle 3 sites will always be a frozen blockage.

For the case of $d = 3$, $k = 3$, there is again only one pair of hopping moves available, this time given by

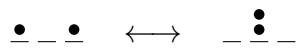

(5.5)

In this case, any sequence of 4 holes (or 4 sites with 2 particles each) will constitute an absolute blockage, with $k - 1 = 2$ frozen sites in the middle. The derivation can be found in Ref. [33], and follows very similar logic to that of the $d = 2$, $k = 4$ model presented above.

5.1.2 Exact Active Bubble Density for $d = 2$, $k = 4$

For the special case of $d = 2$ and $k = 4$, the restricted particle mobility discussed in the previous subsection makes it possible to exactly compute $\lim_{L\to\infty} A_2(x, k = 4, \nu L, L)$, which (as defined in Section 4.3.4) gives the mean density of active bubbles with x particles averaged over all possible states (i.e. particle configurations) with filling ν, interaction range $k = 4$ and dimension $d = 2$. As such, computing it exactly allows us to determine how a typical state in a thermodynamically large system with $d = 2$ and $k = 4$ is divided into active bubbles. We recall that

$$A_2(x, k, N, L) = \sum_{\ell=\ell_{2,\min}(x,k)}^{\ell_{2,\max}(x,k)} m_2(x, \ell, k) a_2(x, \ell, k, N, L), \tag{5.6}$$

where $m_2(x, \ell, k)$ gives the total number of possible active bubble configurations compatible with x particles spread over ℓ sites and $a_2(x, \ell, k, N, L)$ gives the mean density of occurrences of any active bubble configuration compatible with x, ℓ, and k averaged over all states with N particles and L holes. We shall derive an exact analytic expression for the active bubble configuration density function $\lim_{L\to\infty} a_2(x, \ell, k = 4, \nu L, L)$. We begin by noting a few simple combinatorial results.

Given ℓ contiguous sites in a randomly chosen state of a $d = 2$ system with size L and N particles, the probability that those ℓ sites contain any particular

configuration of x particles is given by

$$\binom{L-\ell}{N-x} \Big/ \binom{L}{N}, \tag{5.7}$$

where the numerator gives the number of ways of constructing a state where those ℓ sites contain that configuration of x particles, and the denominator gives the total number of possible states in the N sector. We note this result is independent of the exact arrangement of the x particles in the configuration. Thus, for example, both particle configurations presented in Eq. (5.2) could occur on a given set of 4 contiguous sites in a random state with equal probability.

Setting $N = \nu L$ and taking the thermodynamic limit, Eq. (5.7) simplifies to

$$\nu^x (1-\nu)^{\ell - x}, \tag{5.8}$$

up to $\mathcal{O}(1/L)$ corrections. Thus a given configuration of x particles over ℓ sites occurs on average $L\nu^x(1-\nu)^{\ell-x}$ times in a random state. Hence, by self-averaging [113], Eq. (5.8) also equals the exact density of occurrences of the particle configuration in question in a typical thermodynamically large state. This has important consequences for the dynamics of the system: in particular, it implies the presence of a finite density of absolute blockages in any typical state, guaranteeing the presence of a finite density of frozen sites, and hence of strong fragmentation at any filling ν.

We shall now use the result in Eq. (5.8) to compute the active bubble configuration density function $a_2(x, \ell, k = 4, \nu L, L)$ in the thermodynamic limit. It is clear from the above discussion that this function must be of the general form

$$\lim_{L\to\infty} a_2(x, \ell, k = 4, \nu L, L) = \nu^x (1-\nu)^{\ell-x} (P_{\mathrm{b}}(\nu))^2,$$

where the function $P_{\mathrm{b}}(\nu)$ is the probability that the particles on a given side of the active bubble configuration, either to its right or to its left, are arranged so as to form a frozen blockage consisting of 3 or more frozen sites. By the restricted mobility derived in Section 5.1.1, the simplest way for this to happen would be if there was a sequence of 4 holes or 4 particles next to the active bubble, resulting in the lower bound

$$P_{\mathrm{b}}(\nu) > \nu^4 + (1-\nu)^4.$$

In Appendix B.6, we make use of the restricted particle mobility to exactly enumerate all possible patterns of particles and holes which result in a frozen blockage of 3 frozen sites next to an active bubble, giving the final result

$$\begin{aligned} P_{\mathrm{b}}(\nu) = \\ (1-\nu)^3 \frac{1-2\nu+2\nu^2-\nu^3+\nu^4}{1-2\nu+3\nu^2-3\nu^3+4\nu^4-3\nu^5+\nu^6} \\ + (\nu \leftrightarrow 1-\nu) \end{aligned} \tag{5.9}$$

Using this result, we may exactly calculate $\lim_{L\to\infty} A_2(x, k=4, \nu L, L)$ by determining the multiplicity function $m_2(x, \ell, k)$ on a case-by-case basis. For example, for $x = 2$, only two active bubble configurations are possible in $k = 4$, both of which occupy 4 sites by Eq. (5.2). Referring to Eq. (5.6), this immediately gives

$$\begin{aligned} \lim_{L\to\infty} A_2(x=2, &k=4, \nu L, L) \\ &= 2\nu^2(1-\nu)^2(P_{\mathrm{b}}(\nu))^2. \end{aligned} \tag{5.10}$$

The densities of active bubbles with higher values of x can be computed similarly.

5.2 Deeply Frozen Models

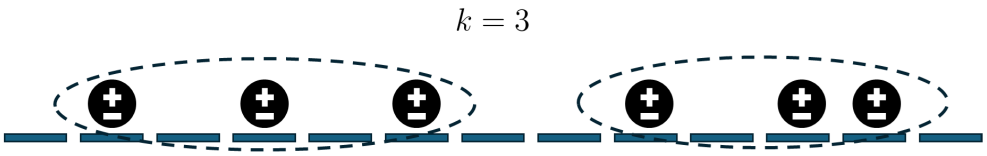

Figure 5.1: A deeply frozen model with $d = 2$, $k = 3$. We endow each particle with a spin-1/2 internal degree of freedom, such that if two particles are next to each other or separated by at most $k - 2 = 1$ site, then they can interact. The particles in a given particle configuration can then be divided into "interacting islands", made up of groups of particles separated by $k - 2$ sites or fewer from each other. This is depicted in the above image. Each interacting island thus forms its own independent closed 1D system.

We showed in Chapter 4 how the strongly fragmented phase of locally interacting dipole-conserving chains can be characterised by the presence of a finite density of blockages (and in particular of frozen blockages) in typical states at $\nu < \nu_c$, and how the weakly fragmented phase can be characterised by the absence of blockages in typical states. We also showed in Section 5.1 that for certain values of k and d, the model is strongly fragmented at all fillings ν, with a finite density of frozen

blockages present throughout. There is a third region of the phase diagram in Fig. 4.1 we have not yet discussed, which we shall refer to as the "deeply frozen" region. This region consists of $k = 2$ for any d and $k = 3$ for $d = 2$. In the deeply frozen region, there are no hopping moves compatible with range-k interactions and particle-number and dipole-moment conservation, and hence the particles are immobile. Although it may seem that the dynamics of the deeply frozen region are trivial, we can make deeply frozen models dynamically interesting by endowing the particles with spin-1/2 internal degrees of freedom, such that they can still interact with each other. The particles within a state of a deeply frozen model can then be divided into "interacting islands" depending on which other particles they interact with. We depict an example of interacting islands in Fig. 5.1. Interacting islands are conceptually very similar to the active bubbles discussed in Section 4.3.4, with the former being composed of particles interacting via their internal spin and the latter of particles interacting via hopping moves.

In Section 5.2.1, we introduce deeply frozen models in more detail, and derive several exact results concerning the interacting-island distribution. In Section 5.2.2, we discuss how imposing the conservation of higher-order multipole laws can impact deeply frozen models, and make the deeply frozen region persist to higher values of k. In Section 5.2.3, we discuss perturbations of deeply frozen models.

5.2.1 Deeply Frozen Models and Interacting Islands

We shall be focusing on deeply frozen models with at most one particle per site ($d = 2$) and periodic boundary conditions, which simplifies many of the calculations. Each of the immobile particles in the system will have an internal spin-1/2 degree of freedom, through which they can interact with other particles separated from them by $k - 2$ sites or fewer. We also no longer focus on random circuit models, but rather "static" deeply frozen range-k Hamiltonians of the general form

$$H = \sum_{i=1}^{L} J_i h_{i,i+k-1}, \tag{5.11}$$

where the J_i are arbitrary coefficients, and each $h_{i,i+k-1}$ acts purely on the internal degrees of freedom of particles situated on the sites i to $i+k-1$ inclusively. The $h_{i,i+k-1}$ for different values of i need not have the same form. Many of our results, however, also directly hold for random circuits as well.

An example of a deeply frozen model with $k = 2$ can be found in Section 2.3.1. In this case, H is a spin-1 model, with possible spin values $\{+, 0, -\}$ on each site. The interaction terms $h_{i,i+1}$ consist of XYZ-chain interactions acting on the spin-1/2 subspaces $\{+, -\}$ of each site; hence, sites with onsite spin 0 are like "empty" sites. Describing our deeply frozen models in terms on spin-1 Hamiltonians will come in handy in Section 5.2.3, where we consider perturbations to these models.

Returning to the more general case of a range-k deeply frozen model, we now seek to analytically determine how on average a given random configuration of particles in such a model at a filling ν will be divided into interacting islands of different sizes. We define an interacting island to be made up of a group of particles such that each particle is separated by at most $k-2$ holes from its neighbours in the island, and such that there are at least $k-1$ holes both on the right and left sides of the island. Hence, each interacting island forms its own closed system under the model's range-k dynamics. We recall that an example of interacting islands for $k = 3$ was provided in Fig. 5.1.

We shall next exactly compute the particle distribution function $P_I(x, N, k, L)$, which gives the average percentage of particles in a random state at filling $\nu = N/L$ that are situated in interacting islands containing x particles in total. Hence, $P_I(1, N, k, L)$ gives the average percentage of particles that are on their own and hence not interacting, $P_I(2, N, k, L)$ gives the percentage of particles that are paired up in islands with 2 particles total, and so on. It is clear that

$$\sum_{x=1}^{\infty} P_I(x, N, k, L) = 1, \tag{5.12}$$

since all particles must belong to an interacting island of some size and we do not expect any extensively large islands in a typical state. The particle distribution

function can be computed explicitly as

$$P_I(x,N,k,L) = \frac{x}{N}\frac{\mathscr{I}(x,N,k,L)}{\binom{L}{N}}, \tag{5.13}$$

where the function $\mathscr{I}(x,N,k,L)$ gives the total number of occurrences of islands with x particles across all possible particle arrangements for a given N, L, and k. Same as in previous scenarios, we expect $P_I(x,N,k,L)$ to also give the exact density of islands with x particles in typical states in the thermodynamic limit by self-averaging [113].

For finite L, the function $\mathscr{I}(x,N,k,L)$ sometimes contains summations that cannot be performed exactly. We provide expressions for $\mathscr{I}(x,N,k,L)$ at finite L in Appendix B.7. Setting $N=\nu L$ and taking the thermodynamic limit, however, makes it possible to compute $P_I(x,N,k,L)$ exactly. We begin by noting that, for $x<N$ and periodic boundaries, we have that

$$\mathscr{I}(x,N,k,L)\Big|_{x<N} = L\ \mathscr{I}_1(x,N,k,L), \tag{5.14}$$

where $\mathscr{I}_1(x,N,k,L)$ is the total number of states with N particles and L sites for which there is an island containing x particles with the leftmost particle of the island being situated on site 1. $\mathscr{I}_1(x,N,k,L)$ is simply computed by summing all possible ways to construct an island with x particles starting on site 1 times all possible ways to arrange the remaining $N-x$ particles in the state. For very large L, we then have that

$$\begin{aligned}\mathscr{I}(x,N,k,L)\Big|_{x\ll N,L} = L \sum_{n_1=0}^{x-1}\ \sum_{n_2=0}^{x-1-n_1}\ \cdots\ \sum_{n_{k-2}=0}^{x-1-\sum_{i=1}^{k-3} n_i} \\ \left(\binom{x-1}{n_1}\binom{x-1-n_1}{n_2}\cdots\binom{x-1-\sum_{i=1}^{k-3} n_i}{n_{k-2}}\right)\binom{L-x-2(k-1)-\sum_{i=1}^{k-1} i n_i}{N-x}\end{aligned} \tag{5.15}$$

The variables $n_1,\ldots,n_{k-2}$ summed over in the above expression constitute the number of pairs of particles in the island that are respectively separated by 1 hole, 2 holes, and so forth up to $k-2$ holes. The rightmost binomial computes all possible ways to arrange the particles outside the island such that there are at least $k-1$ holes on either side of the island, and the other binomials count the

number of ways to arrange the sequences of n_1 individual holes, n_2 pairs of holes, and so on between the particles in the island.

Setting $N = \nu L$ and taking the thermodynamic limit, we find that

$$\frac{L\binom{L-x-2(k-1)-\sum_{i=1}^{k-2} in_i}{\nu L-x}}{\nu L\binom{L}{\nu L}} \xrightarrow{L\to\infty} \nu^{x-1}(1-\nu)^{2(k-1)+\sum_{i=1}^{k-2} in_i}. \tag{5.16}$$

And so, defining $P_I(x,\nu,k) = \lim_{L\to\infty} P_I(x,\nu L,k,L)$, we have that

$$P_I(x,\nu,k) = x\,\nu^{x-1}(1-\nu)^{2(k-1)} \sum_{n_1=0}^{x-1} \sum_{n_2=0}^{x-1-n_1} \cdots \sum_{n_{k-2}=0}^{x-1-\sum_{i=1}^{k-3} n_i} \left(\binom{x-1}{n_1}\binom{x-1-n_1}{n_2}\cdots\binom{x-1-\sum_{i=1}^{k-3} n_i}{n_{k-2}}\right)(1-\nu)^{\sum_{i=1}^{k-1} in_i}. \tag{5.17}$$

Our next task consists of performing the summation above. We make use of the following identity stemming from the binomial theorem:

$$\sum_{n=0}^{N}\binom{N}{n}z^n = (1+z)^N \tag{5.18}$$

The inductive step is then as follows, with j starting at $k-2$ and decreasing by 1 at each step until it reaches 1:

$$\begin{aligned}
&\sum_{n_j=0}^{x-1-\sum_{i=1}^{j-1} n_i}\binom{x-1-\sum_{i=1}^{j-1} n_i}{n_j}(1-\nu)^{jn_j}\left(1+\sum_{\ell=j+1}^{k-2}(1-\nu)^\ell\right)^{-n_j+x-1-\sum_{i=1}^{j-1} n_i} \\
&= \left(1+\sum_{\ell=j+1}^{k-2}(1-\nu)^\ell\right)^{x-1-\sum_{i=1}^{j-1} n_i}\sum_{n_j=0}^{x-1-\sum_{i=1}^{j-1} n_i}\binom{x-1-\sum_{i=1}^{j-1} n_i}{n_j}\left(\frac{(1-\nu)^j}{1+\sum_{\ell=j+1}^{k-2}(1-\nu)^\ell}\right)^{n_j} \\
&= \left(1+\sum_{\ell=j+1}^{k-2}(1-\nu)^\ell\right)^{x-1-\sum_{i=1}^{j-1} n_i}\left(1+\frac{(1-\nu)^j}{1+\sum_{\ell=j+1}^{k-2}(1-\nu)^\ell}\right)^{x-1-\sum_{i=1}^{j-1} n_i} \\
&= \left(1+\sum_{\ell=j}^{k-2}(1-\nu)^\ell\right)^{x-1-\sum_{i=1}^{j-1} n_i}
\end{aligned} \tag{5.19}$$

After the final step at $j = 1$, we obtain:

$$\left(1+\sum_{\ell=1}^{k-2}(1-\nu)^\ell\right)^{x-1} = \left(1+\frac{(1-\nu)-(1-\nu)^{k-1}}{\nu}\right)^{x-1} = \nu^{-(x-1)}(1-(1-\nu)^{k-1})^{x-1} \tag{5.20}$$

And so:

$$P_I(x,\nu,k) = x(1-\nu)^{2(k-1)}\left(1-(1-\nu)^{k-1}\right)^{x-1} \tag{5.21}$$

It is simple to check this distribution function sums to 1, indicating that in a typical state almost all particles belong to finite-sized interacting islands, and that its mean and variance are given by

$$\mu(\nu,k)=\sum_{x=1}^{\infty}xP_I(x,\nu,k)=-1+2(1-\nu)^{-(k-1)}, \tag{5.22}$$

$$\sigma^2(\nu,k)=\sum_{x=1}^{\infty}(x-\mu_f)^2P_I(x,\nu,k)=2(1-\nu)^{-2(k-1)}(1-(1-\nu)^{k-1}). \tag{5.23}$$

By self-averaging, the island distribution function Eq. (5.21) also applies to individual states in the thermodynamic limit: the density of interacting islands of different sizes x is exactly given in almost all states by the distribution in Eq. (5.21). Thus, given a random state at a filling ν, we already know with a high level of certainty how many particles are isolated in $x=1$ islands, how many are paired off in $x=2$ islands, and so on. Hence, a high level of analytic control can be acquired in deeply frozen models concerning the interacting structure of typical states.

5.2.2 Multipole Conservation

As previously established, for onsite Hilbert space dimension $d=2$, if the interaction range satisfies $k\leq 3$, then there are no hopping moves that are compatible with dipole-moment conservation and the model is deeply frozen. In this subsection, we establish that conserving higher-order multipole moments can ensure that models with higher values of k are deeply frozen too.

The general multipole moments $\mathcal{Q}_\ell$ are given by

$$\mathcal{Q}_\ell=\sum_{i=1}^{L}i^\ell n_i, \tag{5.24}$$

with $\ell\geq 0$ and n_i giving the number of particles on site i. We see that $\mathcal{Q}_0=N$ and $\mathcal{Q}_1=X$. Let us define a function $k_{\max}(\ell)$ which, for $\ell\in\mathbb{N}^0$, indicates what the highest value of the interaction range k is such that a range-k Hamiltonian with all multipole moments from $\mathcal{Q}_0$ to $\mathcal{Q}_\ell$ conserved is necessarily deeply frozen. We next derive a lower bound on $k_{\max}(\ell)$. Consider a quantum state $|\psi\rangle$ within a quantum number sector of the $\ell+1$ multipole charges. Since the multipole charges commute with each range-k term $h_{i,i+k-1}$ in the Hamiltonian Eq. (5.11) individually, then

the $h_{i,i+k-1}$ locally conserve each multipole moment as well. Let $X^m_{i,i+k-1}$ denote the local multipole moment associated with the multipole operator $\mathcal{Q}_m$ acting on sites $\{i, i+1, \ldots, i+k-1\}$ of the state $|\psi\rangle$. We obtain the series of equations:

$$\left\{ \sum_{j=i}^{i+k-1} j^m n_j \, |\psi\rangle = X^m_{i,i+k-1} \, |\psi\rangle \right\}_{m=0}^{\ell} \tag{5.25}$$

This provides us with $\ell + 1$ linearly independent equations. Hence, if $k \leq \ell + 1$, then the eigenvalue of each onsite particle number operator n_j acting on $|\psi\rangle$ is uniquely determined by the quantum numbers $Q^m_{i,i+k-1}$ of the multipole symmetries. Thus each n_j is individually conserved, and we have established that

$$k_{\max}(\ell) \geq \ell + 1. \tag{5.26}$$

We have thus guaranteed that by imposing conservation of sufficiently high multipole moments, we can obtain a deeply frozen model for any value of k. In fact, the true value of $k_{\max}(\ell)$ for a given ℓ is typically much higher than the lower bound provided above. This is because the n_j have discrete eigenvalues of 0 and 1. Therefore even if $k > \ell+1$, this additional discreteness constraint can still be enough to determine each n_j from a set of local moments $X^m_{i,i+k-1}$. One can numerically find the first few values of $k_{\max}(\ell)$ by searching for the lowest value of k at which a hopping move compatible with the conservation laws is found. One obtains:

$$k_{\max}(0) = 1,\ k_{\max}(1) = 3,\ k_{\max}(2) = 6,\ k_{\max}(3) = 11,\ k_{\max}(4) = 15,\ k_{\max}(5) = 22.$$

Hence, a small number of conservation laws can greatly impede mobility for a significant range of interaction localities.

5.2.3 Perturbing Deeply Frozen Models

A topic of interest concerning Hilbert space fragmentation has been the study of Hamiltonians which are closely related to fragmented models, e.g. via perturbation theory or a Schrieffer–Wolff transformation [120–124]. Such Hamiltonians can still exhibit signatures of fragmentation, such as low entanglement entropy and signs of localisation. In our case, the study of perturbations of deeply frozen models

could be relevant to understanding the unusual entanglement-entropy spreading observed in a disordered spin chain studied in [119]. The model in question is a spin-1 Hamiltonian whose general structure is given by

$$H = \lambda \left(\sum_{i=1}^{L} J_i (S_i^z)^2 \right) + a\, H_{1/2}^{XX} + b\, H_{\text{th}}, \tag{5.27}$$

where λ, a, and b are parameters that can be tuned, the J_i are random coefficients drawn from a normal distribution with mean 0 and standard deviation 1, H_{th} is a thermalising term, and $H_{1/2}^{XX}$ is a spin-1/2 XX chain Hamiltonian which only acts on sites with onsite spin + or − (and not spin 0). In particular, in terms of the spin-1 raising and lowering operators S_i^+ and S_i^-, we have that

$$H_{1/2}^{XX} = \sum_{i=1}^{L} (S_i^+)^2 (S_{i+1}^-)^2 + (S_i^-)^2 (S_{i+1}^+)^2. \tag{5.28}$$

One of the questions the authors of [119] studied was how the cut-averaged entanglement entropy (CAEE) evolved as the disorder strength λ was varied for fixed values of a and b with $a \approx 2b$. The CAEE associated with a given subsystem size is obtained by computing the von Neumann entanglement entropy for every possible location of a subsystem of that size within the spin chain, then averaging over the results. For the disorder-free case of $\lambda = 0$, the CAEE was found in [119] to scale as a volume law with increasing subsystem size. For large $\lambda \approx 80b$, on the other hand, a spread of many different of CAEE scalings was observed, which is reminiscent of the scalings observed in fragmented models [32].

Using the results derived in Section 5.2.1, we can provide an explanation for the unusual entanglement signatures observed in [119]. In particular, we note that if we set the coefficient $b = 0$, the Hamiltonian

$$H\Big|_{b=0} = \lambda \left(\sum_{i=1}^{L} J_i (S_i^z)^2 \right) + a\, H_{1/2}^{XX} \tag{5.29}$$

is a deeply frozen model with interaction range $k = 2$. Hence, the eigenstates of $H\Big|_{b=0}$ are composed of several "interacting islands", each of which forms its own separate spin-1/2 system acted on by $H_{1/2}^{XX}$. The disordered $\sum_{i=1}^{L} J_i (S_i^z)^2$ term then has the effect of splitting the degeneracies between eigenstates with similar island configurations.

Thus, we can make use of the island distribution function $P_I(x, \nu, k)$ presented in Eq. (5.21) to determine how typical eigenstates are divided into interacting islands. In particular, setting

$$\nu = \frac{1}{L}\sum_{i=1}^{L}(S_i^z)^2, \tag{5.30}$$

then for a typical eigenstate in a thermodynamically large system at a given ν, we can determine from $P_I(x, \nu, k)$ exactly what percentage of sites with onsite spins in $\{+, -\}$ are in islands of different sizes. Those sites in islands of size $x = 1$ will not contribute to the dynamics; those in islands of size $x = 2$ or greater will. The eigenvalue associated with a given eigenstate is the sum of the eigenvalues each interacting island in the eigenstate takes on under $H\Big|_{b=0}$. Hence, the distribution $P_I(x, \nu, k)$ can lead to predictions concerning the eigenvalues of typical eigenstates, as well as concerning their CAEE (which can be determined by averaging over the CAEE of the finite-sized interacting islands).

Returning to the case of nonzero b, we now see that the full Hamiltonian in Eq. (5.27) is a perturbation of the deeply frozen Hamiltonian $H\Big|_{b=0}$. The spread of CAEE scalings shown in Eq. (5.27) therefore suggests that, for $b \ll \lambda$, some of the interacting island structure of the deeply frozen model survives the perturbation. The different CAEE scalings might therefore arise due to the presence of "approximate" interacting islands of different sizes. It would be good to determine more precisely the nature of this approximate island structure and if it continues to be present when larger values of L are considered. If so, one could use the interacting island distribution $P_I(x, \nu, k)$ to make predictions about the spectrum and dynamical evolution of the perturbed model. This could prove beneficial for the study of thermodynamically large states, as they could be divided into finite-sized "approximate islands", making them more tractable for analysis. Future research will hopefully clarify this.

5.3 Concluding Remarks

In this chapter, we studied a variety of "frozen" locally interacting dipole-conserving models which are strongly fragmented at all particle fillings ν. We showed how dipole-conserving models with onsite Hilbert space dimension d and interaction range k satisfying $d = 2$, $k = 4$ or $d = 3$, $k = 3$ have absolute restrictions on how far particles can travel from their point of origin, leading to the presence of local absolute blockages which dynamically disconnect the regions to their left and right. We then made further use of this restricted mobility to exactly compute the active bubble distribution function for $d = 2$, $k = 4$. The dipole-conserving model with $d = 2$, $k = 4$ has previously been studied in depth in [43, 109], where the authors thoroughly analysed the properties of several of its Krylov subspaces. It would be interesting to see if our results can shed further light on their results. It would also be interesting to determine if analytic results could be derived for $d = 3$, $k = 3$, and if so, what their implications would be for the spin-1 chains studied in [32, 33].

We furthermore explored the properties of deeply frozen models, where the particles are immobile but can interact via spin-1/2 internal degrees of freedom. We exactly computed the interacting island distribution function associated with these models, and showed how imposing the conservation of higher-order multipole moments makes it possible to obtain deeply frozen models with any finite interaction range k. We also discussed how the analysis of deeply frozen models may prove useful to the study of related approximately fragmented models, such as the one studied in [119]. This opens up an interesting area for further exploration. In particular, if there is a significant prethermal timescale during which the approximately fragmented models can be considered to be made of interacting islands, then the interacting island distribution could be used to predict the dynamical evolution of thermodynamically large states by splitting them into numerically tractable finite-sized islands. The next steps in exploring these models would therefore be testing the extent to which the analytic results derived match up with the results of numerical simulations of related approximately fragmented models.

6
Summary and Outlook

In this thesis, we studied two examples of Hilbert-space-fragmented models, one exhibiting quantum fragmentation and the other classical fragmentation.

The quantum-fragmented system is a disordered SU(M)-symmetric spin model constituting a long-range generalisation of Temperley-Lieb spin chains. Its fragmentation stems from its exponentially growing nullspace, and its commutant algebra is a subalgebra of the Read-Saleur algebra [78]. We derived many of this model's properties exactly, providing a complete characterisation of its nullspace and showing that some of its SU(M) symmetry sectors are strongly fragmented. We also discussed various perturbations to the model, including ones which transformed some of its nullstates into quantum many-body scars. The rarity of fragmented non-local models in the literature make this model of particular interest.

The classically fragmented system is a well-known 1D lattice model of hopping particles with local range-k interactions which conserve particle number and dipole moment. We developed a powerful approach to analysing this model in terms of "fully extended states" and "blockages". This allowed us to derive several new results for the model's strongly fragmented phase. These included restrictions on particle mobility as well as lower bounds on the mean densities of frozen sites and on those of differently sized active bubbles. It also led to an efficient algorithm for identifying the onset of the weakly fragmented phase by modeling the system's hopping dynamics. These results led us to conclude that the model possesses a universal critical particle

density of $\nu_c = (k-2)^{-1}$ which is independent of the onsite Hilbert space dimension as well as of the details of the dynamics. We furthermore investigated special-case "frozen" models which are strongly fragmented for all particle fillings.

Throughout this thesis, we have highlighted several open questions and possible future research directions. One notable direction is the continued search for non-local models that are Hilbert-space-fragmented. As previously noted, examples of such models are scarce, as the commutant algebras of non-local models are heavily restricted by their large bond algebras. For the non-local model studied in this thesis, it is particularly surprising that a non-trivial commutant survives the generalisation to long-range interactions because this generalisation destroys much of the algebraic structure of the model's nearest-neighbour counterpart. A broader understanding of which local models remain fragmented after the inclusion of all-to-all interactions and which ones do not could provide valuable insights concerning the general algebraic structures of fragmentation in non-local systems.

Another fruitful direction would be to investigate what further results can be derived using fully extended states in locally interacting dipole-conserving chains. In this thesis, the employment of fully extended states has led to a high degree of analytical control over the ergodicity-restoring phase transition such models undergo, a control which is lacking in ergodicity transitions in other settings such as many-body localised models. The fully extended state picture we developed could yield insights concerning critical exponents, and might lead to a rigorous proof for the value of ν_c. It would also be interesting to see if the approaches developed here can be applied to locally interacting dipole-conserving systems with higher spatial dimensions or to models with related fragmentation structures.

Through the results derived in this thesis, we have not only broken ground concerning the study of fragmentation in non-local models, but also revealed surprising new results concerning fragmentation in the paradigmatic example of locally interacting dipole-conserving chains. We hope these will serve as productive starting points for further investigations into these rich topics, leading to a fuller understanding of Hilbert space fragmentation and its role in violations of ergodicity.

A

Appendices for Chapter 3

A.1 Constructing the Nullspace for $M = 3$

In this appendix, we show how to construct a basis which spans a significant fraction of the nullspace of H_M for $M = 3$. The number of linearly independent states provided by this construction grows as $2^N N^2$, accounting for approximately half of the total nullspace dimension of $\frac{9}{4}2^N N^2$ from Eq. (3.33).

Our basis states are constructed by applying SU(3) ladder operators to the product states $|\psi_{\mathcal{N}}\rangle$ described in Eq. (3.8). We use the following two ladder operators:

$$I^+ = \sum_{i=1}^{N} (|3\rangle\langle 2|)^i - \sum_{j=1}^{N} (|2\rangle\langle 3|)_j,$$
$$V^+ = \sum_{i=1}^{N} (|3\rangle\langle 1|)^i - \sum_{j=1}^{N} (|1\rangle\langle 3|)_j$$

The operators with raised i indices act on the **3** irrep spins, and those with lowered j indices act on the $\overline{\mathbf{3}}$ irrep spins.

We write our starting product state explicitly as factored into its components on the **3** irrep and $\overline{\mathbf{3}}$ irrep spins:

$$|\psi_{\mathcal{T}}\rangle = \left|\psi_{\mathcal{N}}^{\mathbf{3}}\right\rangle \otimes \left|\psi_{\mathcal{N}}^{\overline{\mathbf{3}}}\right\rangle.$$

Say we choose n of the spins t^i in $|\psi_{\mathcal{N}}^{\mathbf{3}}\rangle$ to be at level 2 and set the remaining $N - n$ spins to be at level 1, and set all spins s_j in $\left|\psi_{\mathcal{N}}^{\overline{\mathbf{3}}}\right\rangle$ to be at level 3. There are $\binom{N}{n}$ ways to arrange the spins at level 2 in $|\psi_{\mathcal{N}}^{\mathbf{3}}\rangle$. For each of these, the operator

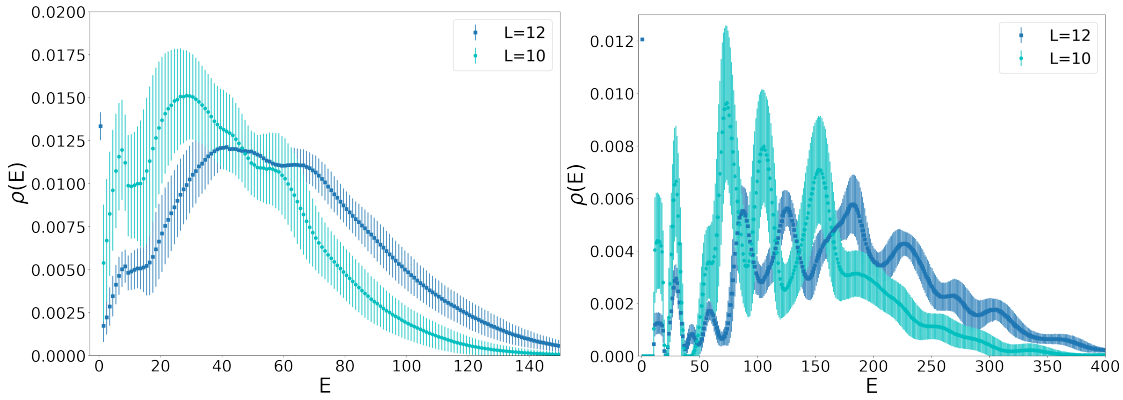

(a) **(b)**

Figure A.1: Densities of states for H_M (3.5) for $M = 3$, with coefficients r_j^i drawn from the uniform distribution [0,10] for subfigure (a) and the uniform distribution [10,20] for subfigure (b). 10000 disorder samples were averaged over for system size $2N = 10$ and 1000 samples for system size $2N = 12$. The results have been binned with bin width 1. For $2N = 10$, the density of states at $E = 0$ is outside of the vertical range of both plots: it is $\rho(0) = 0.042 \pm 0.003$ for $2N = 10$ in (a) and $\rho(0) = 0.03807\ldots$ (exact value) for $2N = 12$ in (b). Error bars represent the standard deviation; the standard error, obtained by dividing by the square root of sample size, would be too small to see.

I^+ can be applied at least N times before it annihilates the overall state. Say it is applied p times, with $0 \leq p \leq N$: then V^+ can be applied up to $2N - n - p$ times before it annihilates the state. This yields in total $\sum_{p=0}^{N}(2N - n - p + 1)$ nullspace states for each initial configuration of the n spins at level 2 in $|\psi_{\mathcal{N}}^{\mathbf{3}}\rangle$. It is straightforward to check that all of the obtained states are linearly independent. The total number of nullspace states obtained this way is

$$\sum_{n,p=0}^{N} \binom{N}{n}(2N - n - p + 1) = 2^N(N+1)^2 \sim 2^N N^2,$$

from which we find that our constructed nullspace states form a basis spanning approximately half of the nullspace.

A.2 Numerical Density of States for $M = 3$

We present some plots of the binned density of states (DOS) of H_M (3.5) for $M = 3$ with various probability distributions for the random coefficients r_j^i.

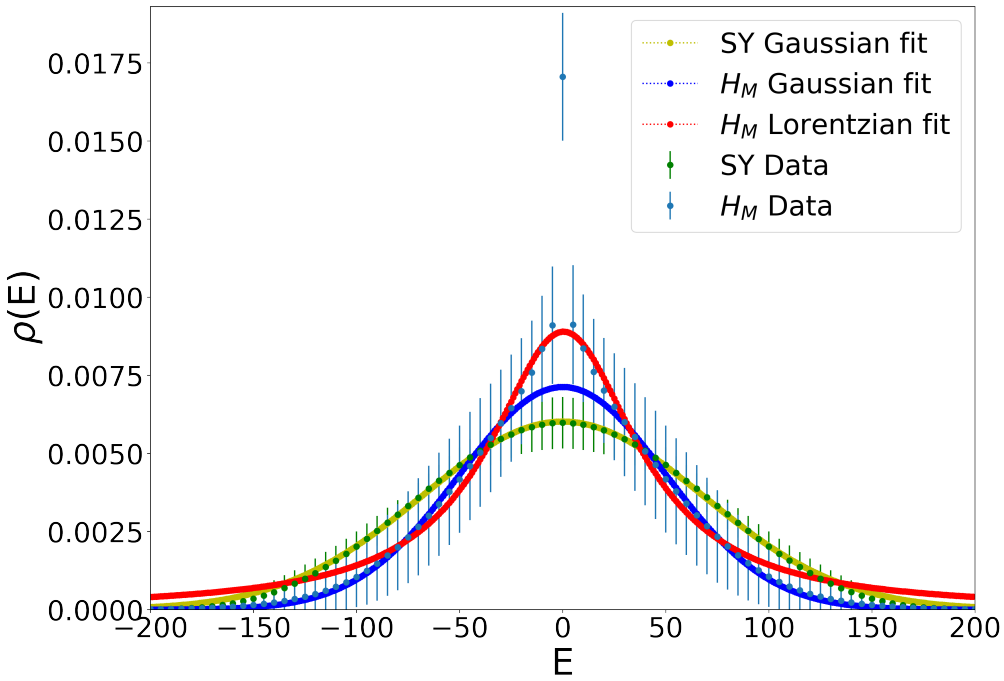

Figure A.2: Density of states for H_M and for the SY model for $2N = 10, M = 3$, and with all sites in the SY model transforming in the **M** irrep. The coefficients were drawn from a Gaussian distribution with mean 0 and standard deviation 10, and a normalisation factor of $1/\sqrt{3*5}$ was applied to both Hamiltonians (as in Eqs. (3.13)). 10000 disorder samples were averaged over for both curves and the results were binned with bin width 5. The Gaussian fit for the SY model follows $\rho(E) = a\exp\{-(E-E_0)^2/2\sigma^2\}$ with parameters $a = 0.00602 \pm 0.00001$, $E_0 = 0.00 \pm 0.04$, and $\sigma = 17.55 \pm 0.04$. The Gaussian fit for H_M was applied to energies $|E| \geq 13$, and has parameters $a = 0.00649 \pm 0.00003$, $E_0 = 0.03 \pm 0.02$, and $\sigma = 13.59 \pm 0.04$. The Lorentzian fit of H_M was applied to energies $|E| \leq 20$ (excluding $E = 0$) and follows $\rho(E) = a\Gamma^2/(\Gamma^2 + (E-E_0)^2)$ with parameters $a = 0.00710 \pm 0.00005$, $E_0 = 0.01 \pm 0.06$, and $\Gamma = 12.98 \pm 0.08$. Error bars again represent the standard deviation, with the standard error being too small to see.

In Fig. A.1a, we give the averaged density of states of H_M for system sizes $2N = 10$ and $2N = 12$, with the random coefficients r_j^i drawn from the uniform distribution [0,10]. We note the singularity at $E = 0$ due to the large ground state degeneracy, and the smoothing out of the profile of the DOS function with increasing N. In Fig. A.1b, the coefficients r_j^i are instead drawn from the uniform distribution [10,20]. The density of states now features several sharp oscillations. Based on similar oscillations observed in the SYK model [125], these oscillations may be due to level repulsion originating from the disordered nature of the system, and may then smooth out for large N. We also note the appearance of a gap between 0 and 10, as opposed to Fig. A.1a where no gap is visible.

In Fig. A.2, we consider a Gaussian distribution for the coefficients r^i_j, with mean 0, standard deviation 10, and a normalisation factor of $1/\sqrt{3*5}$ in front of the Hamiltonian (as is done with the SY model in Eq. (3.13)). We set the system size to $2N = 10$. With this choice of distribution for the r^i_j, the highly degenerate nullspace is situated in the middle of the spectrum, and the resulting singularity is visible at energy 0. For comparison, the DOS of the SY model with all sites in the fundamental $\mathbf{M}$ irrep is also presented in the same plot, with coefficients g^{ij} drawn from the same Gaussian distribution as the coefficients r^i_j in H_M. The DOS of the SY model follows a Gaussian distribution as expected [125]. The tails of the DOS of H_M also follow a Gaussian distribution; however, the peak is better described by a Lorentzian fit, and is much sharper than that of the SY model. Hence, significantly more states in the spectrum of H_M have energies close to 0. This is likely due to the fact that each projection operator $P^{0,i}_j$ in H_M in Eq. (3.5) annihilates 8 out of the 9 states composing the Hilbert space of two spin-1 sites. The permutation operators $\mathbb{P}^{ij}$ in the SY model, on the other hand, do not annihilate states, and split the space of two spin-1 sites into SU(3) irreps of dimensions 6 and 3, with respective eigenvalues 1 and -1. We would hence expect a greater density of states near 0 energy for the H_M model.

A.3 Limiting Form for M Large, N Fixed

In this appendix, we show that for $M \geq 2N$, the Hilbert space is dominated by the nullspace, as displayed in (3.36):

$$\lim_{M\to\infty} \frac{D_{\mathcal{N}}}{M^{2N}} = 1$$

The proof follows from two facts: 1) for all states in the nullspace as given in (3.29), the dimension of the corresponding SU(M) multiplet grows as M^{2N} for fixed N, while 2) all other irreducible representations have dimension growing as a lower power of M.

We first note that $k + \ell \leq 2N < M$ when $M > 2N$. Since the restriction in the sum in (3.30) is always satisfied, the nullspace dimension simplifies to

$$D_{\mathcal{N}} = \sum_{k,\ell=1}^{N} \sum_{\boldsymbol{\lambda}\in P_{N,k}} \sum_{\boldsymbol{\gamma}\in P_{N,\ell}} m(\boldsymbol{\lambda}) m(\boldsymbol{\gamma}) d(\boldsymbol{\lambda} + \overline{\boldsymbol{\gamma}}). \tag{A.1}$$

The only dependence on M here is through the SU(M) dimension $d(\boldsymbol{\rho})$. The formula (3.32) for this dimension can then be factored into two pieces by splitting this product into one piece involving the first k rows of the Young diagram for $\boldsymbol{\rho}$, and another involving the other rows. The latter part of this diagram can be thought of as a separate Young diagram with entries $\boldsymbol{\rho}^{(M-k)} = [\boldsymbol{\rho}_{k+1}, \boldsymbol{\rho}_{k+2}, \ldots, \boldsymbol{\rho}_M] = [\overline{\boldsymbol{\gamma}}_{k+1}, \overline{\boldsymbol{\gamma}}_{k+2}, \ldots, \overline{\boldsymbol{\gamma}}_M]$. The corresponding contributions of this piece to $d(\boldsymbol{\rho})$ then amount to the dimension $d^{(M-k)}$ of the representation $\boldsymbol{\rho}^{(M-k)}$ in the group SU($M-k$), yielding

$$d(\boldsymbol{\rho}) = d^{(M-k)}\Big(\boldsymbol{\rho}^{(M-k)}\Big) \frac{\prod_{a=1}^{k}(\rho_a + M - a)!}{\prod_{a=1}^{k}\Big((M-a)!\prod_{b=1}^{\rho_a} h_{a,b}\Big)}. \tag{A.2}$$

The resulting large-M behavior is straightforward to determine. We have

$$\begin{aligned}\prod_{a=1}^{k}\frac{(\boldsymbol{\rho}_a + M - a)!}{(M-a)!} = &\prod_{a=1}^{k}\frac{(\boldsymbol{\lambda}_a + \boldsymbol{\gamma}_1 + M - a)!}{(M-a)!} \\ &\xrightarrow{M \text{ large}} M^{N+k\gamma_1}\ ,\end{aligned} \tag{A.3}$$

where we exploit the facts that $\sum_{a=1}^{k}\boldsymbol{\lambda}_a = N$ and $\overline{\boldsymbol{\gamma}}_a = \boldsymbol{\gamma}_1$ for $a \leq M - l$. Due to the latter fact along with $\boldsymbol{\gamma} \in P_{N,\ell}$, the first γ_1 columns in the Young diagram of $\overline{\boldsymbol{\gamma}}$ and hence $\boldsymbol{\rho}$ must be at least of length $M - l$. The remaining columns arise only from $\boldsymbol{\lambda}$, and so the corresponding hook lengths are independent of M, yielding

$$\prod_{a=1}^{k}\prod_{b=1}^{\rho_a} h_{a,b} \xrightarrow{M \text{ large}} M^{k\gamma_1} h(\boldsymbol{\lambda}) \tag{A.4}$$

Finally, we use the fact the dimensions of an SU($M-k$) representation and its conjugate are the same to derive

$$d^{(M-k)}\Big(\boldsymbol{\rho}^{(M-k)}\Big) = d^{(M-k)}\Big(\overline{\boldsymbol{\rho}^{(M-k)}}\Big) = d^{(M-k)}(\boldsymbol{\gamma})\ .$$

Here the hook lengths are independent of M, yielding

$$\begin{aligned}d^{(M-k)}\Big(\boldsymbol{\rho}^{(M-k)}\Big) = &\frac{1}{h(\boldsymbol{\gamma})}\prod_{a=1}^{\ell}\frac{(\boldsymbol{\gamma}_a + (M-k) - a)!}{(M-k-a)!} \\ &\xrightarrow{M \text{ large}} M^N \frac{1}{h(\boldsymbol{\gamma})}\ .\end{aligned} \tag{A.5}$$

Putting the above results together, we see that

$$d(\boldsymbol{\lambda} + \overline{\boldsymbol{\gamma}}) \xrightarrow{M \text{ large}} \frac{1}{h(\boldsymbol{\lambda})h(\boldsymbol{\gamma})} M^{2N}\ . \tag{A.6}$$

We proved that states in any SU(M) representation other than $\boldsymbol{\rho} = \boldsymbol{\lambda} + \overline{\boldsymbol{\gamma}}$ are not in the nullspace. For $M \geq 2N$, these states must be in representations $\rho \in \boldsymbol{\lambda} \otimes \overline{\boldsymbol{\gamma}}$ in the tensor product, as there are no restrictions on $\boldsymbol{\lambda} \in P_{N,k}$ and $\boldsymbol{\gamma} \in P_{N,l}$. Since $\overline{\boldsymbol{\gamma}}_a = \boldsymbol{\gamma}_1$ for $a \leq M - l$ and $k < M - l$, the inequality (3.25) means that at least one box in $\boldsymbol{\lambda}$ must move downward when forming ρ. Moreover, it must move to a row a with $a > M - \ell + 1$, as boxes originally in the same row cannot end up in the same column after taking the tensor product. We thus have $\sum_{i=1}^{k} \rho_a < N + k\boldsymbol{\gamma}_1$, as opposed to the equality used in the proof of (A.3). The number of boxes in $\rho^{(M-k)}$ must therefore increase, so that $d^{(M-k)}(\overline{\rho^{(M-k)}})$ must decrease relative to (A.5). Meanwhile, M in (A.4) is unchanged. Thus $d(\rho)$ for $\rho \neq \boldsymbol{\rho}$ increases at large M at most with a power M^{2N-2}.

We have shown that the only SU(M) representations with dimension growing as M^{2N} that appear are those in the nullspace. Since the total dimension of the Hilbert space is M^{2N}, the relation (3.36) must therefore hold.

A.4 Demonstrating Fragmentation for $m > 1$

Since, following the generalisation to general m performed in Section 3.2.6, the model remains a sum of positive semidefinite operators, the nullspace eigenstates for general m still consist of those states annihilated by each two-site term individually, and we may again obtain the nullspace dimension of the disordered model by computing that of the clean model. For general m, we recall that the clean model is given by

$$H_{\text{clean}} = \frac{1}{2}\left(C_{\mathbf{A}_m^{\otimes N}} + C_{\overline{\mathbf{A}}_m^{\otimes \tilde{N}}} - C_{\mathbf{A}_m^{\otimes N} \otimes \overline{\mathbf{A}}_m^{\otimes \tilde{N}}}\right) + \frac{m^2(N^2 + \tilde{N}^2)}{2M}, \tag{A.7}$$

where $C_{\mathbf{A}_m^{\otimes N}}$, $C_{\overline{\mathbf{A}}_m^{\otimes \tilde{N}}}$, and $C_{\mathbf{A}_m^{\otimes N} \otimes \overline{\mathbf{A}}_m^{\otimes \tilde{N}}}$ now refer to the Casimirs respectively acting on the first set of N spins transforming in the irrep with one column and m rows in its Young diagram, the second set of $\tilde{N}$ spins transforming in the irrep with one column and $(M-m)$ rows, and all spins combined. We proceed to consider how the tensor product of N copies of the irrep $(\overbrace{1, \ldots, 1}^{m}, 0, \ldots, 0)$ decomposes into irreps λ, and how the tensor product of $\tilde{N}$ copies of the irrep $(\overbrace{1, \ldots, 1}^{M-m}, 0, \ldots, 0)$ decomposes

into conjugate irreps $\overline{\gamma}$. We may directly apply the results from Section 3.2.2 to conclude that those SU(M) irreps which are part of the nullspace are those obtained by adding the elements of the partitions λ and $\overline{\gamma}$ together term by term, with k, the number of rows in λ, and ℓ, the number of rows in γ, satisfying $k + \ell \leq M$. We immediately note that for the case $m = M/2$, all but one of the irreps arising from $(\overbrace{1, \ldots, 1}^{M/2}, 0, \ldots, 0)^{\otimes N}$ have more than $M/2$ rows, likewise for $(\overbrace{1, \ldots, 1}^{M/2}, 0, \ldots, 0)^{\otimes \tilde{N}}$. Hence there is only one SU(M) irrep in the nullspace, and Hilbert space fragmentation does not occur. This is expected, since for $m = M/2$, the model is equivalent to the SY model with $m = M/2$.

We next consider $m < M/2$. We will not aim to derive a general formula for the dimension of the nullspace for this case, but rather simply to show that the dimension of the nullspace grows exponentially with N. Let us consider the cases where the irrep on the spins individually transforming in $\overline{\mathbf{A}}_m$ is $\overline{\gamma} = (\overbrace{\tilde{N}, \ldots, \tilde{N}}^{M-m}, 0, \ldots, 0)$, such that $l = m$. For the irrep λ on the spins individually transforming in $\mathbf{A}_m$, if we choose λ to have k rows such that $k \leq m + 1 \leq M - l$, then the irrep obtained by gluing the diagram for λ row-by-row to the diagram for $\overline{\gamma}$ is part of the nullspace. We may obtain an irrep λ satisfying this condition from the decomposition of $(\overbrace{1, \ldots, 1}^{m}, 0, \ldots, 0)^{\otimes N}$ by moving n blocks, with $n \leq N/2$, from the mth row of their original irrep to row $m + 1$ in constructing λ. There are $\binom{N}{n}$ ways to choose which blocks to shift one row down, and the number of nullspace SU(M) irreps thus obtained is $\sum_{n=0}^{N/2} \binom{N}{n} \geq 2^{N-1}$. Thus the number of irreps λ which yield a nullspace irrep grows exponentially, and Hilbert space fragmentation occurs.

B

Appendices for Chapters 4 and 5

B.1 Additional Derivations for BFESs

Here we present proofs for some of the results discussed in Section 4.2.3.

B.1.1 One BFES per Symmetry Sector

The first result is a proof for the statement:

There is exactly one BFES in each (N, X) symmetry sector.

As we have shown in Case 3 of the uniqueness proof in Section 4.2.1, there is at most one BFES in each (N, X) sector, and so it suffices for us now to show that there is also at least one BFES in each (N, X) sector. The fact that there is at least one such BFES was derived in collaboration with Riccardo Senese [2]. We recall that, as also shown in Case 3 of the uniqueness proof in Section 4.2.1, there is a unique number N_L of particles on the left boundary site which is compatible with a BFES in a given (N, X) sector. Assuming (for now) that $N_L > 0$, the BFES made of N particles with the highest dipole moment, $X_{\max}$ is given by

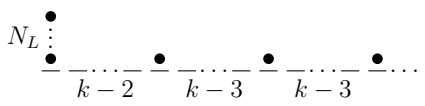

(B.1)

where the leftmost sequence of $k-2$ holes is followed by a series of sequences of $k-3$ holes until either all particles are positioned or the right boundary is reached,

in which case the remaining particles are stacked on the right boundary. Likewise, the BFES with the lowest dipole moment $X_{\min}$ is given by

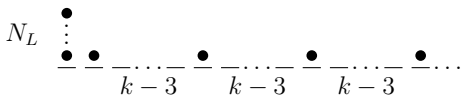

(B.2)

where again sequences of only $k-3$ particles are repeated until all particles are placed or the right boundary is encountered.

We assume $X_{\min} \leq X \leq X_{\max}$. We now demonstrate an iterative procedure which, starting from the BFES with dipole moment $X_{\max}$ in Eq. (B.1), constructs a BFES for each intermediate value of X between $X_{\max}$ and $X_{\min}$. We begin by moving the leftmost particle not on a boundary site one site to the left, yielding the state

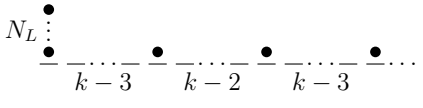

(B.3)

We then move the next particle over one site left, yielding

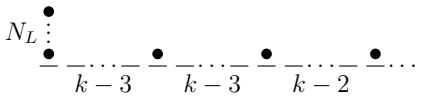

(B.4)

We see that at each step, we obtain a new BFES (since there is still only one pair of particles separated by $k-2$ holes) and that we lower the dipole moment X by 1. We continue this process of shifting the next particle over by 1 site to the left until we reach the rightmost particle not on a boundary site. If this particle, after having been shifted left, is separated by $k-2$ holes from the right boundary site (and $N_R \neq 0$), then for the next move we shift one particle from the right boundary stack one site to the left. In terms of diagrams, if we find ourselves with the situation

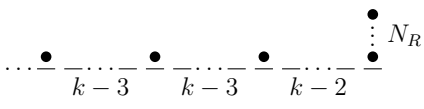

(B.5)

then we move one particle from the rightmost stack left, yielding

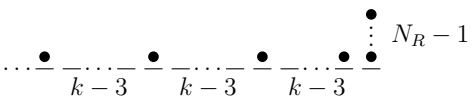

(B.6)

We then loop back to the leftmost particle not on the left boundary, and move it one site left again, yielding

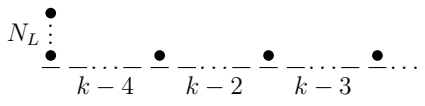

(B.7)

Iterating this procedure, it is clear we will eventually arrive at the BFES with dipole moment $X_{\min}$ in Eq. (B.2), and furthermore that along the way, we will have constructed a BFES with each intermediate value of X. This concludes the proof for $N_L > 0$; the proof for $N_L = 0$ follows very similar lines, where one instead starts with the state with the maximal dipole moment for $N_R = N$, then shifts one particle from the boundary one site to the left. One then follows identical steps to those described above, constructing a BFES with every possible intermediate value of X until one arrives at the state in Eq. (B.2) with $N_L = 0$.

B.1.2 Dividing an FES into Sub-BFESs

Here we prove that:

Say an initial state is expanded via a series of outward hops to an FES. The resulting FES can then be divided into sub-BFESs such that no particles in different sub-BFESs interacted during the outward expansion.

To prove this, we consider dividing the FES in question into several sub-FESs such that:

1. Each particle in each sub-FES was, at some point during the expansion, separated by $k-4$ sites or fewer from the next particle over to its right and to its left in the sub-FES (or was stacked on them, in the case of $k = 3$).

2. The leftmost and rightmost particles in each sub-FES were, at all points during the expansion, separated by at least $k-3$ sites from all of the particles outside the sub-FES (or were never stacked on them for $k = 3$).

It is clear that particles within different sub-FESs in this construction will not have interacted during the outward expansion, since for two particles to interact via an outward hop, at some point during the expansion they would need to be separated by $k-4$ sites or fewer. We now prove that all the sub-FESs constructed in this way are sub-BFESs, from which the main result immediately follows as a corollary. In other words, we prove the theorem:

Say an initial state is expanded via a series of outward hops to an FES. Assume furthermore that for a particular sub-FES within the FES, each pair of particles separated only by holes within the sub-FES was, at some point during the expansion, separated by $k-4$ holes or fewer (or stacked, in the case of $k=3$). Then that sub-FES is a sub-BFES.

The proof is as follows. Say the sub-FES in question was not a sub-BFES. Then there must either be at least one pair of particles in the sub-FES separated by $\geq k-1$ holes, or else at least two pairs of particles separated by $k-2$ holes. Furthermore, there must exist a sequence of inward hops such that when these hops are applied to the FES, each pair of particles separated only by holes in the concerned sub-FES will at some point during the sequence be separated by $k-4$ holes or fewer. This sequence of inward hops is simply the inverse of the sequence of outward hops used to map to the FES in the first place. It is then apparent, following identical logic to that employed in the uniqueness proof in Section 4.2.1, that such a sequence of inward hops cannot exist: there must be at least one pair of particles which, throughout the application of the sequence of inward hops, are separated by at least $k-3$ holes. Indeed, if there is a pair of particles in the sub-FES separated by $\geq k-1$ holes, then clearly those particles will remain separated during the inward hops. Likewise, if there are at least two pairs of particles separated by $k-2$ holes, then we can follow identical logic to that used in case 2 of the uniqueness proof of Section 4.2.1 to show that this will result in one pair of particles in the sub-FES always being separated by at least $k-3$ holes during the inward hops. Thus the result is proven by contradiction.

B.2 Calculation of Densities of Various Particle Configurations

In this appendix, we compute several functions of use for Section 4.3.

B.2.1 Calculation of $b^{(2)}(k,N,L)$ and $b^{(\infty)}(k,N,L)$

Here we compute exact expressions for the functions $b^{(2)}(k,N,L)$ and $b^{(\infty)}(k,N,L)$, which for $d=2$ and $d=\infty$ respectively give the total number of ways to arrange N particles over L sites such that they satisfy the no-propagation constraints

$$i_n^0 \geq (n-1)(k-2) \tag{B.8}$$

for $n = 1,\ldots,N$. For $d = 2$, we have

$$b^{(2)}(k,N,L) = \sum_{i_N=(N-1)(k-2)}^{L-1} \cdots \sum_{i_2=(k-2)}^{i_3-1} \sum_{i_1=0}^{i_2-1} 1. \tag{B.9}$$

We shall prove that this sum equals

$$b^{(2)}(k,N,L) = \binom{L+(k-2)}{N} \frac{L-(N-1)(k-2)}{L+(k-2)}. \tag{B.10}$$

We proceed by induction. The case $N = 1$ is trivial. Assume the result holds up to $N-1$, and consider the case of N. We have that

$$b^{(2)}(k,N,L) = \sum_{N_M=1}^{N} b^{(2)}(k,N-N_M,(N-1)(k-2)) \binom{L-(N-1)(k-2)}{N_M}. \tag{B.11}$$

The summation variable N_M gives the number of particles situated on sites $(N-1)(k-2)$ to $L-1$. Since there is no constraint on the positions of particles on those sites, the number of possible arrangements is given by the simple binomial in the above expression. The remaining $N-N_M$ particles, which are situated on sites 0 to $(N-1)(k-2)-1$, must obey the position constraints $i_1 \geq 0$, $i_2 \geq (k-2)$, etc. Hence the sum over all of their possible positions is given by $b^{(2)}(k,N-N_M,(N-1)(k-2))$.

With some work, the summation in Eq. (B.11) can be rewritten as

$$\begin{aligned} b^{(2)}(k,N,L) =& \frac{L-(N-1)(k-2)}{N} \binom{N(k-2)}{N-1} \\ & {}_2F_1(-L-(k-3)+N(k-2), -N+1, N(k-3)+2, 1), \end{aligned} \tag{B.12}$$

where the hypergeometric function is given by

$$ {}_2F_1(-L-(k-3)+N(k-2),-N+1,N(k-3)+2,1) = \sum_{p=0}^{L+(k-3)-N(k-2)} (-1)^p \binom{L+(k-3)-N(k-2)}{p} \frac{(-N+1)_p}{(N(k-3)+2)_p}, \tag{B.13} $$

in which the subscript p corresponds to the Pochhammer symbol notation. Applying Gauss' hypergeometric theorem and simplifying the result completes the proof.

As concerns the $d = \infty$ case, due to stacking, we have

$$ b^{(\infty)}(k,N,\ell) = \sum_{i_N=(N-1)(k-2)}^{L-1} \cdots \sum_{i_2=(k-2)}^{i_3} \sum_{i_1=0}^{i_2} 1, \tag{B.14} $$

since each particle can also be positioned on top of the next particle over. Following identical logic to the previous derivation, one can then show

$$ b^{(\infty)}(k,N,L) = \frac{L-(N-1)(k-2)}{L+k-2} \binom{L+k+N-3}{N}. \tag{B.15} $$

B.2.2 Lower Bounds on Various Densities

We next compute a function which has several applications in the main text. In particular, we consider the function

$$ P^{(2)}(x,m,k,N,L) = \frac{\sum_{L_R=0}^{L-m} \sum_{N_R=N_{\min}}^{N_{\max}} b^{(2)}(k,N_R,L_R) b^{(2)}(k,N-N_R-x,L-L_R-m)}{L\binom{L}{N}}. \tag{B.16} $$

For a particular local configuration of x particles over m sites in a $d = 2$ system, this sum equals the average density of occurrences of that configuration amongst all states with N particles and L sites such that the particles to the right and left of the configuration satisfy the no-propagation condition of Eq. 4.25. The average is carried out over an entire N sector. The bounds on the sum over N_R are given by

$$ N_{\min} = \max\left(0, N - \left\lfloor \frac{L-L_R-m+k-3}{k-2} \right\rfloor\right), \tag{B.17} $$

$$ N_{\max} = \min\left(N, \left\lfloor \frac{L_R+k-3}{k-2} \right\rfloor\right), \tag{B.18} $$

The sum on the right-hand side of Eq. (B.16) involves polynomially many in L terms. A subset of the summands exponentially dominates in L over the others, and thus the leading order of the total sum coincides with the sum of this subset. Hence, the above sums can be approximated in the thermodynamic limit using Laplace's method. For lack of space we do not include the details here, but we refer the interested reader to the appendices of [2] where the full calculation can be found. The final result is

$$\lim_{L\to\infty} P^{(2)}(x, m, k, \nu L, L) = \nu^x (1-\nu)^{m+2-2(k-1)} (1-\nu/\nu_c)^2 \tag{B.19}$$

This leads to the formulas for the density of frozen sites in Eq. (4.36), the density of active blockages in Eq. (4.42), and the active bubble configuration density of Eq. (4.49).

The corresponding function for $d = \infty$ is given by

$$P^{(\infty)}(x,m, k, N, L) = \frac{\sum_{L_R=0}^{L-m} \sum_{N_R=N_{\min}}^{N_{\max}} b^{(\infty)}(k, N_R, L_R) b^{(\infty)}(k, N - N_R - x, L - L_R - m)}{L\binom{L+N-1}{N}}. \tag{B.20}$$

The thermodynamic limit expression is derived using an identical approach to the $d = 2$ case, and is found to be

$$\lim_{L\to\infty} P^{(\infty)}(x, m, k, \nu L, L) = \nu^x (1+\nu)^{-(x+m+2-2(k-1))} (1-\nu/\nu_c)^2. \tag{B.21}$$

From this we obtain the density of frozen sites in Eq. (4.39),the density of active blockages in Eq. (4.43), and the active bubble configuration density of Eq. (4.53).

B.3 Self-Averaging

In this appendix, we argue that by self-averaging in the thermodynamic limit [113], the exact density of frozen sites in a typical randomly chosen state equals $\overline{\rho}_F^{(d)}$, the mean density of frozen sites averaged over all states. Hence, the lower bounds on $\overline{\rho}_F^{(d)}$ derived in Section 4.3.3 also apply individually to almost all states at a given filling $\nu < \nu_c$ in the thermodynamic limit.

In the thermodynamic limit, we do not expect typical random states to have extensively large subregions that deviate significantly from the global density ν.

Indeed, for general d, let $p_n^{(d)}(\nu)$ denote the probability that a given site is occupied by n particles in a random state with filling ν. For $d = 2$ and $d = \infty$, this function can be computed exactly, yielding

$$p_n^{(2)}(\nu) = \lim_{\substack{L\to\infty \\ N=\nu L}} \binom{L-1}{N-n} \Big/ \binom{L}{N} = \nu^n (1-\nu)^{1-n} \tag{B.22}$$

$$p_n^{(\infty)}(\nu) = \lim_{\substack{L\to\infty \\ N=\nu L}} \binom{L+N-n-1}{N-n} \Big/ \binom{L+N-1}{N} = \nu^n (1+\nu)^{-(n+1)} \tag{B.23}$$

For other values of d, $p_n^{(d)}$ can be estimated numerically, and should have a mean value of $\overline{p}_n^{(d)} = \sum_{n=0}^{d} n p_n^{(d)} = \nu$.

In the thermodynamic limit, we can treat the number of particles on each site as i.i.d. random variables, with a probability distribution given by $p_n^{(d)}$. Since this probability distribution clearly has a finite variance, a simple application of the central limit theorem [113] implies that suitably large subregions should have density ν up to vanishingly small deviations.

Since $\nu < \nu_c$, this result means that in a typical randomly drawn state with filling ν there must be a finite density of blockages. Indeed, consider expanding the state in question to its corresponding FES in the FES picture. For $\nu < \nu_c$, we do not expect particles to travel very far from their point of origin during this expansion, as a group of particles needs to have a local density greater than ν_c to expand. This implies that any sufficiently large subregion of the FES should have a density close to ν, and so a finite fraction of the FES' particles must be separated from each other by $k-2$ or more holes to comply with $\nu < \nu_c$. This leads to a finite density of blockages (active, frozen, or both). The blockages should also be evenly distributed, so as not to create large regions deviating from ν.

We then make use of this finite density of blockages to divide the state into an extensive number of large, but finite, regions of roughly equal size, separated by blockages. We choose the size ζ of these regions to be much bigger than the typical distance between blockages. The mean density of frozen sites within these finite regions is then described by $\overline{\rho}_F(k, \nu\zeta, \zeta)$, and treating the densities in such finite regions as i.i.d.'s, the density of frozen sites in the whole of the randomly

drawn state should tend towards this mean value by the central limit theorem. This means thermodynamically large typical states should have a density of frozen sites that equals the mean density. Hence, lower bounds derived for the mean density of frozen sites should also apply to typical states in the thermodynamic limit.

To support these claims, in Section 4.3.5 we present numerical evidence that self-averaging is indeed occurring by showing that the variance on numerically computed lower bounds of $\overline{\rho}_F(k, N, L)$ vanishes as $L \to \infty$. We note that the above arguments can also be applied to other intensive quantities, such as the mean density of active blockages computed in Eq. (4.42) and Eq. (4.43), or of active bubbles computed in Eq. (4.46) and Eq. (4.51). We also have evidence of self-averaging in these cases, such as very small standard deviations for the data points taken for several $L = 10^6$ systems in Fig. 4.3.

B.4 Lower Bounds on $A_2(x, k, N, L)$ and $A_\infty(x, k, N, L)$

In this section, we proceed to explicitly compute some lower bounds on the $d = 2$ and $d = \infty$ active bubble density functions, $A_2(x, k, \nu L, L)$ and $A_\infty(x, k, \nu L, L)$ (as defined in Section 4.3.4), for various values of k and x. We begin with the simpler case of $A_\infty(x, k, \nu L, L)$, which we lower-bound for $k = 7$ and from $x = 2$ to $x = 6$. We have that

$$A_\infty(x,k = 7, \nu L, L) = \sum_{\ell=1+5(x-1)}^{1+6(x-1)} m_\infty(x, \ell, k = 7) a_\infty(x, \ell, k = 7, N, L), \tag{B.24}$$

The summation bounds are derived from Eqs. (4.48) (which also holds for $d = \infty$) and (4.52) in the main text, where a lower bound on $a_\infty(x, \ell, k = 7, N, L)$ in the thermodynamic limit is also provided in Eq. (4.53). Hence all that remains to be calculated are the multiplicities $m_\infty(x, \ell, k = 7)$. This can be done methodically with the aid of a computer as follows. For each value of ℓ in the summation, $m_\infty(x, \ell, k = 7)$ equals the sum of the dimensions of all local Krylov sectors with a corresponding local FES consisting of $\ell - (1 + 5(x - 1))$ pairs of particles separated by $k - 2$ holes and $1 + 6(x - 1) - \ell$ pairs of particles separated by $k - 3$ holes. For

example, $m_\infty(x, \ell = 1 + 5(x-1), k = 7)$ equals the dimension of the local Krylov sector that contains the local FES in which all pairs of particles are separated by $k-3$ holes. On the other hand, $m_\infty(x, \ell = 2 + 5(x-1), k = 7)$ equals the sum of the dimensions of the $x-1$ local Krylov sectors defined by the local FESs with exactly one pair of particles separated by $k-2$ holes; and so on. The dimension of the local Krylov sector associated with a given local FES can be determined by starting from that FES, then computing all possible states that can be reached from the FES via a series of inward hop operators. This necessarily maps out the whole of the FES, as by the results in Section 4.2.1, any state in a Krylov sector of a $d = \infty$ system can be reached by starting from the FES and applying inward hops. We present all the multiplicity values derived in this fashion in the table below, where the boxes filled are those between the bounds of $\ell_{\min}$ and $\ell_{\max}$:

$m_\infty(x, \ell, k = 7)$						
	$\ell = 1 + 5(x-1)$	$\ell = 2 + 5(x-1)$	$\ell = 3 + 5(x-1)$	$\ell = 4 + 5(x-1)$	$\ell = 5 + 5(x-1)$	$\ell = 6 + 5(x-1)$
x=2	3	4				
x=3	18	42	7			
x=4	131	462	108	19		
x=5	1111	5268	1446	408	40	
x=6	10462	62185	18688	6723	1077	97

We next consider, for $k = 5$, the $d = 2$ multiplicity function $m_2(x, \ell, k = 5)$. Although a given active bubble configuration cannot necessarily attain its corresponding local FES for d finite, one can show via brute force enumeration that for the values $x = 2$ to $x = 5$ that we consider, this will always be the case. Hence the local Krylov sectors for these values of x can be determined by starting from the corresponding local FES and mapping out all states attainable via a combination of inward and outward hops. This can be done numerically, yielding the results

$m_2(x, \ell, k = 5)$					
	$\ell = 1 + 5(x-1)$	$\ell = 2 + 5(x-1)$	$\ell = 3 + 5(x-1)$	$\ell = 4 + 5(x-1)$	$\ell = 5 + 5(x-1)$
x=2	2	2			
x=3	5	12	3		
x=4	15	62	27	5	
x=5	56	318	180	62	8

B.5 Proof of the CS-to-BES Algorithm

In this appendix, we prove the algorithm described in Section 4.4.2 for mapping a contracted state to a blockage-free extended state. We focus on the case of $d = 2$ for simplicity, from which it is clear how to generalise to higher d. We recall that the algorithm in question is given for $d = 2$ by

- For site $i \in \{0, \ldots, L-3\}$ in increasing order, if the sites i and $i+k-1$ are within the bounds of the system and are empty and all sites in-between them are occupied, apply the gate $U^{+}_{i,i+k-1}$. Repeat the loop over sites until it is no longer possible to apply this gate.

- For $\ell \in \{k-4, \ldots, 1\}$ in decreasing order, for site $i \in \{0, \ldots, L-3\}$ in increasing order, if the sites i and $i+\ell+2$ are within the system and empty and all sites in-between are occupied, apply the gate $U^{+}_{i,i+\ell+2}$; otherwise, if the sites i and $i+\ell+3$ are within the system and empty and all sites in-between are occupied, apply $U^{+}_{i,i+\ell+3}$.

- For $\ell \in \{1, \ldots, k-4\}$ in increasing order, for site $i \in \{0, \ldots, L-3\}$ in increasing order, apply the gate $U^{+}_{i,i+\ell+2}$ if possible, and if not then apply the gate $U^{+}_{i,i+\ell+3}$ if possible.

To prove that this algorithm works, we note that a CS for $d = 2$ consists of a series of clusters of particles, each separated by one hole from its neighbouring clusters. By a cluster, we mean a group of occupied contiguous sites. We also recall that at most one of these clusters contains $k-2$ particles; the rest all contain $k-3$ particles, up to the possible exception of the leftmost and rightmost clusters, which may contain fewer particles.

Let us label the clusters in a given CS by an index $j = 1, \ldots, N_C$, where N_C is the initial total number of particle clusters. As the algorithm is carried out, new clusters may form to the left and right of the existing ones. When a new cluster is formed to the left, we take the range of j to extend downward, so a first new leftward cluster will have $j = 0$, a second new one will have $j = -1$, and so on. Likewise,

when new clusters are formed to the right, the upper range of the index j extends beyond N_C. We denote the number of particles in each cluster by c_j. When, after a series of hops, $c_j = 0$ this indicates there are no particles left in that cluster (hence the holes that were originally on either side of the cluster become adjacent); we will continue to label the "empty cluster", however, to preserve notational consistency.

Let us consider the first step in the algorithm. If there is no cluster of size $k-2$, this step does not have an impact. If there is such a cluster, then say it is at index j, such that $c_j = k-2$, and that the leftmost particle in the cluster is at site $i+1$. After the outward hop gate $U^{+}_{i,i+k-1}$ is applied to it, the following changes in cluster size occur:

$$\begin{aligned} c_j &= k-4, \\ c_{j+1} &= c_{j+1}+1, \\ c_{j-1} &= c_{j-1}+1. \end{aligned}$$

Indeed, the jth cluster loses two particles, and the clusters to its left and right both gain one (or new clusters are started if they are not there already). If the new value of c_{j+1} satisfies $c_{j+1} < k-2$, then no further hops are applied until the algorithm loops back round to the first site. If $c_{j+1} = k-2$, on the other hand, then the outward hop operator is applied again, resulting in

$$\begin{aligned} c_{j+1} &= k-4, \\ c_j &= k-3, \\ c_{j+2} &= c_{j+2}+1. \end{aligned}$$

Again, a further hop operator is only applied if $c_{j+2} = k-2$; these outward hops continue until an outward hop occurs in which no cluster of size $k-2$ is formed, or else a cluster of size $k-2$ is formed which overlaps with the boundary (in which case the particles just contribute to the pile-up at the boundary). At this point, the algorithm loops back to the first site.

When the algorithm loops back to the first site and runs through again, then $c_{j-1} \leq k-2$, and all other clusters (up to the possible exception of those on the

boundary) have size less than $k-2$. If $c_{j-1} < k-2$, then the first step of the algorithm terminates. If $c_{j-1} = k-2$, then the same series of hops is performed again, with the end result that either $c_{j-2} = k-2$ or else no cluster away from the boundaries has size $k-2$. This continues until no clusters of size $k-2$ not on the boundary are left, which must eventually occur due to the finite size of the system.

We then consider the second step of the algorithm. For each value of ℓ, at the beginning of the loop, $\ell+1$ is the size of the largest clusters present, and at the end of the loop, ℓ is the size of the largest clusters present (disregarding boundaries). To demonstrate this, we note that it is straightforward to show following identical logic to the last step that by the end of each loop over all sites, the number of clusters of size $\ell+1$ is lesser or equal to what it was before the loop over all sites; and furthermore that if it is equal, then the index of the leftmost cluster of size $\ell+1$ has decreased by 1. Hence, repeated application of the loop over all sites eventually results in the absence of any clusters of size $\ell+1$ away from the boundaries. The loop over the values of ℓ itself eventually results in all clusters away from the boundaries having a size of at most 1, and hence in all particles not in boundary pile-ups being separated by at least one (and at most 2) holes from their neighbours.

The third step of the algorithm follows identical logic in reverse. For each value of ℓ, at the start all particles are separated by at least ℓ and at most $\ell+1$ holes from their neighbours, and by the end they are all separated by at least $\ell+1$ and at most $\ell+2$ holes. By the end of the algorithm, all particles are separated by at least $k-3$ and at most $k-2$ holes. However, it can readily be shown that there can only be one instance of $k-2$ holes, since if there were two or more, then following logic identical to that in step 2 of the uniqueness proof in Section 4.2.1, it would be impossible via a series of solely inward hops to arrive at a CS; but it must be possible since the sequence of outward hops we applied in our algorithm can be reversed.

In the case of general finite d, the "clusters" become groups of neighbouring sites each containing $d-1$ particles. The first step of the algorithm removes any cluster of $k-2$ sites, and the second step removes any clusters of even one site, as it results in a state where no sites aside from boundary pile-ups have occupancy

$d-1$. The third step then completes the expansion to the BES. The proof of the general d algorithm is almost identical to that presented above for $d = 2$.

B.6 Deriving $P_{\mathrm{b}}(\nu)$ for $d = 2$, $k = 4$

We aim to derive an exact expression for the function $P_{\mathrm{b}}(\nu)$, which for $k = 4$ and $d = 2$ gives the probability that, starting from a given site (and assuming the preceding 2 sites are part of an active bubble), a pattern of particles and holes arises such that the first three sites in the pattern are frozen sites.

We begin by noting that the first three sites in the pattern must either all be holes or particles. This is because the preceding 2 sites are part of an active bubble, and so they must consist of one particle and one hole, with the respective positions of the particle and hole swapping as the system evolves with time. Hence, if the first three sites of the pattern contained both particles and holes, it is easy to see this would allow a hopping move to occur via interaction with a particle in the active bubble, and so the 3 sites would not all be frozen.

In view of this result, we proceed to decompose our function as

$$P_{\mathrm{b}}(\nu) = (1-\nu)^3 p_{\mathrm{b}}(\nu) + \nu^3 p_{\mathrm{b}}(1-\nu),$$

where $p_{\mathrm{b}}(\nu)$ is the probability that starting from a given site, a pattern arises such that the first site in the pattern is either empty or, if it contains a particle, the particle is unable to perform an outward hop. Hence, if the three sites next to the active bubble are holes, $p_{\mathrm{b}}(\nu)$ is the probability that the following sites are configured such that those 3 holes are frozen; and likewise, if the three sites are particles, then $p_{\mathrm{b}}(1-\nu)$ gives the probability that those three particles are frozen.

To make the computation of $p_{\mathrm{b}}(\nu)$ more intuitive to follow, instead of expressing it as a sum over powers of ν and $(1-\nu)$, we express it as a sum over sequences of "0" (indicating a hole) and "1" (indicating a particle), with the rule $0 \to (1-\nu)$ and $1 \to \nu$. By the above definition of $p_{\mathrm{b}}(\nu)$, we immediately have that

$$p_{\mathrm{b}}(\nu) = 0 + 1 \ldots, \tag{B.25}$$

where by the "$\ldots$" in the above, we mean that further terms need to be specified in the sequence to ensure that its starting particle (represented by "1") cannot hop outward. If this first 1 is followed by a 0 then another 1, we find ourselves in the same situation: the first particle in the sequence cannot hop outward only if the newly added particle cannot hop outward. This pattern repeats itself if we add on indefinitely many further terms of the form 01, and so

$$p_{\mathrm{b}}(\nu) = 0 + 1\left(\sum_{i=0}^{\infty}(01)^i\right)\ldots \tag{B.26}$$

The next term we could add to the sequence is either a 00 or a 11 (since a 10 would allow the first particle in the sequence to perform an outward hop). A 00 already achieves the goal of preventing an outward hop. A 11 on the other hand requires that more of the sequence be specified to ensure an outward hop cannot happen. Hence we have

$$p_{\mathrm{b}}(\nu) = 0 + 1\left(\sum_{i=0}^{\infty}(01)^i\right)[00 + 11\ldots] \tag{B.27}$$

If we have a 11 term, we must ensure that the second of these two particles cannot perform an inward hop with the remaining particles in the sequence. If we add a 01 to the sequence, then we have the same situation: we must ensure that the latest particle added to the sequence cannot perform an inward hop. Thus we have

$$p_{\mathrm{b}}(\nu) = 0 + 1\left(\sum_{i=0}^{\infty}(01)^i\right)\left[00 + 11\left(\sum_{i=0}^{\infty}(01)^i\right)\ldots\right] \tag{B.28}$$

If we add on a further 1 after this, then the inward hop cannot occur and we are done. If we add on a 00, then we must add on a third 0, as a 001 would allow an inward hop with the before-last particle. Thus

$$p_{\mathrm{b}}(\nu) = 0 + 1\left(\sum_{i=0}^{\infty}(01)^i\right)\left[00 + 11\left(\sum_{i=0}^{\infty}(01)^i\right)(1 + 000\ldots)\right] \tag{B.29}$$

For the final term, we note that our aim is achieved only if the last sequence 000 is followed by a fourth hole 0, or else by a particle 1 that cannot perform an outward hop. We therefore have

$$p_{\mathrm{b}}(\nu) = 0 + 1\left(\sum_{i=0}^{\infty}(01)^i\right)\left[00 + 11\left(\sum_{i=0}^{\infty}(01)^i\right)(1 + 000p_{\mathrm{b}}(\nu))\right] \tag{B.30}$$

Substituting $(1-\nu)$ for "0" and ν for "1" in the above equation and solving it, we obtain our desired result:

$$p_{\mathrm{b}}(\nu) = \frac{1 - 2\nu + 2\nu^2 - \nu^3 + \nu^4}{1 - 2\nu + 3\nu^2 - 3\nu^3 + 4\nu^4 - 3\nu^5 + \nu^6} \tag{B.31}$$

B.7 Island Counting Function for Finite L

We here derive a general expression for the island counting function $\mathscr{I}(x, N, k, L)$ defined in Section 5.2.1, which counts the total number of interacting islands with x particles over all states in a given N sector. As shown in Eq. (5.14), it is sufficient for $x < N$ and periodic boundaries to compute $\mathscr{I}_1(x, N, k, L)$, which is the total number of states in an N sector that have an interacting island with x particles starting on site 1, and then multiply this result by L. For $x = N$ however, the situation becomes more complicated. We begin with the simpler cases of $k = 2$ and $k = 3$ as illustrative examples before moving on to the case of general k.

In the case of $k = 2$, an interacting island with x particles simply consists of a sequence of x particles with a hole on either side. Hence, we have that

$$\mathscr{I}(x < N, N, k = 2, L) = L\Theta(L - 2 - N)\binom{L - x - 2}{N - x}, \tag{B.32}$$

where the binomial counts all possible ways to arrange the particles outside the island while leaving a hole on either side, and the Heaviside theta ensures $L \geq N + 2$ and hence that such a construction is possible. For the case $x = N$, the setting is even simpler, and it is apparent that

$$\mathscr{I}(x = N, N, k = 2, L) = L^{1-\delta_{L,N}}. \tag{B.33}$$

For the situation $k \geq 3$, there can be holes within the interacting islands provided that no particle in the island is separated by more than $k - 2$ holes from the next particle over in the island. Let us refer to the regions between particles in a given island as gaps. For $k = 3$, each gap can contain either one hole or no holes. Assuming $x < N$ to start, let n_1 denote the number of gaps in an island that contain a hole.

We note that $n_1 \leq \min(x-1, L-N-4)$, since we need at least 2 holes on either side to distinguish the island in question from the next islands over. Hence, we have that

$$\mathscr{I}(x < N, N, k = 3, L) = L \sum_{n_1=0}^{\min(x-1,L-N-4)} \binom{L-x-n_1-4}{N-x} \binom{x-1}{n_1}, \quad \text{(B.34)}$$

where the first binomial computes the number of ways to arrange the n_1 holes among the $x-1$ gaps and the second binomial counts the number of ways to arrange the remaining particles in the system. For $x = N$, we obtain $\mathscr{I}(x = N, N, k = 3, L)$ by counting the number of states containing a single island. We distinguish between two types of states: those that contain a sequence of 2 or more holes, and those that don't. For those that do, one can naturally define a start and an end to the island contained in the state, the start being the particle immediately following the sequence of holes, and the end being the particle immediately preceding them. As previously, we may count these types of states by counting the number of states with a single island starting at position 1, and multiplying the result by L. The total number of such states is given by:

$$L \sum_{n_1=0}^{\min(N-1,L-N-2)} \binom{N-1}{n_1} \quad \text{(B.35)}$$

Note that the upper bound on the summation now requires that at least two holes be left outside the island, instead of 4.

For those states that do not contain a sequence of two or more holes, there is no longer a natural starting point to the island. One instead computes all possible arrangements of the N particles such that no two particles are separated by more than one hole. The total number of such states is

$$\binom{N+1}{L-N} - \binom{N-1}{L-N-2}. \quad \text{(B.36)}$$

The binomial on the left counts all possible ways to construct a state with $L-N$ holes arranged individually around n particles. The binomial on the right subtracts off those states in which there is a hole both on sites 1 and L in the

state, since those states in fact contain a sequence of 2 adjacent holes via the periodic boundary. Thus we have

$$\mathscr{I}(x=N,N,k=3,L)=\binom{N+1}{L-N}-\binom{N-1}{L-N-2}+L\sum_{n_1=0}^{\min(N-1,L-N-2)}\binom{N-1}{n_1}. \tag{B.37}$$

The expressions for $k=3$ can be straightforwardly generalised for the case of general k. We begin with $x<N$. Each gap in an island can contain between 0 and $k-2$ holes, and there must be at least $(k-1)$ holes on each side of the island. Let n_1 indicate the number of gaps containing one hole, n_2 indicate the number of gaps containing two holes, and so on up to n_{k-2}. We then have that:

$$\begin{aligned}\mathscr{I}(x<N,N,k,L)=&L\left(\prod_{\ell=1}^{k-2}\sum_{n_\ell=0}^{\min(x-1-\sum_{i=1}^{\ell-1}n_i,(L-N-2(k-1)-\sum_{i=1}^{\ell-1}in_i)/\ell)}\right)\\&\binom{L-x-2(k-1)-\sum_{i=1}^{k-2}in_i}{N-x}\prod_{j=1}^{k-2}\binom{x-1-\sum_{i=1}^{j-1}n_i}{n_j}\end{aligned} \tag{B.38}$$

Once more, the first binomial computes the number of ways to arrange the $N-x$ particles outside the island on the remaining sites, and the other binomials compute the number of ways to arrange the various sequences of holes in the gaps of the island.

For $x=N$, we get:

$$\begin{aligned}\mathscr{I}(x=N,N,k,L)=&\left(\prod_{\ell=1}^{k-2}\sum_{n_\ell=0}^{\min(x-1-\sum_{i=1}^{\ell-1}n_i,(L-N-(k-1)-\sum_{i=1}^{\ell-1}in_i)/\ell)}\right)\\&(L-(\Theta(L-N-\sum_{i=1}^{k-2}in_i-(k-1))-\Theta(L-N-\sum_{i=1}^{k-2}in_i-(2k-3)))(2k-3-L+N+\sum_{i=1}^{k-2}in_i))\\&\prod_{j=1}^{k-2}\binom{x-1-\sum_{i=1}^{j-1}n_i}{n_j}\\&+\left(\prod_{\ell=2}^{k-2}\sum_{n_\ell=0}^{(L-N-\sum_{i=2}^{\ell-1}in_i)/\ell}\right)\left(\binom{x+1-\sum_{i=2}^{k-2}n_i}{L-N-\sum_{i=2}^{k-2}in_i}\prod_{j=2}^{k-2}\binom{x+1-\sum_{i=2}^{j-1}n_j}{n_j}\right).\end{aligned} \tag{B.39}$$

The first term, covering the first three lines, counts the number of ways to construct a state with a single island and a sequence of at least $k-1$ holes outside the island. The product of binomials on the third line counts the number of ways to arrange the

sequences of holes in the gaps of the island. The term in the fourth line counts the number of ways to construct one big state without any sequences of $k-1$ holes. The various binomials in the fourth line count the number of ways to arrange sequences of between 1 and $k-2$ holes in the spaces around the particles. The first binomial counts the number of arrangements of gaps with one hole, while also enforcing that $n_1 = L - N - \sum_{i=2}^{k-2} n_i$. The contributions of spurious states, in which the number of holes on the left of the leftmost particle and on the right of the rightmost particle sum to $k-1$ or greater, are removed via the subtracted Heaviside step functions in line 2. Hence, the expression in Eq. (B.39) counts all possible ways to obtain a state where all particles are part of the same interacting island.

References

[1] J. Classen-Howes et al. “Bipartite Sachdev-Ye models with Read-Saleur symmetries”. In: *Phys. Rev. B* 110 (12 Sept. 2024), p. 125140. [Editors' Suggestion].

[2] J. Classen-Howes, R. Senese, and A. Prakash. “Universal Freezing Transitions of Dipole-Conserving Chains”. 2024. arXiv: `2408.10321 [cond-mat.str-el]`.

[3] Joshua M Deutsch. “Eigenstate thermalization hypothesis”. In: *Reports on Progress in Physics* 81.8 (July 2018), p. 082001.

[4] Luca D'Alessio et al. “From quantum chaos and eigenstate thermalization to statistical mechanics and thermodynamics”. In: *Advances in Physics* 65.3 (2016), pp. 239–362.

[5] Rahul Nandkishore and David A. Huse. “Many-Body Localization and Thermalization in Quantum Statistical Mechanics”. In: *Annual Review of Condensed Matter Physics* 6.1 (2015), pp. 15–38.

[6] Zlatko Papić. “Weak Ergodicity Breaking Through the Lens of Quantum Entanglement”. In: *Entanglement in Spin Chains: From Theory to Quantum Technology Applications*. Ed. by Abolfazl Bayat, Sougato Bose, and Henrik Johannesson. Cham: Springer International Publishing, 2022, pp. 341–395.

[7] P. W. Anderson. “Absence of Diffusion in Certain Random Lattices”. In: *Phys. Rev.* 109 (5 Mar. 1958), pp. 1492–1505.

[8] E. Abrahams et al. “Scaling Theory of Localization: Absence of Quantum Diffusion in Two Dimensions”. In: *Phys. Rev. Lett.* 42 (10 Mar. 1979), pp. 673–676.

[9] D.M. Basko, I.L. Aleiner, and B.L. Altshuler. “Metal–insulator transition in a weakly interacting many-electron system with localized single-particle states”. In: *Annals of Physics* 321.5 (2006), pp. 1126–1205.

[10] Dmitry A. Abanin et al. “Colloquium: Many-body localization, thermalization, and entanglement”. In: *Rev. Mod. Phys.* 91 (May 2019), p. 021001.

[11] Marcos Rigol, Vanja Dunjko, and Maxim Olshanii. “Thermalization and its mechanism for generic isolated quantum systems”. In: *Nature* 452.7189 (Apr. 2008), pp. 854–858.

[12] Hannes Bernien et al. “Probing many-body dynamics on a 51-atom quantum simulator”. In: *Nature* 551.7682 (Nov. 2017), pp. 579–584.

[13] C. J. Turner et al. “Weak ergodicity breaking from quantum many-body scars”. In: *Nature Physics* 14.7 (May 2018), pp. 745–749.

[14] Maksym Serbyn, Dmitry A. Abanin, and Zlatko Papić. “Quantum many-body scars and weak breaking of ergodicity”. In: *Nature Physics* 17.6 (June 2021), pp. 675–685.

[15] Sanjay Moudgalya, B. Andrei Bernevig, and Nicolas Regnault. "Quantum many-body scars and Hilbert space fragmentation: a review of exact results". In: *Reports on Progress in Physics* 85.8 (July 2022), p. 086501.

[16] C. J. Turner et al. "Quantum scarred eigenstates in a Rydberg atom chain: Entanglement, breakdown of thermalization, and stability to perturbations". In: *Phys. Rev. B* 98 (15 Oct. 2018), p. 155134.

[17] Sanjay Moudgalya et al. "Exact excited states of nonintegrable models". In: *Phys. Rev. B* 98 (23 Dec. 2018), p. 235155.

[18] Sanjay Moudgalya, Nicolas Regnault, and B. Andrei Bernevig. "Entanglement of exact excited states of Affleck-Kennedy-Lieb-Tasaki models: Exact results, many-body scars, and violation of the strong eigenstate thermalization hypothesis". In: *Physical Review B* 98.23 (Dec. 2018).

[19] Michael Schecter and Thomas Iadecola. "Weak Ergodicity Breaking and Quantum Many-Body Scars in Spin-1 XY Magnets". In: *Phys. Rev. Lett.* 123 (14 Oct. 2019), p. 147201.

[20] Thomas Iadecola and Michael Schecter. "Quantum many-body scar states with emergent kinetic constraints and finite-entanglement revivals". In: *Phys. Rev. B* 101 (2 Jan. 2020), p. 024306.

[21] Daniel K. Mark and Olexei I. Motrunich. "η-pairing states as true scars in an extended Hubbard model". In: *Phys. Rev. B* 102 (7 Aug. 2020), p. 075132.

[22] Christopher M. Langlett et al. "Rainbow scars: From area to volume law". In: *Phys. Rev. B* 105 (6 Feb. 2022), p. L060301.

[23] Bart van Voorden, Jiří Minář, and Kareljan Schoutens. "Quantum many-body scars in transverse field Ising ladders and beyond". In: *Phys. Rev. B* 101 (22 June 2020), p. 220305.

[24] Naoto Shiraishi and Takashi Mori. "Systematic Construction of Counterexamples to the Eigenstate Thermalization Hypothesis". In: *Phys. Rev. Lett.* 119 (3 July 2017), p. 030601.

[25] Daniel K. Mark, Cheng-Ju Lin, and Olexei I. Motrunich. "Unified structure for exact towers of scar states in the Affleck-Kennedy-Lieb-Tasaki and other models". In: *Phys. Rev. B* 101 (19 May 2020), p. 195131.

[26] Sanjay Moudgalya, Nicolas Regnault, and B. Andrei Bernevig. "η-pairing in Hubbard models: From spectrum generating algebras to quantum many-body scars". In: *Phys. Rev. B* 102 (8 Aug. 2020), p. 085140.

[27] Jie Ren, Chenguang Liang, and Chen Fang. "Quasisymmetry Groups and Many-Body Scar Dynamics". In: *Phys. Rev. Lett.* 126 (12 Mar. 2021), p. 120604.

[28] K. Pakrouski et al. "Many-Body Scars as a Group Invariant Sector of Hilbert Space". In: *Phys. Rev. Lett.* 125 (23 Dec. 2020), p. 230602.

[29] Nicholas O'Dea et al. "From tunnels to towers: Quantum scars from Lie algebras and q-deformed Lie algebras". In: *Phys. Rev. Research* 2 (4 Dec. 2020), p. 043305.

[30] Sanjay Moudgalya and Olexei I. Motrunich. "Exhaustive Characterization of Quantum Many-Body Scars using Commutant Algebras". 2022. arXiv: `2209.03377 [cond-mat.str-el]`.

[31] Shriya Pai, Michael Pretko, and Rahul M. Nandkishore. "Localization in Fractonic Random Circuits". In: *Phys. Rev. X* 9 (Apr. 2019), p. 021003.

[32] Pablo Sala et al. "Ergodicity Breaking Arising from Hilbert Space Fragmentation in Dipole-Conserving Hamiltonians". In: *Phys. Rev. X* 10 (1 Feb. 2020), p. 011047.

[33] Vedika Khemani, Michael Hermele, and Rahul Nandkishore. "Localization from Hilbert space shattering: From theory to physical realizations". In: *Phys. Rev. B* 101 (May 2020), p. 174204.

[34] Sanjay Moudgalya and Olexei I. Motrunich. "Hilbert Space Fragmentation and Commutant Algebras". In: *Phys. Rev. X* 12 (1 Mar. 2022), p. 011050.

[35] Michael Pretko, Xie Chen, and Yizhi You. "Fracton phases of matter". In: *International Journal of Modern Physics A* 35.06 (2020), p. 2030003.

[36] Claudio Chamon. "Quantum Glassiness in Strongly Correlated Clean Systems: An Example of Topological Overprotection". In: *Phys. Rev. Lett.* 94 (Jan. 2005), p. 040402.

[37] Jeongwan Haah. "Local stabilizer codes in three dimensions without string logical operators". In: *Phys. Rev. A* 83 (Apr. 2011), p. 042330.

[38] Sagar Vijay, Jeongwan Haah, and Liang Fu. "A new kind of topological quantum order: A dimensional hierarchy of quasiparticles built from stationary excitations". In: *Phys. Rev. B* 92 (Dec. 2015), p. 235136.

[39] Rahul M. Nandkishore and Michael Hermele. "Fractons". In: *Annual Review of Condensed Matter Physics* 10 (2019), pp. 295–313.

[40] Andrey Gromov and Leo Radzihovsky. "Colloquium: Fracton matter". In: *Rev. Mod. Phys.* 96 (Jan. 2024), p. 011001.

[41] Alan Morningstar, Vedika Khemani, and David A. Huse. "Kinetically constrained freezing transition in a dipole-conserving system". In: *Phys. Rev. B* 101 (June 2020), p. 214205.

[42] Calvin Pozderac et al. "Exact solution for the filling-induced thermalization transition in a one-dimensional fracton system". In: *Phys. Rev. B* 107 (Jan. 2023), p. 045137.

[43] Sanjay Moudgalya et al. "Thermalization and Its Absence within Krylov Subspaces of a Constrained Hamiltonian". In: *Memorial Volume for Shoucheng Zhang* (Sept. 2021), pp. 147–209.

[44] Tibor Rakovszky et al. "Statistical localization: From strong fragmentation to strong edge modes". In: *Phys. Rev. B* 101 (12 Mar. 2020), p. 125126.

[45] Zhi-Cheng Yang et al. "Hilbert-Space Fragmentation from Strict Confinement". In: *Phys. Rev. Lett.* 124 (20 May 2020), p. 207602.

[46] Giuseppe De Tomasi et al. "Dynamics of strongly interacting systems: From Fock-space fragmentation to many-body localization". In: *Phys. Rev. B* 100 (21 Dec. 2019), p. 214313.

[47] Sreemayee Aditya, Deepak Dhar, and Diptiman Sen. "Subspace-restricted thermalization in a correlated-hopping model with strong Hilbert space fragmentation characterized by irreducible strings". In: *Phys. Rev. B* 110 (4 July 2024), p. 045418.

[48] Libor Caha and Daniel Nagaj. "The pair-flip model: a very entangled translationally invariant spin chain". 2018. arXiv: `1805.07168 [quant-ph]`.

[49] Atsuki Yoshinaga et al. "Emergence of Hilbert Space Fragmentation in Ising Models with a Weak Transverse Field". In: *Physical Review Letters* 129.9 (Aug. 2022).

[50] Oliver Hart and Rahul Nandkishore. "Hilbert space shattering and dynamical freezing in the quantum Ising model". In: *Phys. Rev. B* 106 (21 Dec. 2022), p. 214426.

[51] Balázs Pozsgay et al. "Integrable spin chain with Hilbert space fragmentation and solvable real-time dynamics". In: *Phys. Rev. E* 104 (4 Oct. 2021), p. 044106.

[52] Pietro Brighi, Marko Ljubotina, and Maksym Serbyn. "Hilbert space fragmentation and slow dynamics in particle-conserving quantum East models". In: *SciPost Phys.* 15 (2023), p. 093.

[53] Márton Borsi, Levente Pristyák, and Balázs Pozsgay. "Matrix Product Symmetries and Breakdown of Thermalization from Hard Rod Deformations". In: *Phys. Rev. Lett.* 131 (3 July 2023), p. 037101.

[54] Eulàlia Nicolau et al. "Flat band induced local Hilbert space fragmentation". In: *Phys. Rev. B* 108 (20 Nov. 2023), p. 205104.

[55] Eulàlia Nicolau et al. "Local Hilbert space fragmentation and weak thermalization in Bose-Hubbard diamond necklaces". In: *Phys. Rev. B* 107 (9 Mar. 2023), p. 094312.

[56] Bhaskar Mukherjee, Zi Cai, and W. Vincent Liu. "Constraint-induced breaking and restoration of ergodicity in spin-1 PXP models". In: *Phys. Rev. Res.* 3 (3 Aug. 2021), p. 033201.

[57] Bhaskar Mukherjee et al. "Minimal model for Hilbert space fragmentation with local constraints". In: *Phys. Rev. B* 104 (15 Oct. 2021), p. 155117.

[58] Dominik Hahn, Paul A. McClarty, and David J. Luitz. "Information dynamics in a model with Hilbert space fragmentation". In: *SciPost Phys.* 11 (2021), p. 074.

[59] Jonas Richter and Arijeet Pal. "Anomalous hydrodynamics in a class of scarred frustration-free Hamiltonians". In: *Phys. Rev. Res.* 4 (1 Jan. 2022), p. L012003.

[60] Christopher M. Langlett and Shenglong Xu. "Hilbert space fragmentation and exact scars of generalized Fredkin spin chains". In: *Phys. Rev. B* 103 (22 June 2021), p. L220304.

[61] Anwesha Chattopadhyay et al. "Strong Hilbert space fragmentation via emergent quantum drums in two dimensions". In: *SciPost Phys.* 14 (2023), p. 146.

[62] Pranay Patil and Anders W. Sandvik. "Hilbert space fragmentation and Ashkin-Teller criticality in fluctuation coupled Ising models". In: *Phys. Rev. B* 101 (1 Jan. 2020), p. 014453.

[63] Daniel Adler et al. "Observation of Hilbert space fragmentation and fractonic excitations in 2D". In: *Nature* 636.8041 (Dec. 2024), pp. 80–85.

[64] Faidon Andreadakis and Paolo Zanardi. "Coherence generation, symmetry algebras, and Hilbert space fragmentation". In: *Phys. Rev. A* 107 (6 June 2023), p. 062402.

[65] Melissa Will, Roderich Moessner, and Frank Pollmann. "Realization of Hilbert Space Fragmentation and Fracton Dynamics in Two Dimensions". In: *Phys. Rev. Lett.* 133 (19 Nov. 2024), p. 196301.

[66] Philipp Frey, Lucas Hackl, and Stephan Rachel. "Hilbert space fragmentation and interaction-induced localization in the extended Fermi-Hubbard model". In: *Phys. Rev. B* 106 (22 Dec. 2022), p. L220301.

[67] Yahui Li, Pablo Sala, and Frank Pollmann. "Hilbert space fragmentation in open quantum systems". In: *Phys. Rev. Res.* 5 (4 Dec. 2023), p. 043239.

[68] Alexandre Chaduteau et al. "Hilbert Space Fragmentation in the Chiral Luttinger Liquid". 2024. arXiv: `2409.10359 [cond-mat.str-el]`.

[69] Yiqiu Han, Xiao Chen, and Ethan Lake. "Exponentially slow thermalization and the robustness of Hilbert space fragmentation". 2024. arXiv: `2401.11294 [quant-ph]`.

[70] Xiaozhou Feng and Brian Skinner. "Hilbert space fragmentation produces an effective attraction between fractons". In: *Phys. Rev. Res.* 4 (1 Jan. 2022), p. 013053.

[71] Li Zhang et al. "Floquet engineering of Hilbert space fragmentation in Stark lattices". In: *Phys. Rev. B* 109 (18 May 2024), p. 184313.

[72] Somsubhra Ghosh, Indranil Paul, and K. Sengupta. "Prethermal Fragmentation in a Periodically Driven Fermionic Chain". In: *Phys. Rev. Lett.* 130 (12 Mar. 2023), p. 120401.

[73] K. Klocke, J. E. Moore, and M. Buchhold. "Power-Law Entanglement and Hilbert Space Fragmentation in Nonreciprocal Quantum Circuits". In: *Phys. Rev. Lett.* 133 (7 Aug. 2024), p. 070401.

[74] Matthew Wampler and Israel Klich. "Arrested development and fragmentation in strongly-interacting Floquet systems". In: *SciPost Phys.* 14 (2023), p. 145.

[75] Thomas Kohlert et al. "Exploring the Regime of Fragmentation in Strongly Tilted Fermi-Hubbard Chains". In: *Phys. Rev. Lett.* 130 (1 Jan. 2023), p. 010201.

[76] David T. Stephen, Oliver Hart, and Rahul M. Nandkishore. "Ergodicity Breaking Provably Robust to Arbitrary Perturbations". In: *Phys. Rev. Lett.* 132 (4 Jan. 2024), p. 040401.

[77] Gianluca Francica and Luca Dell'Anna. "Hilbert space fragmentation in a long-range system". In: *Phys. Rev. B* 108 (4 July 2023), p. 045127.

[78] N. Read and H. Saleur. "Enlarged symmetry algebras of spin chains, loop models, and S-matrices". In: *Nuclear Physics B* 777.3 (2007), pp. 263–315.

[79] G. A. P. Ribeiro and A. Lima-Santos. "Bethe ansatz for the Temperley–Lieb spin chain with integrable open boundaries". In: *Journal of Statistical Mechanics: Theory and Experiment* 2013.02 (Feb. 2013), P02035.

[80] M. T. Batchelor and M. N. Barber. "Spin-s quantum chains and Temperley-Lieb algebras". In: *Journal of Physics A: Mathematical and General* 23.1 (Jan. 1990), p. L15.

[81] Daniel Harlow. "The Ryu–Takayanagi Formula from Quantum Error Correction". In: *Communications in Mathematical Physics* 354.3 (May 2017), pp. 865–912.

[82] N. P. Landsman. "Lecture notes on C*-algebras, Hilbert C*-modules, and quantum mechanics". 1998. arXiv: `math-ph/9807030 [math-ph]`.

[83] Paolo Zanardi. "Virtual Quantum Subsystems". In: *Phys. Rev. Lett.* 87 (7 July 2001), p. 077901.

[84] Stephen D. Bartlett, Terry Rudolph, and Robert W. Spekkens. "Reference frames, superselection rules, and quantum information". In: *Rev. Mod. Phys.* 79 (2 Apr. 2007), pp. 555–609.

[85] Loïc Herviou, Jens H. Bardarson, and Nicolas Regnault. "Many-body localization in a fragmented Hilbert space". In: *Phys. Rev. B* 103 (13 Apr. 2021), p. 134207.

[86] James R. Garrison and Tarun Grover. "Does a Single Eigenstate Encode the Full Hamiltonian?" In: *Phys. Rev. X* 8 (2 Apr. 2018), p. 021026.

[87] Xiao-Liang Qi and Daniel Ranard. "Determining a local Hamiltonian from a single eigenstate". In: *Quantum* 3 (July 2019), p. 159.

[88] Britta Aufgebauer and Andreas Klümper. "Quantum spin chains of Temperley–Lieb type: periodic boundary conditions, spectral multiplicities and finite temperature". In: *Journal of Statistical Mechanics: Theory and Experiment* 2010.05 (May 2010), P05018.

[89] Subir Sachdev and Jinwu Ye. "Gapless spin-fluid ground state in a random quantum Heisenberg magnet". In: *Phys. Rev. Lett.* 70 (21 May 1993), pp. 3339–3342.

[90] A. Georges, O. Parcollet, and S. Sachdev. "Quantum fluctuations of a nearly critical Heisenberg spin glass". In: *Phys. Rev. B* 63 (13 Mar. 2001), p. 134406.

[91] Julian Sonner and Manuel Vielma. "Eigenstate thermalization in the Sachdev-Ye-Kitaev model". In: *Journal of High Energy Physics* 2017.11 (Nov. 2017), p. 149.

[92] Masudul Haque and P. A. McClarty. "Eigenstate thermalization scaling in Majorana clusters: From chaotic to integrable Sachdev-Ye-Kitaev models". In: *Phys. Rev. B* 100 (11 Sept. 2019), p. 115122.

[93] Bruce Eli Sagan. *The symmetric group : representations, combinatorial algorithms, and symmetric functions*. 2nd ed. Graduate texts in mathematics. New York: Springer, 2001.

[94] Michael E. Beverland et al. "Realizing exactly solvable SU(N) magnets with thermal atoms". In: *Phys. Rev. A* 93 (5 May 2016), p. 051601.

[95] Michael A. Perlin et al. "Engineering infinite-range SU(n) interactions with spin-orbit-coupled fermions in an optical lattice". In: *Phys. Rev. A* 105 (2 Feb. 2022), p. 023326.

[96] Dávid Jakab, Gergely Szirmai, and Zoltán Zimborás. "The bilinear–biquadratic model on the complete graph". In: *Journal of Physics A: Mathematical and Theoretical* 51.10 (Feb. 2018), p. 105201.

[97] Dávid Jakab and Zoltán Zimborás. "Quantum phases of collective SU(3) spin systems with bipartite symmetry". In: *Phys. Rev. B* 103 (21 June 2021), p. 214448.

[98] A M Perelomov and Vladimir S Popov. "Casimir Operators for Semisimple Lie Groups". In: *Mathematics of the USSR-Izvestiya* 2.6 (Dec. 1968), p. 1313.

[99] M. Hamermesh. *Group Theory and Its Application to Physical Problems*. Addison Wesley Series in Physics. Dover Publications, 1989.

[100] Hartmut Schlosser. "A Closed Formula for the Decomposition of the Kronecker Product of Irreducible Representations of SU(n)". In: *Mathematische Nachrichten* 134.1 (1987), pp. 237–243.

[101] Kieran Bull et al. "Tuning between Continuous Time Crystals and Many-Body Scars in Long-Range XYZ Spin Chains". In: *Phys. Rev. Lett.* 129 (14 Sept. 2022), p. 140602.

[102] Alessio Lerose et al. "Theory of robust quantum many-body scars in long-range interacting systems". 2023. arXiv: `2309.12504 [cond-mat.str-el]`.

[103] G Zhang and Z Song. "Quantum scars in spin-isotropic Heisenberg clusters". In: *New Journal of Physics* 25.5 (May 2023), p. 053025.

[104] K. Pakrouski et al. "Group theoretic approach to many-body scar states in fermionic lattice models". In: *Phys. Rev. Res.* 3 (4 Dec. 2021), p. 043156.

[105] Eiki Iyoda, Hosho Katsura, and Takahiro Sagawa. "Effective dimension, level statistics, and integrability of Sachdev-Ye-Kitaev-like models". In: *Phys. Rev. D* 98 (8 Oct. 2018), p. 086020.

[106] Zheng-Yuan Wang, Shintaro Takayoshi, and Masaaki Nakamura. "Spin-chain description of fractional quantum Hall states in the Jain series". In: *Phys. Rev. B* 86 (Oct. 2012), p. 155104.

[107] Emil J. Bergholtz, Masaaki Nakamura, and Juha Suorsa. "Effective spin chains for fractional quantum Hall states". In: *Physica E: Low-dimensional Systems and Nanostructures* 43.3 (2011). NanoPHYS 09, pp. 755–760.

[108] Sebastian Scherg et al. "Observing non-ergodicity due to kinetic constraints in tilted Fermi-Hubbard chains". In: *Nature Communications* 12.1 (July 2021), p. 4490.

[109] Sanjay Moudgalya, B. Andrei Bernevig, and Nicolas Regnault. "Quantum many-body scars in a Landau level on a thin torus". In: *Phys. Rev. B* 102 (19 Nov. 2020), p. 195150.

[110] W. Morong et al. "Observation of Stark many-body localization without disorder". In: *Nature* 599.7885 (Nov. 2021), pp. 393–398.

[111] Evert van Nieuwenburg, Yuval Baum, and Gil Refael. "From Bloch oscillations to many-body localization in clean interacting systems". In: *Proceedings of the National Academy of Sciences* 116.19 (2019), pp. 9269–9274.

[112] Cheng Wang and Zhi-Cheng Yang. "Freezing transition in the particle-conserving East model". In: *Phys. Rev. B* 108 (Oct. 2023), p. 144308.

[113] Shai Wiseman and Eytan Domany. "Lack of self-averaging in critical disordered systems". In: *Phys. Rev. E* 52 (Oct. 1995), pp. 3469–3484.

[114] Julius Lehmann et al. "Fragmentation-induced localization and boundary charges in dimensions two and above". In: *SciPost Phys.* 14 (2023), p. 140.

[115] P. Sala et al. “Dynamics in Systems with Modulated Symmetries”. In: *Phys. Rev. Lett.* 129 (Oct. 2022), p. 170601.

[116] Jason Iaconis, Andrew Lucas, and Rahul Nandkishore. “Multipole conservation laws and subdiffusion in any dimension”. In: *Phys. Rev. E* 103 (Feb. 2021), p. 022142.

[117] Abhishodh Prakash, Alain Goriely, and S. L. Sondhi. “Classical nonrelativistic fractons”. In: *Phys. Rev. B* 109 (Feb. 2024), p. 054313.

[118] Abhishodh Prakash, Ylias Sadki, and S. L. Sondhi. “Machian fractons, Hamiltonian attractors, and nonequilibrium steady states”. In: *Phys. Rev. B* 110 (July 2024), p. 024305.

[119] Abhishodh Prakash et al. “Eigenstate phases with finite on-site non-Abelian symmetry”. In: *Phys. Rev. B* 96 (16 Oct. 2017), p. 165136.

[120] Wei-Han Li, Xiaolong Deng, and Luis Santos. “Hilbert Space Shattering and Disorder-Free Localization in Polar Lattice Gases”. In: *Phys. Rev. Lett.* 127 (26 Dec. 2021), p. 260601.

[121] Alvise Bastianello, Umberto Borla, and Sergej Moroz. “Fragmentation and Emergent Integrable Transport in the Weakly Tilted Ising Chain”. In: *Phys. Rev. Lett.* 128 (19 May 2022), p. 196601.

[122] I-Chi Chen and Thomas Iadecola. “Emergent symmetries and slow quantum dynamics in a Rydberg-atom chain with confinement”. In: *Phys. Rev. B* 103 (21 June 2021), p. 214304.

[123] Philipp Frey et al. “Probing Hilbert space fragmentation and the block inverse participation ratio”. In: *Phys. Rev. B* 109 (6 Feb. 2024), p. 064302.

[124] E. V. H. Doggen, I. V. Gornyi, and D. G. Polyakov. “Stark many-body localization: Evidence for Hilbert-space shattering”. In: *Phys. Rev. B* 103 (10 Mar. 2021), p. L100202.

[125] Jordan S. Cotler et al. “Black holes and random matrices”. In: *Journal of High Energy Physics* 2017.5 (May 2017), p. 118.